# Methodologies for the Mechanistic Study of Compartment-Specific Hydrogen Peroxide Perturbations

by

Kassi Taylor Stein

M.S., Massachusetts Institute of Technology (2016)
B.S., Northeastern University (2014)

Submitted to the Department of Chemical Engineering
in Partial Fulfillment of the Requirements for the Degree of

Doctor of Philosophy

at the

Massachusetts Institute of Technology

June 2019



Signature of author.....
Department of Chemical Engineering
May 10, 2019

Certified by .....
Hadley D. Sikes
Associate Professor of Chemical Engineering
Thesis Supervisor

Accepted by .....
Patrick Doyle
Professor of Chemical Engineering
Chairman, Committee for Graduate Students

This thesis has been examined by:

**Professor Hadley D. Sikes**
Thesis Supervisor
Associate Professor of Chemical Engineering
Esther and Harold E. Edgerton Career Development Professor
Massachusetts Institute of Technology

**Professor Douglass Lauffenburger**
Committee Chair
Ford Professor of Biological Engineering, Chemical Engineering, and Biology
Head, Department of Biological Engineering
Massachusetts Institute of Technology

**Professor Kwanghun Chung**
Committee Member
Assistant Professor of Chemical Engineering
Massachusetts Institute of Technology

Methodologies for the Mechanistic Study of Compartment-Specific Hydrogen Peroxide Perturbations

by
Kassi Taylor Stein

Submitted to the Department of Chemical Engineering
on May 10, 2019 in Partial Fulfillment of the Requirements for the
Degree of Doctor of Philosophy in Chemical Engineering

# Abstract

Reactive oxygen species (ROS) are an interesting class of molecules because of their ability to promote contradictory phenotypes depending on their intracellular concentration. Most significantly, their elevation has been linked with several pathologies, including cancer. The selective cancer killing hypothesis hinges on the idea that certain cancers will be more susceptible to toxicity via a redox-based mechanism than their surrounding healthy counterparts, and provides an attractive target for those studying redox biology. In order to effectively leverage this strategy, quantitative knowledge of intracellular ROS, specifically hydrogen peroxide ($H_2O_2$) and its associated pathway proteins, is necessary.

This thesis developed tools and methodology for quantitative and mechanistic studies of $H_2O_2$ in the mitochondria. Both experimental and computational tools were developed and implemented to analyze mitochondrial $H_2O_2$, peroxiredoxin (Prx) proteins, and primary patient tumor cells. It was established that the toxicity of $H_2O_2$ perturbations localized to the mitochondrial matrix is dose- and time-dependent. A computational model of the mitochondrial $H_2O_2$ reaction network predicted that basal steady-state mitochondrial $H_2O_2$ concentrations are in the low nM range, and that Prx3 is responsible for $H_2O_2$ dynamics. Preliminary data in primary patient tumor cells of paraganglioma and related tumors with succinate dehydrogenase b (SDHB) mutations suggested these cancers are potentially sensitive to the investigational chemotherapeutic piperlongumine. And finally, analysis on the Prx family using statistical coupling analysis suggested evolutionarily conserved clusters of residues at the C-terminus of the Prx2 and Prx1 protein families that may point to a structure-function mechanism for their ability to complex with other proteins. All in all, these tools can be used in other cancer cell systems to better understand the quantitative $H_2O_2$ signaling mechanisms and possible chemotherapeutic targets within those pathways.

Thesis Supervisor: Hadley D. Sikes
Title: Associate Professor of Chemical Engineering

# Acknowledgements

This thesis would have never been possible without the unwavering support of my family. My entire educational path has been promoted, supported, uplifted, and cheered on by my mother, grandparents, aunts and uncles, and even (though perhaps with less vigor) my brothers. My mother, Maria Stein, in particular has been a role model, and provided everything I needed to be successful today, whether that was sound career advice, reassurance when I doubted myself, or even just an excuse to take a break and relax. This work is also dedicated to my niece and my godson, who each joined the world at various points in my graduate school career and have brought a lot of joy into my life.

I also owe tremendous gratitude to all my friends who encouraged me, supported me, and kept me sane throughout this whole experience. To Melanie, thank you for never letting me quit, no matter how many times I threatened it. To Katie, thank you for being both family and friend, and always knowing that good food fixes everything. To Emily, thank you for being my fiercest cheerleader and frankest advocate. To Emily Jo, thank you for always indulging my whimsical nature and always being the best friend anyone could ask for. To my friends in my cohort, I would have never survived first year without you (or second or third year). I am proud to know each of you and can't wait to see what you'll accomplish next. Finally, to my ONE TEAM from Practice School, somehow we managed not to kill each other, despite spending way too many hours together working on such tight deadlines. Thank you for all the adventures.

Thank you Dr. Hadley Sikes for being my adviser and mentor. These five years challenged me to synthesize concepts and techniques from a multitude of fields, go head-to-head with biologists and chemists, and find my voice out here in the "wild west". Thank you for resisting the status quo of academia in many ways, and for fighting for a more equitable future. I am grateful that there was always someone in my corner, regardless of the other ups and downs that transpired. Thank you also to all the members of the Sikes lab, past and present. Kara Huang, thank you for training me and passing the baton (and teaching me Western blotting over Skype). This thesis would not have happened without the ground work you laid down. Also thank you to Kaja Kaastrup as well as Kara for reaching out when I was at wit's end. Sometimes you need a little solidarity to make it through. Troy Langford was my only partner in redox biology for a while, so a huge thanks for taking care of my cells when I was out of town and for swapping tips and tricks when experiments failed. I am now passing the baton to Sun Jin Moon and Lynn Hao, who have many great ideas to take quantitative redox biology in new directions. Try not to let the Western blots get you down. I would be remiss if I didn't also thank Brooke Tam, who was my partner in being a pseudo-lab manager and just an overall great friend. Also, big thanks to my UROPs Natasha Stark, Katherine Hahn, and Athena Nguyen. Athena in particular contributed a lot of work to the third chapter of this thesis. I look forward to seeing what else you accomplish. Many thanks to Caroline Werlang for her help with SCA, which was originally a class project for 20.440 that snowballed. I have never felt such joy over a class assignment. Thank you to Dr. Doug Lauffenburger for all your guidance, helpful advice, and support during uncertain times. Additional thanks to all the members of the Lauffenburger lab that helped and supported me as I figured out systems biology and related topics. Thank you to Drs. Art Tischler and James Powers of Tufts Medical Center for collaborating with us on the rare endocrine tumor work. Thank you to Jaime Cheah and Christian Soule from the High-Throughput Screening core at the Koch Institute, who have helped me get beautiful data and have also given me great advice. Finally, thank you to the greater redox biology community,

whom I had the privilege to meet at the GRS and GRC this past summer. In particular, the other grad students and postdocs I met really inspired me at a time when my motivation was at an all-time low. I am grateful for all the friends I made at the Gordon Conference, and I hope our paths cross again.

Last but not least, thank you to my partner in every one of these ups and downs, Justin. The process of making it to the end of this thesis has certainly been tumultuous, and I appreciate all your support, encouragement, and offerings of mac and cheese. Your goofiness has uplifted me when I was ready to throw in the towel on numerous occasions. Thank you for being on this bizarre roller coaster with me. I can't wait for the next adventure.

# Table of Contents

## Table of Figures

# Table of Tables

# Chapter 1 : Introduction

Reactive oxygen species (ROS) are a class of molecules that arise as a result of the abundance of diatomic oxygen ($O_2$) in aerobic species. Redox biology spans all kingdoms of life, and many antioxidant defense proteins are highly evolutionarily conserved across species [1–3]. This chemical class is compelling for study because ROS can elicit diverse phenotypes depending on their intracellular concentration. At low concentrations, they promote homeostasis; as that intracellular concentration increases, we expect to observe pathogenesis, oncogene activation, and eventually toxicity and cell death [4,5]. This more nuanced understanding of ROS as more than simply deleterious agents is a relatively recent development [6]. While our qualitative understanding of the biological roles of ROS grows, still lacking is a specific, quantitative, and dynamic characterization of ROS species.

## 1.1 Hydrogen Peroxide

ROS can take several forms; common biologically relevant species comprise hydrogen peroxide ($H_2O_2$), superoxide ($O_2^{\cdot-}$), and hydroxyl radical ($HO^{\cdot}$) [7]. $H_2O_2$ alone among ROS is known to behave as a classical signaling molecule [5,8–10]. Unlike radical species, $H_2O_2$ is expected to be able to cross biological membranes and participate in specific chemical reactions inside the cell [8,11]. The primary intracellular target for $H_2O_2$ signaling is protein cysteine residues, as depicted in Figure 1.1 [8]. $H_2O_2$ reacts with thiol groups to form sulfenic acid, which is then free to form disulfides. The sulfenic acid can condense into an internal disulfide bond, or it can form intermolecular bonds. Alternatively, under high concentrations of $H_2O_2$, the sulfenic acid can react with additional molecules of $H_2O_2$ to form sulfinic or sulfonic acid [8,12].

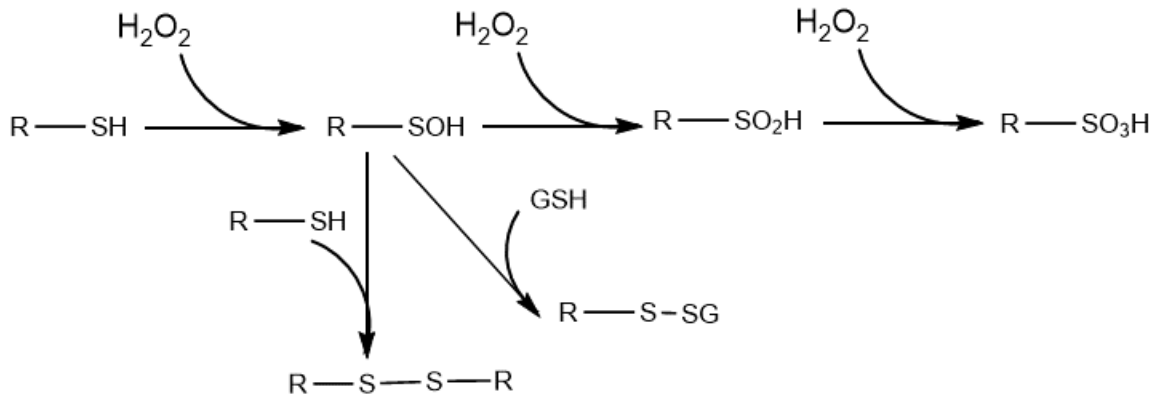


*Figure 1.1: $H_2O_2$ reactions with protein thiols.*

Thiol groups actually differ greatly in reactivity depending on the local protein structure [12,13]. General protein thiols have a reactivity on the order of 20 $s^{-1}M^{-1}$ while specialized antioxidants like the 2-Cys peroxiredoxins (Prx) react with $H_2O_2$ on the order of $1x10^8$ $s^{-1}M^{-1}$ [14–16]. The Prx group of antioxidants comprise the most abundant family of $H_2O_2$ scavenging proteins [17,18]. The 2-Cys Prxs dimerize in a head-to-tail fashion. The catalytic or peroxidatic cysteine ($C_P$) forms a disulfide bond with the resolving cysteine ($C_R$) upon oxidation that links the homodimer [13,19]. Figure 1.2 depicts schematically the way 2-Cys Prxs react with $H_2O_2$. It is currently unclear by what mechanism low-reactivity thiols become oxidized when this reaction is kinetically unfavorable. The chief hypothesis that has been proposed is the redox relay; $H_2O_2$ does not directly react with these thiols, but rather, reacts with Prx, and then that oxidized dimer reacts with the protein thiol and "transfers" its disulfide [20,21].

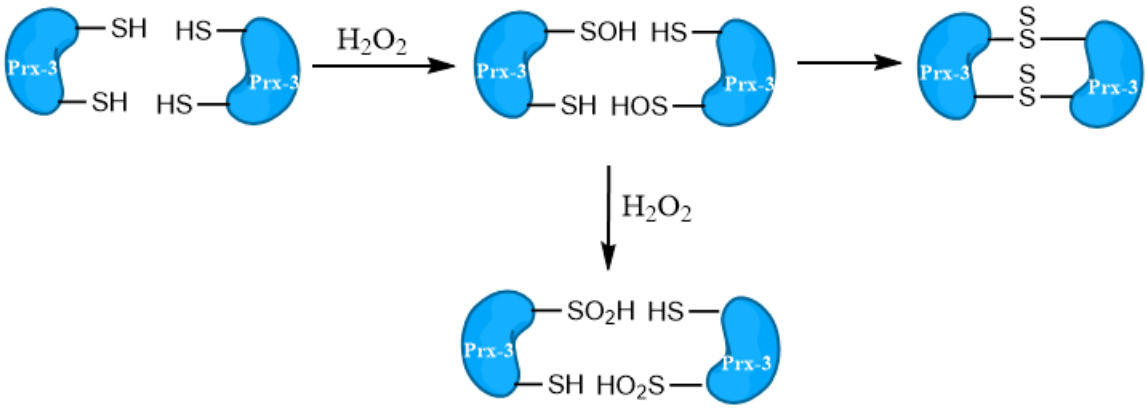


*Figure 1.2: General 2-Cys Prx reaction scheme, illustrated by the mitochondrion-specific Prx3. The catalytic cysteine of Prx becomes oxidized by $H_2O_2$ to form a sulfenic acid. This causes a local conformational change that allows the resolving cysteine to become accessible for disulfide formation with the catalytic cysteine on the opposite monomer, completing the formation of the dimer [10]. Alternatively, under high concentrations of $H_2O_2$, the sulfenic acid can be oxidized an additional time by $H_2O_2$ to a sulfinic acid, which is then unable to form dimers.*

The Prxs have six different mammalian isoforms, each one showing different compartment sequestration within the cell [3]. Among the typical 2-Cys Prxs, Prx1 and Prx2 are cytosolic, Prx3 is mitochondrial, and Prx4 is specific to the Endoplasmic Reticulum (ER) [22]. Prx5, an atypical 2-Cys Prx, is putatively more reactive to reactive nitrogen species (RNS) than $H_2O_2$ [23]. Prx6 is a 1-Cys Prx [3]. The oxidized dimer formed upon oxidation of the typical 2-Cys Prxs is reduced by the thioredoxin (Trx) system using electrons from NADPH [24–26]. The hyperoxidized sulfinic/sulfonic acid forms of Prx are reduced by sulfiredoxin (Srx) [27,28].

It has long been proposed that catalase and the glutathione peroxidases (Gpx) were the main enzymes responsible for detoxifying $H_2O_2$ due to their fast reactivities [29]. Indeed, catalase has been measured to react with $H_2O_2$ with a second-order rate constant of $2.4x10^7$ $M^{-1}s^{-1}$ and Gpx1 has a second-order rate constant in the same order of magnitude [30,31]. Combining these data with information about these enzymes' relative abundance and sub-cellular sequestration paints a different picture. We expect catalase to remain to typically remain sequestered in peroxisomes, and only sometimes be expressed in mitochondria in certain, specialized cell types [32–35]. Additionally, based on the detailed kinetic experiments of several groups, we now know that the

second-order rate constant for Prx2 is higher than that of the Gpx system, $1.6x10^8$ $M^{-1}s^{-1}$ [16,36]. Prxs are also more abundant than Gpxs by at least one order of magnitude, meaning the former will have a higher pseudo first-order reaction rate constant with $H_2O_2$ [14]. Thus, based on a kinetic analysis, we expect Prx to be an important reaction partner of $H_2O_2$ [37].

Glutathione (GSH) and the glutaredoxins (Grx) are another piece of the redox puzzle whose role has recently come into question. GSH is an extremely abundant non-enzymatic protein antioxidant, reaching concentrations sometimes in excess of 5 mM [33,38,39]. Its abundance has led many to conclude that is has a crucial role in maintaining redox homeostasis [39]. However, inhibition of GSH synthesis using buthionine sulfoximine (BSO) has produced mixed results, and even improved cells' ability to detoxify an intracellular $H_2O_2$ perturbation [40–42]. It has been proposed that GSH's primary intracellular role may not be related to redox homeostasis per se, and that additional quantitative data is necessary to elucidate more precisely what role GSH has in $H_2O_2$ signaling [38,43]. Grx is the enzyme responsible for reversing the protein S-glutathionylation reaction, a post-translation modification wherein a disulfide bond between a protein and GSH is formed that may have some protective or even regulatory function [44–46].

## 1.2 Mitochondria

Mitochondria are organelles of active interest in redox biology because they are a putative site of $H_2O_2$ generation through the electron transport chain (ETC) and oxidative phosphorylation (OxPhos) [48–50]. It is currently hypothesized that during OxPhos, some electron leak occurs, causing incompletely reduced oxygen to be evolved as superoxide [51]. This superoxide is quickly converted to $H_2O_2$ by manganese superoxide dismutase (MnSOD) in the mitochondrial matrix [50,52]. Complexes I, II, and III are thought to be the specific sites of ROS generation, as well as the tricarboxylic acid (TCA) cycle enzymes 2-oxoglutarate dehydrogenase (Odh) and pyruvate

dehydrogenase (Pdh) [44]. The rate of ROS evolution due to OxPhos is expected to be proportional to the rate of cellular respiration, and various ETC complex inhibitors can alter this rate [51].

In addition to generating $H_2O_2$, the mitochondria is hypothesized to be the site of much $H_2O_2$-mediated signaling [51,53,54]. There are many routes through which mitochondrial $H_2O_2$ can trigger a signaling cascade, which includes post-translational modifications on thiol groups and redox relays [51]. Mitochondrial $H_2O_2$ signaling is hypothesized to play a role in processes like the mitochondrial permeability transition (MPT) [44,55], uncoupling [56,57], phosphatidylinositol 3 kinase (PI3K) signaling [58], and apoptosis [59]. One particular signaling cascade that has been implicated in cancer onset and progression is the Kelch-like ECH-associated protein 1 (Keap1)/ nuclear factor-like 2 (Nrf-2) pathway, depicted schematically in Figure 1.3 [60]. Under homeostatic conditions, Keap1 binds Nrf-2 and marks it for degradation, but if there is an increase in intracellular oxidants, Keap1 becomes oxidized, changing conformation and releasing Nrf-2 [61]. Nrf-2 is then free to translocate into the nucleus, where it acts as a transcriptional activator of the antioxidant responsive element (ARE) [62]. This regulatory element upregulates the transcription of many antioxidant proteins, including Gpx1 [63]. In certain cancers, Keap1 is mutated, causing a constitutive upregulation of the ARE, as Nrf-2 is always bound there [64]. This mutation has been implicated in drug resistance [65].

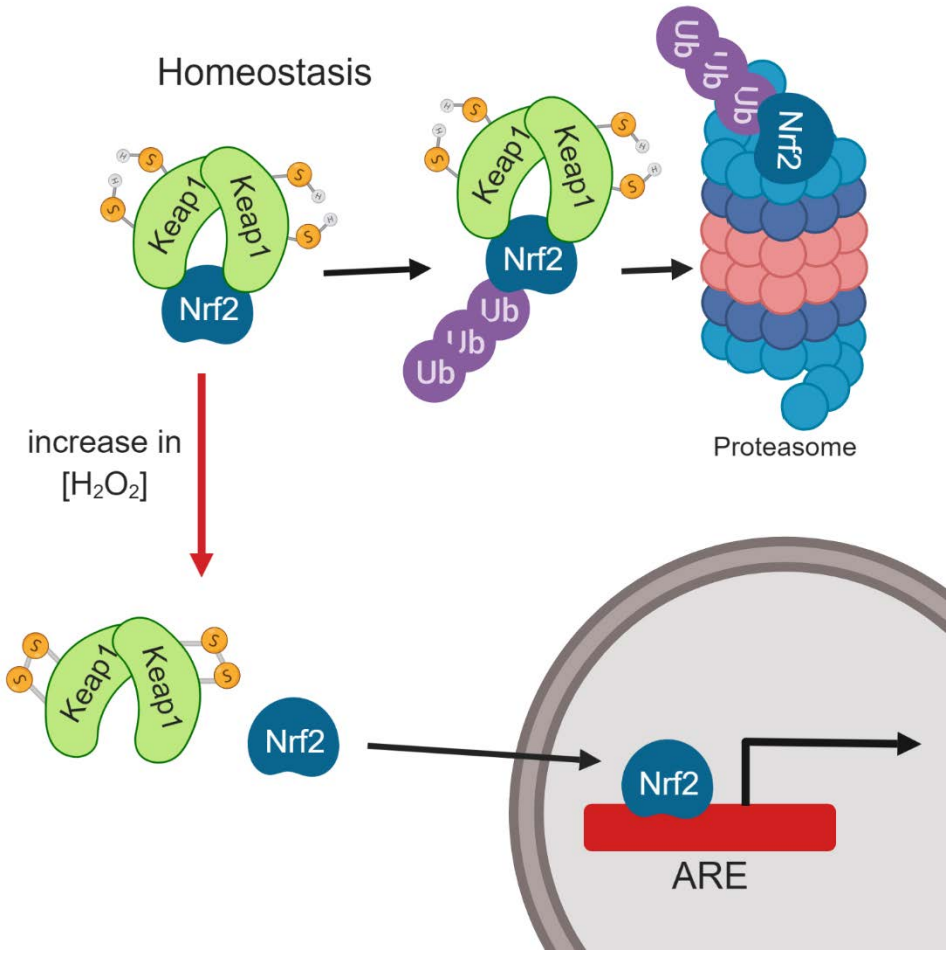


*Figure 1.3: The Keap1/Nrf-2 Pathway. A simplified schematic of the Keap1/Nrf-2 signaling pathway. Under homeostatic conditions, dimeric Keap1 binds Nrf-2 and marks it for degradation by the proteasome. If there is an increase in intracellular $H_2O_2$, then cysteine residues on Keap1 become oxidized, causing a conformational change that releases Nrf2. This allows Nrf2 to translocate into the nucleus and act as a transcription factor, binding the antioxidant responsive element (ARE) and upregulating the transcription of certain antioxidant and other stress response genes. Image created using BioRender.com.*

Another way the mitochondria is putatively involved in $H_2O_2$-mediated signaling is via the Bcl-2 family of proteins [66–68]. This protein family consists of pro- and anti-apoptotic proteins that normally allow the cell to regulate programmed cell death, though they sometimes become dysregulated in cancer [69,70]. Bcl-2 and related pro-survival proteins are associated with the mitochondrial outer membrane, whereas Bax and Bak, the pro-apoptotic proteins, translocate to the mitochondrial membrane upon receiving a cytotoxic signal [68,69,71]. Bax and Bak have been found to promote the mitochondrial outer membrane polarization (MOMP) whereas Bcl-2 has been found to suppress this; some linear combination between these competing signals will

ultimately determine cell fate [69,71]. Bcl-2 has already been identified as oncogenic, and efforts to target it have demonstrated that it is responsive to redox-mediated signaling, likely via post-translational modification [67,68,70,72,73].

The mitochondria has been found to maintain its own redox homeostasis separate from the cytosol and other organelles [74,75]. As previously mentioned, Prx3 is the Prx isoform native to this organelle. Prx5 is also present, as well as two Gpx isoforms, 1 and 4. Trx2, a distinct isoform from the cytosolic Trx1, is responsible for reducing the mitochondrial Prxs [26]. Quantitative efforts to characterize this interesting organelle have largely focused on the ETC [76]. Some groups have explicitly modeled the rate of generation of $H_2O_2$ as a function of cellular respiration and mitochondrial membrane polarization; these models are quite detailed, and focus on fast-respiring cell types (e.g. cardiac cells) [52,77,78]. Some other models have sought to integrate mitochondrial and cytosolic ROS [79,80]. As our quantitative understanding continues to grow, computational models of the mitochondria will be able to answer a more diverse array of questions.

## 1.3 Tools and Methodology

Most of the tools that have existed in the field until very recently were quite effective at qualitative characterizations [81,82]. This allowed for a broad understanding of many cellular redox processes and the discovery of antioxidant pathways. As we look towards developing a clear mechanistic understanding of $H_2O_2$ signaling, tools would ideally have spatiotemporal resolution, be quantitative rather than qualitative, and be specific for $H_2O_2$ only. The advent of genetically encoded probes and synthetic biology tools has greatly improved our ability to make quantitative measurements of cellular systems [81]. Measurement tools and tools for creating perturbations have improved over time, but still face limitations.

Dyes have traditionally been used as sensors of ROS changes. Though vendor websites often claim specificity, it is unclear how specific these dyes actually are in their chemistry. The

dyes MitoSOX and dihydroethidium are marketed as $O_2^{\cdot-}$ sensors. The dye 2',7'-dichlorodihydrofluorescein diacetate (H2DCFDA), converted to the fluorescent 2',7'-dichlorofluorescein (DCF) intracellularly, is commonly used to detect changes in ROS levels. Experiments using this latter compound are fraught with artifacts, as DCF itself can act as a photosensitizer of H2DCFDA and can also generate radicals itself [81–83]. Newer dyes have recently been developed with some of the drawbacks of older methods in mind; mitochondrially targeted ROS dyes with reversible fluorescence were developed as sensors of the state of all the redox couples in the mitochondria [84].

In order to overcome some of the limitations presented by fluorescent dyes, protein-based sensors have been developed. These offer the advantages of being specific and reversible, allowing measurement of how a signal is changing over time [14,85]. Because they are genetically encoded, they can be stably expressed in a cell line, and the gene can also be modified for localization to a specific organelle. Several sensors specific to $H_2O_2$ have been developed. HyPer, based on the OxyR transcription factor derived from microbes, consists of a circular-permuted yellow fluorescent protein (cpYFP) inserted into the $H_2O_2$-sensititve domain of OxyR. Upon oxidation by $H_2O_2$, HyPer's cpYFP changes conformation, causing a change in the ratio of the sensor's two characteristic fluorescent peaks [86]. Another probe, roGFP-Orp1, is based on a similar concept, but uses a redox-sensitive green fluorescent protein (roGFP) [82]. Both of these probes have been directed to other organelles, like the mitochondria, to track specific sub-cellular changes in $H_2O_2$ [87,88]. Both HyPer and roGFP-Orp1 are relatively insensitive to low-level $H_2O_2$ perturbations. Recently, a more sensitive probe based on engineered Prx2 was developed. This probe uses the principles of Förster resonance energy transfer (FRET) to elicit a change in fluorescence upon formation of the oxidized dimer of Prx2 [89]. The dynamic range of the FRET probe was sufficient

to cover low-level perturbations that were below the limit of detection of HyPer and roGFP-Orp1, and when this probe saturated, the other probes were able to sense $H_2O_2$ changes [85,89]. A more sensitive $H_2O_2$ sensor specific for the mitochondria was also recently developed based on the yeast analog of Prx, Tsa2, and roGFP [90]. This probe was well-validated in a yeast model system but does not translate to mammalian systems.

Specific generators of $H_2O_2$ are tools that have also been leveraged by the field to deliver a tunable perturbation. Glucose oxidase (Gox) has been used to generate $H_2O_2$ extracellularly, as it can consume glucose present in cell culture media and produce a steady output of $H_2O_2$ [91]. This is a useful tool for modeling an exogenous signal, like from inflammation. An enzyme derived from yeast, D-amino acid oxidase (DAAO), has been leveraged for its ability to convert D-amino acids into $H_2O_2$ in a tunable fashion [92]. This enzyme is genetically encoded rather than added extracellularly, creating an intracellular perturbation that can be further targeted to specific organelles [93]. This tool is useful for modeling an endogenous signal, like one that would be introduced by a redox-based chemotherapeutic.

Some groups have made significant strides in understanding and targeting small molecule tools to the mitochondria. This can generally be achieved by attaching a lipophilic triphenylphosphonium cation ($TPP^+$) to a molecule [66,94–96]. The use of an alkyl linker has been successfully used to attach $TPP^+$ to antioxidants like ubiquinone and α-tocopherol (vitamin E) in order to dose the mitochondria with them [97,98]. $TPP^+$ has also been linked to thiol reagents like 4-iodobutyl and 4-thiobutyl to identify reactive thiols in the mitochondria specifically [99] and to a Trx reductase (TrxR) inhibitor to block only mitochondrial TrxR activity [75]. Finally, the Murphy group in particular has used small molecules to perturb the mitochondria. For example, using paraquat,

which interacts with complex I, they have altered superoxide production [100]. These targeted tools are useful in the quest for building a spatially-resolved understanding of $H_2O_2$ signaling.

## 1.4 Redox-based Chemotherapeutics

Redox-based chemotherapeutics have become an attractive target because of the selective cancer killing hypothesis. This is the hypothesis that certain cancers, due to their aberrant metabolism and subsequent adaptations, have higher endogenous concentrations of ROS than the healthy cells around them, so if a patient were given a therapeutic systemically that raised the ROS levels in all cells, only the cancer cells would be raised above some toxic threshold [70]. Several drugs, both currently in use and under investigation, work by perturbing intracellular redox pathways in some way.

Many interesting compounds currently on the market for cancer treatment have been found to involve a mitochondrial redox-mediated mechanism. These include cisplatin [101,102], arsenic trioxide [103,104], and tamoxifen [105,106]. Tamoxifen was found to interfere with mitochondrial complex I, and a horseradish peroxidase (HRP) assay demonstrated increased $H_2O_2$ with tamoxifen treatment in isolated liver mitochondria [106]. Arsenic trioxide is an uncoupler of OxPhos and has also been found to bind thiol residues [104]. Cisplatin binds purines, interfering with DNA synthesis, but has also been demonstrated to alter GSH and Gpx concentrations [101,102,107]. This compound has been targeted to the mitochondria using $TPP^+$ to enhance its chemotherapeutic effects [99].

There has also been a marked interest in evaluating natural products and other small molecules for potential therapeutic effect. Many small molecules currently in use as supplements are under investigation for potential redox-based anti-cancer activity. These include α-tocopherol succinate (a vitamin E analog) [108–110], curcumin [111,112], imexon [113–115], and lonidamine [66,73]. Piperlongumine is a small molecule investigational therapeutic that has been demonstrated to act via a $H_2O_2$-dependent mechanism in the cytoplasm by using mechanistic synthetic biology tools

[40]. This type of methodology will be useful in further understanding the mechanisms of all the compounds listed here, as well as ones yet to be investigated.

## 1.5 Purpose of Thesis Work

In this work, tools and methodology for developing a quantitative understanding of mitochondrial $H_2O_2$ are presented. This is achieved experimentally by using synthetic biology tools and redox Western blots alongside more traditional assay like immunofluorescence. A computational modeling framework is presented to contextualize the experimental results in the appropriate concentration range and build a mechanistic understanding of the mitochondrial $H_2O_2$ reaction network. Two exploratory pieces are also presented. First, a methodology for analyzing primary patient tumors for sensitivity to an investigational chemotherapeutic while maintaining statistical power was developed. Second, an analysis on the Prx proteins using statistical coupling analysis (SCA) to look for evolutionarily conserved clusters of residues and what they might mean about the proteins' structure and function was performed. These thesis results provide an overall proof-of-concept system for making and measuring $H_2O_2$ perturbations and the related Prx proteins, which can be applied in clinically relevant cancer systems.

## 1.6 References


(1) Kemp, M.; Go, Y.-M.; Jones, D. P. Nonequilibrium Thermodynamics of Thiol/Disulfide Redox Systems: A Perspective on Redox Systems Biology. *Free Radic. Biol. Med.* **2008**, *44* (6), 921–937.

(2) Holmgren, A.; Lu, J. Thioredoxin and Thioredoxin Reductase: Current Research with Special Reference to Human Disease. *Biochem. Biophys. Res. Commun.* **2010**, *396* (1), 120–124.

(3) Wood, Z. a; Schröder, E.; Robin Harris, J.; Poole, L. B. Structure, Mechanism and Regulation of Peroxiredoxins. *Trends Biochem. Sci.* **2003**, *28* (1), 32–40.

(4) Sies, H. Oxidative Stress: A Concept in Redox Biology and Medicine. *Redox Biol.* **2015**, *4*, 180–183.

(5) Gough, D. R.; Cotter, T. G. Hydrogen Peroxide: A Jekyll and Hyde Signalling Molecule. *Cell Death Dis.* **2011**, *2* (10), e213.

(6) Murphy, M. P.; Holmgren, A.; Larsson, N.-G.; Halliwell, B.; Chang, C. J.; Kalyanaraman, B.; Rhee, S. G.; Thornalley, P. J.; Partridge, L.; Gems, D.; et al. Unraveling the Biological Roles of Reactive Oxygen Species. *Cell Metab.* **2011**, *13* (4), 361–366.

(7) Kehrer, J. P.; Robertson, J. D.; Smith, C. V. Free Radicals and Reactive Oxygen Species. *Compr. Toxicol.* **2010**, No. August 2014, 277–307.
(8) Lennicke, C.; Rahn, J.; Lichtenfels, R.; Wessjohann, L. A.; Seliger, B. Hydrogen Peroxide – Production, Fate and Role in Redox Signaling of Tumor Cells. *Cell Commun. Signal.* **2015**, *13* (1), 39.
(9) Sies, H. Hydrogen Peroxide as a Central Redox Signaling Molecule in Physiological Oxidative Stress: Oxidative Eustress. *Redox Biol.* **2017**, *11*, 613–619.
(10) Young, D.; Pedre, B.; Ezeriņa, D.; De Smet, B.; Lewandowska, A.; Tossounian, M.-A.; Bodra, N.; Huang, J.; Astolfi Rosado, L.; Van Breusegem, F.; et al. Protein Promiscuity in H 2 O 2 Signaling. *Antioxid. Redox Signal.* **2019**, *30* (10), 1285–1324.
(11) Winterbourn, C. C. Are Free Radicals Involved in Thiol-Based Redox Signaling? *Free Radic. Biol. Med.* **2015**, *80*, 164–170.
(12) Paulsen, C. E.; Carroll, K. S. Cysteine-Mediated Redox Signaling: Chemistry, Biology, and Tools for Discovery. *Chem. Rev.* **2013**, *113* (7), 4633–4679.
(13) Winterbourn, C. C.; Peskin, A. V. Kinetic Approaches to Measuring Peroxiredoxin Reactivity. *Mol. Cells* **2016**, *39* (1), 26–30.
(14) Huang, B. K.; Sikes, H. D. Quantifying Intracellular Hydrogen Peroxide Perturbations in Terms of Concentration. *Redox Biol.* **2014**, *2*, 955–962.
(15) Lim, J. B.; Huang, B. K.; Deen, W. M.; Sikes, H. D. Analysis of the Lifetime and Spatial Localization of Hydrogen Peroxide Generated in the Cytosol Using a Reduced Kinetic Model. *Free Radic. Biol. Med.* **2015**, *89*, 47–53.
(16) Portillo-Ledesma, S.; Randall, L. M.; Parsonage, D.; Dalla Rizza, J.; Karplus, P. A.; Poole, L. B.; Denicola, A.; Ferrer-Sueta, G. Differential Kinetics of Two-Cysteine Peroxiredoxin Disulfide Formation Reveal a Novel Model for Peroxide Sensing. *Biochemistry* **2018**, acs.biochem.8b00188.
(17) Netto, L. E. S.; Antunes, F. The Roles of Peroxiredoxin and Thioredoxin in Hydrogen Peroxide Sensing and in Signal Transduction. *Mol. Cells* **2016**, *39* (1), 65–71.
(18) Lim, J. B.; Langford, T. F.; Huang, B. K.; Deen, W. M.; Sikes, H. D. A Reaction-Diffusion Model of Cytosolic Hydrogen Peroxide. *Free Radic. Biol. Med.* **2016**, *90*, 85–90.
(19) Zeida, A.; Reyes, A. M.; Lebrero, M. C. G.; Radi, R.; Trujillo, M.; Estrin, D. A. The Extraordinary Catalytic Ability of Peroxiredoxins: A Combined Experimental and QM/MM Study on the Fast Thiol Oxidation Step. *Chem. Commun.* **2014**, *50* (70), 10070.
(20) Sobotta, M. C.; Liou, W.; Stöcker, S.; Talwar, D.; Oehler, M.; Ruppert, T.; Scharf, A. N. D.; Dick, T. P. Peroxiredoxin-2 and STAT3 Form a Redox Relay for H2O2 Signaling. *Nat. Chem. Biol.* **2014**, *11* (1), 64–70.
(21) Travasso, R. D. M.; Sampaio dos Aidos, F.; Bayani, A.; Abranches, P.; Salvador, A. Localized Redox Relays as a Privileged Mode of Cytoplasmic Hydrogen Peroxide Signaling. *Redox Biol.* **2017**, *12* (November 2016), 233–245.
(22) Poynton, R. A.; Peskin, A. V; Haynes, A. C.; Lowther, W. T.; Hampton, M. B.; Winterbourn, C. C. Kinetic Analysis of Structural Influences on the Susceptibility of Peroxiredoxins 2 and 3 to Hyperoxidation. *Biochem. J.* **2016**, *473* (4), 411–421.
(23) Trujillo, M.; Carballal, S.; Zeida, A.; Radi, R. Comparative Analysis of Hydrogen Peroxide and Peroxynitrite Reactivity with Thiols. In *Hydrogen Peroxide Metabolism in Health and Disease*; Vissers, M. C. M., Hampton, M. B., Kettle, A. J., Eds.; CRC Press: Boca Raton, FL, 2018; pp 49–79.

(24) Matsuzawa, A. Thioredoxin and Redox Signaling: Roles of the Thioredoxin System in Control of Cell Fate. *Arch. Biochem. Biophys.* **2016**, *617*, 101–105.
(25) Holmgren, A. Thioredoxin Structure and Mechanism: Conformational Changes on Oxidation of the Active-Site Sulfhydryls to a Disulfide. *Structure* **1995**, *3* (3), 239–243.
(26) Hanschmann, E. M.; Lönn, M. E.; Schütte, L. D.; Funke, M.; Godoy, J. R.; Eitner, S.; Hudemann, C.; Lillig, C. H. Both Thioredoxin 2 and Glutaredoxin 2 Contribute to the Reduction of the Mitochondrial 2-Cys Peroxiredoxin Prx3. *J. Biol. Chem.* **2010**, *285* (52), 40699–40705.
(27) Chang, T.-S.; Woo, H. A.; Park, K. J.; Rhee, S. G.; Yang, J. S.; Jeong, W.; Park, S. J. Reduction of Cysteine Sulfinic Acid by Sulfiredoxin Is Specific to 2-Cys Peroxiredoxins. *J. Biol. Chem.* **2004**, *280* (5), 3125–3128.
(28) Chang, T.-S.; Jeong, W.; Woo, H. A.; Lee, S. M.; Park, S.; Rhee, S. G. Characterization of Mammalian Sulfiredoxin and Its Reactivation of Hyperoxidized Peroxiredoxin through Reduction of Cysteine Sulfinic Acid in the Active Site to Cysteine. *J. Biol. Chem.* **2004**, *279* (49), 50994–51001.
(29) Jones, D. P.; Eklöw, L.; Thor, H.; Orrenius, S. Metabolism of Hydrogen Peroxide in Isolated Hepatocytes: Relative Contributions of Catalase and Glutathione Peroxidase in Decomposition of Endogenously Generated H2O2. *Arch. Biochem. Biophys.* **1981**, *210* (2), 505–516.
(30) Greenfield, R. E.; Price, V. E. Liver Catalase: I. A Manometric Determination of Catalase Activity. *J. Biol. Chem.* **1954**, No. 209, 355–361.
(31) Ng, C. F.; Schafer, F. Q.; Buettner, G. R.; Rodgers, V. G. J. The Rate of Cellular Hydrogen Peroxide Removal Shows Dependency on GSH: Mathematical Insight into in Vivo H2O2 and GPx Concentrations. *Free Radic. Res.* **2007**, *41* (11), 1201–1211.
(32) Rindler, P. M.; Cacciola, A.; Kinter, M.; Szweda, L. I. Catalase-Dependent H 2 O 2 Consumption by Cardiac Mitochondria and Redox-Mediated Loss in Insulin Signaling. *Am. J. Physiol. Circ. Physiol.* **2016**, *311* (5), H1091–H1096.
(33) Dey, S.; Sidor, A.; O'Rourke, B. Compartment-Specific Control of Reactive Oxygen Species Scavenging by Antioxidant Pathway Enzymes. *J. Biol. Chem.* **2016**, *291* (21), 11185–11197.
(34) Buettner, G. R.; Wagner, B. a.; Rodgers, V. G. J. Quantitative Redox Biology: An Approach to Understand the Role of Reactive Species in Defining the Cellular Redox Environment. *Cell Biochem. Biophys.* **2013**, *67* (2), 477–483.
(35) Cox, A. G.; Winterbourn, C. C.; Hampton, M. B. Mitochondrial Peroxiredoxin Involvement in Antioxidant Defence and Redox Signalling. *Biochem. J.* **2010**, *425* (2), 313–325.
(36) Dalla Rizza, J.; Randall, L. M.; Santos, J.; Ferrer-Sueta, G.; Denicola, A. Differential Parameters between Cytosolic 2-Cys Peroxiredoxins, PRDX1 and PRDX2. *Protein Sci.* **2019**, *28* (1), 191–201.
(37) Winterbourn, C. C. Reconciling the Chemistry and Biology of Reactive Oxygen Species. *Nat. Chem. Biol.* **2008**, *4* (5), 278–286.
(38) Deponte, M. Glutathione Catalysis and the Reaction Mechanisms of Glutathione-Dependent Enzymes. *Biochim. Biophys. Acta - Gen. Subj.* **2013**, *1830* (5), 3217–3266.
(39) Ribas, V.; García-Ruiz, C.; Fernández-Checa, J. C. Glutathione and Mitochondria. *Front. Pharmacol.* **2014**, *5 JUL* (July), 1–19.
(40) Huang, B. K.; Langford, T. F.; Sikes, H. D. Using Sensors and Generators of H2O2 to

Elucidate the Toxicity Mechanism of Piperlongumine and Phenethyl Isothiocyanate. *Antioxid. Redox Signal.* **2016**, *24* (16), 924–938.
(41) Mishina, N. M.; Bogdanova, Y. A.; Ermakova, Y. G.; Panova, A. S.; Kotova, D. A.; Bilan, D.; Steinhorn, B.; Arnér, E. S. J.; Michel, T.; Belousov, V. Which Antioxidant System Shapes Intracellular H2O2 Gradients? *Antioxid. Redox Signal.* **2019**, *0* (ja), null.
(42) Brozovic, A.; Ambriović-Ristov, A.; Osmak, M. The Relationship between Cisplatin-Induced Reactive Oxygen Species, Glutathione, and BCL-2 and Resistance to Cisplatin. *Crit. Rev. Toxicol.* **2010**, *40* (4), 347–359.
(43) Deponte, M. The Incomplete Glutathione Puzzle: Just Guessing at Numbers and Figures? *Antioxid. Redox Signal.* **2017**, *27* (15), 1130–1161.
(44) Mailloux, R. J.; Jin, X.; Willmore, W. G. Redox Regulation of Mitochondrial Function with Emphasis on Cysteine Oxidation Reactions. *Redox Biology*. 2014, pp 123–139.
(45) Gould, N. S.; Evans, P.; Martínez-Acedo, P.; Marino, S. M.; Gladyshev, V. N.; Carroll, K. S.; Ischiropoulos, H. Site-Specific Proteomic Mapping Identifies Selectively Modified Regulatory Cysteine Residues in Functionally Distinct Protein Networks. *Chem. Biol.* **2015**, *22* (7), 965–975.
(46) Grek, C. L.; Zhang, J.; Manevich, Y.; Townsend, D. M.; Tew, K. D. Causes and Consequences of Cysteine S -Glutathionylation. *J. Biol. Chem.* **2013**, *288* (37), 26497–26504.
(47) Flohé, L. The Fairytale of the GSSG/GSH Redox Potential. *Biochim. Biophys. Acta - Gen. Subj.* **2013**, *1830* (5), 3139–3142.
(48) Mailloux, R. J. Teaching the Fundamentals of Electron Transfer Reactions in Mitochondria and the Production and Detection of Reactive Oxygen Species. *Redox Biol.* **2015**, *4*, 381–398.
(49) Mailloux, R. J.; Treberg, J. R. Protein S-Glutathionlyation Links Energy Metabolism to Redox Signaling in Mitochondria. *Redox Biol.* **2016**, *8*, 110–118.
(50) Collins, Y.; Chouchani, E. T.; James, A. M.; Menger, K. E.; Cocheme, H. M.; Murphy, M. P. Mitochondrial Redox Signalling at a Glance. *J. Cell Sci.* **2012**, *125* (7), 1837–1837.
(51) Shadel, G. S.; Horvath, T. L. Mitochondrial ROS Signaling in Organismal Homeostasis. *Cell* **2015**, *163* (3), 560–569.
(52) Kembro, J. M.; Aon, M. A.; Winslow, R. L.; O'Rourke, B.; Cortassa, S. Integrating Mitochondrial Energetics, Redox and ROS Metabolic Networks: A Two-Compartment Model. *Biophys. J.* **2013**, *104* (2), 332–343.
(53) Diebold, L.; Chandel, N. S. Mitochondrial ROS Regulation of Proliferating Cells. *Free Radic. Biol. Med.* **2016**, *100*, 86–93.
(54) Murphy, M. P. Mitochondrial Thiols in Antioxidant Protection and Redox Signaling: Distinct Roles for Glutathionylation and Other Thiol Modifications. *Antioxid. Redox Signal.* **2012**, *16* (6), 476–495.
(55) Cao, X.; Zhao, S.; Liu, D.; Wang, Z.; Niu, L.; Hou, L.; Wang, C. ROS-Ca2+ Is Associated with Mitochondria Permeability Transition Pore Involved in Surfactin-Induced MCF-7 Cells Apoptosis. *Chem. Biol. Interact.* **2011**, *190* (1), 16–27.
(56) Chouchani, E. T.; Kazak, L.; Jedrychowski, M. P.; Lu, G. Z.; Erickson, B. K.; Szpyt, J.; Pierce, K. A.; Laznik-Bogoslavski, D.; Vetrivelan, R.; Clish, C. B.; et al. Mitochondrial ROS Regulate Thermogenic Energy Expenditure and Sulfenylation of UCP1. *Nature* **2016**, *532* (7597), 112–116.
(57) Mailloux, R. J.; Xuan, J. Y.; Beauchamp, B.; Jui, L.; Lou, M.; Harper, M.-E.

Glutaredoxin-2 Is Required to Control Proton Leak through Uncoupling Protein-3. *J. Biol. Chem.* **2013**, *288* (12), 8365–8379.
(58) Kim, J.-H.; Choi, T. G.; Park, S.; Yun, H. R.; Nguyen, N. N. Y.; Jo, Y. H.; Jang, M.; Kim, J.; Kim, J.; Kang, I.; et al. Mitochondrial ROS-Derived PTEN Oxidation Activates PI3K Pathway for MTOR-Induced Myogenic Autophagy. *Cell Death Differ.* **2018**, *25* (11), 1921–1937.
(59) Chang, T.-S.; Cho, C.-S.; Park, S.; Yu, S.; Kang, S. W.; Rhee, S. G. Peroxiredoxin III, a Mitochondrion-Specific Peroxidase, Regulates Apoptotic Signaling by Mitochondria. *J. Biol. Chem.* **2004**, *279* (40), 41975–41984.
(60) Sullivan, L. B.; Chandel, N. S. Mitochondrial Reactive Oxygen Species and Cancer. *Cancer Metab.* **2014**, *2* (1), 17.
(61) Kang, J.; Pervaiz, S. Mitochondria: Redox Metabolism and Dysfunction. *Biochem. Res. Int.* **2012**, *2012*, 1–14.
(62) Bellezza, I.; Giambanco, I.; Minelli, A.; Donato, R. Nrf2-Keap1 Signaling in Oxidative and Reductive Stress. *Biochim. Biophys. Acta - Mol. Cell Res.* **2018**, *1865* (5), 721–733.
(63) Holmström, K. M.; Kostov, R. V.; Dinkova-Kostova, A. T. The Multifaceted Role of Nrf2 in Mitochondrial Function. *Curr. Opin. Toxicol.* **2017**, *2*, 80–91.
(64) Vyas, S.; Zaganjor, E.; Haigis, M. C. Mitochondria and Cancer. *Cell* **2016**, *166* (3), 555–566.
(65) Hong, Y. Bin; Kang, H. J.; Kwon, S. Y.; Kim, H. J.; Kwon, K. Y.; Cho, C. H.; Lee, J.-M.; Kallakury, B. V. S.; Bae, I. Nuclear Factor (Erythroid-Derived 2)-Like 2 Regulates Drug Resistance in Pancreatic Cancer Cells. *Pancreas* **2010**, *39* (4), 463–472.
(66) Milane, L.; Trivedi, M.; Singh, A.; Talekar, M.; Amiji, M. Mitochondrial Biology, Targets, and Drug Delivery. *J. Control. Release* **2015**, *207*, 40–58.
(67) Pohl, S. Ö.-G.; Agostino, M.; Dharmarajan, A.; Pervaiz, S. Cross Talk Between Cellular Redox State and the Antiapoptotic Protein Bcl-2. *Antioxid. Redox Signal.* **2018**, *00* (00), ars.2017.7414.
(68) Gross, A.; McDonnell, J. M.; Korsmeyer, S. J. BCL-2 Family Members and the Mitochondria in Apoptosis. *Genes Dev.* **1999**, *13* (15), 1899–1911.
(69) Cory, S.; Adams, J. M. The Bcl2 Family: Regulators of the Cellular Life-or-Death Switch. *Nat. Rev. Cancer* **2002**, *2* (9), 647–656.
(70) Trachootham, D.; Alexandre, J.; Huang, P. Targeting Cancer Cells by ROS-Mediated Mechanisms: A Radical Therapeutic Approach? *Nat. Rev. Drug Discov.* **2009**, *8* (7), 579–591.
(71) Czabotar, P. E.; Lessene, G.; Strasser, A.; Adams, J. M. Control of Apoptosis by the BCL-2 Protein Family: Implications for Physiology and Therapy. *Nat. Rev. Mol. Cell Biol.* **2014**, *15* (1), 49–63.
(72) Dunnill, C. J.; Ibraheem, K.; Mohamed, A.; Southgate, J.; Georgopoulos, N. T. A Redox State-Dictated Signalling Pathway Deciphers the Malignant Cell Specificity of CD40-Mediated Apoptosis. *Oncogene* **2017**, *36* (18), 2515–2528.
(73) Ravagnan, L.; Marzo, I.; Costantini, P.; Susin, S. a; Zamzami, N.; Petit, P. X.; Hirsch, F.; Goulbern, M.; Poupon, M. F.; Miccoli, L.; et al. Lonidamine Triggers Apoptosis via a Direct, Bcl-2-Inhibited Effect on the Mitochondrial Permeability Transition Pore. *Oncogene* **1999**, *18* (16), 2537–2546.
(74) Pastor-Flores, D.; Becker, K.; Dick, T. P. Monitoring Yeast Mitochondria with Peroxiredoxin-Based Redox Probes: The Influence of Oxygen and Glucose Availability.

*Interface Focus* **2017**, *7* (2), 20160143.
(75) Booty, L. M.; Gawel, J. M.; Cvetko, F.; Caldwell, S. T.; Hall, A. R.; Mulvey, J. F.; James, A. M.; Hinchy, E. C.; Prime, T. A.; Arndt, S.; et al. Selective Disruption of Mitochondrial Thiol Redox State in Cells and In Vivo. *Cell Chem. Biol.* **2019**, *26* (3), 449–461.e8.
(76) Pereira, E. J.; Smolko, C. M.; Janes, K. A. Computational Models of Reactive Oxygen Species as Metabolic Byproducts and Signal-Transduction Modulators. *Front. Pharmacol.* **2016**, *7* (November), 1–9.
(77) Gauthier, L. D.; Greenstein, J. L.; Cortassa, S.; O'Rourke, B.; Winslow, R. L. A Computational Model of Reactive Oxygen Species and Redox Balance in Cardiac Mitochondria. *Biophys. J.* **2013**, *105* (4), 1045–1056.
(78) Gauthier, L. D.; Greenstein, J. L.; O'Rourke, B.; Winslow, R. L. An Integrated Mitochondrial ROS Production and Scavenging Model: Implications for Heart Failure. *Biophys. J.* **2013**, *105* (12), 2832–2842.
(79) Pannala, V. R.; Dash, R. K. Mechanistic Characterization of the Thioredoxin System in the Removal of Hydrogen Peroxide. *Free Radic. Biol. Med.* **2015**, *78*, 42–55.
(80) Park, J.; Lee, J.; Choi, C. Mitochondrial Network Determines Intracellular ROS Dynamics and Sensitivity to Oxidative Stress through Switching Inter-Mitochondrial Messengers. *PLoS One* **2011**, *6* (8), e23211.
(81) Ezerina, D.; Morgan, B.; Dick, T. P. Imaging Dynamic Redox Processes with Genetically Encoded Probes. *J. Mol. Cell. Cardiol.* **2014**, *73* (09), 43–49.
(82) Meyer, A. J.; Dick, T. P. Fluorescent Protein-Based Redox Probes. *Antioxid. Redox Signal.* **2010**, *13* (5), 621–650.
(83) Schwarzländer, M.; Dick, T. P.; Meyer, A. J.; Morgan, B. Dissecting Redox Biology Using Fluorescent Protein Sensors. *Antioxid. Redox Signal.* **2016**, *24* (13), 680–712.
(84) Chong, K. L.; Chalmers, B. A.; Cullen, J. K.; Kaur, A.; Kolanowski, J. L.; Morrow, B. J.; Fairfull-Smith, K. E.; Lavin, M. J.; Barnett, N. L.; New, E. J.; et al. Pro-Fluorescent Mitochondria-Targeted Real-Time Responsive Redox Probes Synthesised from Carboxy Isoindoline Nitroxides: Sensitive Probes of Mitochondrial Redox Status in Cells. *Free Radic. Biol. Med.* **2018**, *128* (November 2017), 97–110.
(85) Huang, B. K.; Stein, K. T.; Sikes, H. D. Modulating and Measuring Intracellular H 2 O 2 Using Genetically Encoded Tools to Study Its Toxicity to Human Cells. *ACS Synth. Biol.* **2016**, *5* (12), 1389–1395.
(86) Belousov, V. V; Fradkov, A. F.; Lukyanov, K. A.; Staroverov, D. B.; Shakhbazov, K. S.; Terskikh, A. V; Lukyanov, S. Genetically Encoded Fluorescent Indicator for Intracellular Hydrogen Peroxide. *Nat. Methods* **2006**, *3* (4), 281–286.
(87) Malinouski, M.; Zhou, Y.; Belousov, V. V.; Hatfield, D. L.; Gladyshev, V. N. Hydrogen Peroxide Probes Directed to Different Cellular Compartments. *PLoS One* **2011**, *6* (1).
(88) Yang, K.; Kolanowski, J. L.; New, E. J. Mitochondrially Targeted Fluorescent Redox Sensors. *Interface Focus* **2017**, *7* (2), 20160105.
(89) Langford, T. F.; Huang, B. K.; Lim, J. B.; Moon, S. J.; Sikes, H. D. Monitoring the Action of Redox-Directed Cancer Therapeutics Using a Human Peroxiredoxin-2-Based Probe. *Nat. Commun.* **2018**, *9* (1), 3145.
(90) Morgan, B.; Van Laer, K.; Owusu, T. N. E.; Ezeriņa, D.; Pastor-Flores, D.; Amponsah, P. S.; Tursch, A.; Dick, T. P. Real-Time Monitoring of Basal H2O2 Levels with Peroxiredoxin-Based Probes. *Nat. Chem. Biol.* **2016**, No. April.
(91) Sobotta, M. C.; Barata, A. G.; Schmidt, U.; Mueller, S.; Millonig, G.; Dick, T. P.

Exposing Cells to H2O2: A Quantitative Comparison between Continuous Low-Dose and One-Time High-Dose Treatments. *Free Radic. Biol. Med.* **2013**, *60*, 325–335.
(92) Haskew-Layton, R. E.; Payappilly, J. B.; Smirnova, N. A.; Ma, T. C.; Chan, K. K.; Murphy, T. H.; Guo, H.; Langley, B.; Sultana, R.; Butterfield, D. A.; et al. Controlled Enzymatic Production of Astrocytic Hydrogen Peroxide Protects Neurons from Oxidative Stress via an Nrf2-Independent Pathway. *Proc. Natl. Acad. Sci.* **2010**, *107* (40), 17385–17390.
(93) Alim, I.; Haskew-Layton, R. E.; Aleyasin, H.; Guo, H.; Ratan, R. R. Spatial, Temporal, and Quantitative Manipulation of Intracellular Hydrogen Peroxide in Cultured Cells. *Methods Enzymol.* **2014**, *547* (1), 251–273.
(94) Smith, M. R.; Vayalil, P. K.; Zhou, F.; Benavides, G. A.; Beggs, R. R.; Golzarian, H.; Nijampatnam, B.; Oliver, P. G.; Smith, R. A. J.; Murphy, M. P.; et al. Mitochondrial Thiol Modification by a Targeted Electrophile Inhibits Metabolism in Breast Adenocarcinoma Cells by Inhibiting Enzyme Activity and Protein Levels. *Redox Biol.* **2016**, *8*, 136–148.
(95) Reily, C.; Mitchell, T.; Chacko, B. K.; Benavides, G. A.; Murphy, M. P.; Darley-Usmar, V. M. Mitochondrially Targeted Compounds and Their Impact on Cellular Bioenergetics. *Redox Biol.* **2013**, *1* (1), 86–93.
(96) Murphy, M. P.; Smith, R. A. J. Targeting Antioxidants to Mitochondria by Conjugation to Lipophilic Cations. *Annu. Rev. Pharmacol. Toxicol.* **2007**, *47* (1), 629–656.
(97) Smith, R. A. J.; Porteous, C. M.; Gane, A. M.; Murphy, M. P. Delivery of Bioactive Molecules to Mitochondria in Vivo. *Proc. Natl. Acad. Sci.* **2003**, *100* (9), 5407–5412.
(98) Kelso, G. F.; Porteous, C. M.; Coulter, C. V.; Hughes, G.; Porteous, W. K.; Ledgerwood, E. C.; Smith, R. A. J.; Murphy, M. P. Selective Targeting of a Redox-Active Ubiquinone to Mitochondria within Cells: Antioxidant and Antiapoptotic Properties. *J. Biol. Chem.* **2001**, *276* (7), 4588–4596.
(99) Ross, M. F.; Kelso, G. F.; Blaikie, F. H.; James, A. M.; Cochemé, H. M.; Filipovska, A.; Da Ros, T.; Hurd, T. R.; Smith, R. A. J.; Murphy, M. P. Lipophilic Triphenylphosphonium Cations as Tools in Mitochondrial Bioenergetics and Free Radical Biology. *Biochem.* **2005**, *70* (2), 222–230.
(100) Cochemé, H. M.; Murphy, M. P. Complex I Is the Major Site of Mitochondrial Superoxide Production by Paraquat. *J. Biol. Chem.* **2008**, *283* (4), 1786–1798.
(101) Brozovic, A.; Ambriović-Ristov, A.; Osmak, M. The Relationship between Cisplatin-Induced Reactive Oxygen Species, Glutathione, and BCL-2 and Resistance to Cisplatin. *Crit. Rev. Toxicol.* **2010**, *40* (4), 347–359.
(102) Dasari, S.; Bernard Tchounwou, P. Cisplatin in Cancer Therapy: Molecular Mechanisms of Action. *Eur. J. Pharmacol.* **2014**, *740*, 364–378.
(103) Miller, W. H.; Schipper, H. M.; Lee, J. S.; Singer, J.; Waxman, S. Mechanisms of Action of Arsenic Trioxide. *Cancer Res.* **2002**, *62*, 3893–3903.
(104) Zheng, C.-Y.; Lam, S.-K.; Li, Y.-Y.; Ho, J. Arsenic Trioxide-Induced Cytotoxicity in Small Cell Lung Cancer via Altered Redox Homeostasis and Mitochondrial Integrity. *Int. J. Oncol.* **2015**, 1067–1078.
(105) Kallio, a.; Zheng, a.; Dahllund, J.; Heiskanen, K. M.; Härkönen, P. Role of Mitochondria in Tamoxifen-Induced Rapid Death of MCF-7 Breast Cancer Cells. *Apoptosis* **2005**, *10* (6), 1395–1410.
(106) Moreira, P. I.; Custódio, J.; Moreno, A.; Oliveira, C. R.; Santos, M. S. Tamoxifen and Estradiol Interact with the Flavin Mononucleotide Site of Complex I Leading to

Mitochondrial Failure. *J. Biol. Chem.* **2006**, *281* (15), 10143–10152.
(107) Godwin, A. K.; Meister, A.; O'Dwyer, P. J.; Huang, C. S.; Hamilton, T. C.; Anderson, M. E. High Resistance to Cisplatin in Human Ovarian Cancer Cell Lines Is Associated with Marked Increase of Glutathione Synthesis. *Proc. Natl. Acad. Sci. U. S. A.* **1992**, *89* (7), 3070–3074.
(108) Weber, T.; Lu, M.; Andera, L.; Lahm, H.; Gellert, N.; Fariss, M. W.; Korinek, V.; Sattler, W.; Ucker, D. S.; Terman, A.; et al. Vitamin E Succinate Is a Potent Novel Antineoplastic Agent with High Selectivity and Cooperativity with Tumor Necrosis Factor Related Apoptosis-Inducing Ligand (Apo2 Ligand) in Vivo. *Clin. Cancer Res.* **2002**, *8* (3), 863–869.
(109) Neuzil, J. Alpha-Tocopheryl Succinate Epitomizes a Compound With a Shift in Biological Activity Due To Pro-Vitamin-To-Vitamin Conversion. *Biochem. Biophys. Res. Commun.* **2002**, *293* (5), 1309–1313.
(110) Koudelka, S.; Turanek Knotigova, P.; Masek, J.; Prochazka, L.; Lukac, R.; Miller, A. D.; Neuzil, J.; Turanek, J. Liposomal Delivery Systems for Anti-Cancer Analogues of Vitamin E. *J. Control. Release* **2015**, *207*, 59–69.
(111) Thayyullathil, F.; Chathoth, S.; Hago, A.; Patel, M.; Galadari, S. Rapid Reactive Oxygen Species (ROS) Generation Induced by Curcumin Leads to Caspase-Dependent and -Independent Apoptosis in L929 Cells. *Free Radic. Biol. Med.* **2008**, *45* (10), 1403–1412.
(112) Numsen, H. Mitochondrial Reactive Oxygen Species Affect Sensitivity to Curcumin-Induced Apoptosis. *Free Radic. Biol. Med.* **2008**, *44* (7), 1382–1393.
(113) Kuehl, P. J.; Hoye, W. L.; Myrdal, P. B. Preformulation Studies on Imexon. *Drug Dev. Ind. Pharm.* **2006**, *32* (6), 687–697.
(114) Iyengar, B. S.; Dorr, R. T.; Remers, W. a. Chemical Basis for the Biological Activity of Imexon and Related Cyanoaziridines. *J. Med. Chem.* **2004**, *47* (1), 218–223.
(115) Dvorakova, K.; Waltmire, C. N.; Payne, C. M.; Tome, M. E.; Briehl, M. M.; Dorr, R. T. Induction of Mitochondrial Changes in Myeloma Cells by Imexon. *Blood* **2001**, *97* (11), 3544–3551.

# Chapter 2 : Mitochondrial $H_2O_2$ generation using a tunable chemogenetic tool to perturb redox homeostasis in human cells and induce cell death

Among reactive oxygen species (ROS), $H_2O_2$ alone acts as a signaling molecule that promotes diverse phenotypes depending on the intracellular concentration. Mitochondria have been suggested as both sources and sinks of cellular $H_2O_2$, and mitochondrial dysfunction has been implicated in diseases such as cancer. A genetically-encoded $H_2O_2$ generator, D-amino acid oxidase (DAAO), was targeted to the mitochondria of human cells, and its utility in investigating cellular response to a range of $H_2O_2$ doses over time was assessed. Organelle-specific peroxiredoxin dimerization and protein S-glutathionylation were measured as indicators of increased $H_2O_2$ flux due to the activity of DAAO. Cell death was observed in a concentration- and time-dependent manner, and protein oxidation shifted in localization as the dose increased. This work presents the first systematic study of $H_2O_2$-specific perturbation of mitochondria in human cells, and it reveals a marked sensitivity of this organelle to increases in $H_2O_2$ in comparison with prior studies that targeted the cytosol.

## 2.1 Introduction

Hydrogen peroxide ($H_2O_2$) is a member of a family of molecules known as reactive oxygen species (ROS) and has been demonstrated to induce proliferation, differentiation, and cell death [1,2]. Among ROS, $H_2O_2$ is known to behave as a classical signaling molecule, undergoing specific reactions with cysteine residues to cause various downstream effects [3–5]. It has been observed that the intracellular level of $H_2O_2$ determines phenotypic outcome, so controlled modulation of $H_2O_2$ concentration is desirable in order to probe cellular response [4]. Previous studies have investigated cytoplasmic generation of $H_2O_2$ and found either no toxic effects[6] or only partial toxicity with surprisingly large and lengthy perturbations[7].

It is thought that subcellular localization of $H_2O_2$ generation, in addition to concentration, determines downstream effects[1,4]. The need for mechanistic studies exploring the effects of targeted, intracellular $H_2O_2$ generation has already been identified, as the network of antioxidant reactions confine $H_2O_2$ to a small area near its generation site [8–11]. This limitation imposed by the interplay of reaction and diffusion rates within the cell highlights the difference between extracellular bolus addition and intracellular peroxide generation [11,12]. Mitochondria are a compelling organelle for study because they have been suggested as both sources and sinks of intracellular ROS, as well as a hypothesized site for redox signaling [5,13,14]. Mitochondria generate superoxide ($O_2^{\bullet-}$) at various points in the electron transport chain (ETC) as well as in the Kreb's cycle, after which it is quickly converted to $H_2O_2$ by manganese superoxide dismutase (MnSOD) [5]. The $H_2O_2$ levels are managed by the mitochondrial antioxidant network, which is dominated by the 2-cysteine peroxidase Peroxiredoxin 3 (Prx-3) [5,15].

Notably, mitochondrial $H_2O_2$ has been implicated in the onset of apoptosis as well as several diseases, such as cancer and diabetes; as such, some therapeutics have targeted mitochondria and mitochondrial ROS [13,16–18]. However, a dose-response relationship between mitochondrial $H_2O_2$ and cell phenotype, as well as the kinetics involved in this interaction, have not been well established. Synthetic biology tools provide access to this information, enabling elucidation of the strength and activities of compartment-specific networks of antioxidant reactions. In our previous work, we used tunable tools in the cytosol of human epithelial cells to establish the concentration- and time-dependence of $H_2O_2$-induced cell death [7]. We observed only partial toxicity (<50%) as a result of these cytosolic $H_2O_2$ perturbations. Here, we extend this approach to mitochondria, enabling a comparison of cellular responses to compartment-specific perturbations.

## 2.2 Methods

*2.2.1 : Cell Culture*

HeLa cells were a generous gift from Dane Wittrup, and were maintained in Dulbecco's modified Eagle's medium (DMEM; Lonza) supplemented with 10% fetal bovine serum (FBS; ATCC) at 37 °C in a humidified atmosphere of 5% $CO_2$. Cells were passaged every three to six days, depending on growth rate. Stable cell lines created by lentivirus transfection using a synthetic construct were maintained in medium containing 6 μg/mL puromycin (Sigma) to apply selective pressure.

*2.2.2 : Creation of Stable Cell Lines*

A plasmid encoding HyPer with a mitochondrial localization tag (HyPer-mito) was purchased from Evrogen. A plasmid encoding D-amino acid oxidase with a mitochondrial localization tag (DAAO-mito) was a gift from Rajiv Ratan (Weill Medical College of Cornell University, USA). HyPer-mito and DAAO-mito were sub-cloned from their original vectors into the lentiviral transfer plasmid PLJM1-EGFP (Addgene plasmid #19319), replacing the EGFP gene between the NheI and EcoRI restriction sites. HEK293 FT cells (ATCC) were seeded at $7.5x10^5$ cells/35mm well and allowed to grow for two days until 90% confluent. The PLJM1 transfer vector containing the appropriate gene insert was co-transfected for 18 hours in OptiMEM (Invitrogen) with the packaging plasmids psPAX2 and pMD2.G (Addgene plasmids #12260 and #12259) in a ratio 3:2:1 and a total of 5 μg plasmid and 10 μg Lipofectamine 2000 (Invitrogen). Following transfection, the OptiMEM was replaced with 1 mL DMEM supplemented with 10% FBS for virus collection; viruses were harvested every 24 hours for two days. HeLa cells were seeded at a density of $3.5x10^5$ cells/35mm well and grown for 24 hours until 80-90% confluent in preparation for transfection. 1 mL virus-containing medium plus 6 μg/mL polybrene (Sigma) was added to the HeLa well for 24 hours. Cells were allowed to recover in DMEM supplemented with 10% FBS

for two days, at which point they were expanded into a 10 cm dish for selection in DMEM supplemented with 10% FBS plus 6 μg/mL puromycin.

*2.2.3 : Mitochondrial Generation of $H_2O_2$ Using D-amino Acid Oxidase*

HeLa cells co-transfected with HyPer-mito and DAAO-mito were seeded at $3.5x10^5$ cells/well in 35 mm dishes or 6-well plates, $1.75x10^5$ cells/well in 12-well plates coated with poly-L-lysine (Sigma), or $2x10^4$ cells/well in 96-well plates 24 hours prior to the start of generation. For confocal imaging experiments, cells were grown on 12 mm round coverslips coated with poly-L-lysine (Fisher Scientific) seeded at $8.75x10^4$ cells/well. Cells were washed once with 1x PBS then exposed to 5 μM FAD (Sigma) and concentrations of D-alanine (Sigma) from 0 – 50 mM in Roswell Park Memorial Institute 1640 medium (RPMI; Invitrogen) without phenol red. At least 25 cells per time point per condition were imaged.

*2.2.4 : Redox Western Blotting*

The protocols for redox western blotting were adapted from [23]. Prior to lysing, cells grown in 6-well plates were washed with 1x PBS then incubated on ice with 2 mL 100 mM methyl methanethiosulfonate (MMTS; Sigma) for 30 min to block thiols. Cells were lysed with 100 μL lysis buffer (0.5% Triton X-100, 1x HALT protease inhibitors (ThermoFisher), 1x PBS) then lysates were collected and centrifuged at 10,000 xg for 10 min. Supernatants were separated on a non-reducing SDS-PAGE 12% polyacrylamide gel, then transferred to a PVDF membrane for immunoblotting. Blots were blocked with Odyssey blocking buffer (Licor) and incubated overnight at 4 °C with primary antibodies against Prx-2 (R&D Systems, AF3489), Prx-3 (Abcam, Clone# EPR8115), and Hsp60 (R&D Systems, Clone# 264233). Blots were incubated with IR-conjugated secondary antibodies (Licor) for 1 hr at room temperature. For the Western blots showing hyperoxidation, the same protocol was followed, excluding the blocking step with MMTS.

*2.2.5 : Protein S-glutathionylation Immunofluorescence*

After $H_2O_2$ generation experiments, cells were fixed in 4% paraformaldehyde for 30 min. Cells were permeabilized in 0.5% Triton X-100 (Sigma) in 1x PBS for 30 min and blocked in 2% bovine serum albumin (BSA; VWR), 0.5% Triton X-100 in 1x PBS for 30 min. Primary antibody staining with antibodies raised against protein-glutathione conjugates (Abcam, Clone# D8) was performed overnight at 4 °C at a 1:200 dilution. AlexaFluor-488 conjugated (Invitrogen) secondary antibody staining was performed for 45 min at room temperature at a 1:250 dilution. Feature sizes were quantified using a built-in toolbox in ImageJ. We note that we have verified the specificity of the Pr-SSG antibody used here by reducing the mixed disulfides induced by DAAO/D-ala $H_2O_2$ perturbations and observing the expected ablation of fluorescent signal upon immunofluorescent analysis [36].

*2.2.6 : Cell Viability after Exposure to $H_2O_2$ Produced by DAAO-mito*

For cell counts, at the end of $H_2O_2$ generation experiments, cells were trypisinized and counted by Trypan blue exclusion to obtain live cell counts. For CellTiter Glo, cells were grown in white 96-well plates. Assay was performed according to manufacturer's instructions.

*2.2.7 : Mitochondrial Depolarization Assay*

Prior to treatment of cells with D-alanine, cells were incubated with 200 nM tetramethylrhodamine, ethyl ester (TMRE; ThermoFisher) for 45 min spiked directly into the culture medium. 20 µM Carbonyl cyanide-p-trifluoromethoxyphenylhydrazone (FCCP; Sigma) was used as a positive control for mitochondrial depolarization, and was added 10 min prior to TMRE addition. After dye incubation, cells were washed once with Dulbecco's phosphate buffered saline (DPBS) with calcium and magnesium (ThermoFisher), and then culture medium was replaced with RPMI for $H_2O_2$ generation and imaging. At least four images per condition per

time were taken. TMRE-stained images were quantified using ImageJ by measuring the average fluorescence of the entire field of view.

*2.2.8 : Fluorescence Microscopy*

The ratiometric HyPer-mito signal was captured using an inverted IX81 widefield fluorescence microscope (Olympus) with a 60x/1.42 NA oil-immersion objective lens and Prior Lumen2000 lamp. For the HyPer Short channel, a Chroma 415/30 nm excitation filter was used, and for the HyPer Long channel, a Semrock 488/6 nm excitation filter was used. Emission was collected on a Semrock 525/40 nm filter for both channels. A 250 ms exposure time and 10% lamp intensity was used to generate fluorescent images. Mitochondrial localization was verified using CellLight Mitochondria-RFP, BacMam 2.0 (ThermoFisher) following manufacturer's instructions. TMRE and CellLight Mitochondria-RFP were visualized using a Texas Red filter set from Semrock, 562/40 nm excitation and 624/40 nm emission, and AlexaFluor-488 conjugated secondary antibodies were visualized using a GFP filter set from Semrock, 472/30 nm excitation and 520/35 nm emission. Confocal images were obtained using a FV1000MPE confocal microscope (Olympus) and a 40x/1.25 NA oil-immersion objective lens. Images were exported to ImageJ or MATLAB for post-processing.

*2.2.9 : Quantification and Statistical Analysis*

At least four fields of view per time point per condition were captured for all imaging experiments, encompassing a minimum of 20-70 cells total. The number of cells observed per condition was inversely proportional to the toxicity of the perturbation, as this factor limited the number of cells available for analysis. A minimum of two biological replicates and three technical replicates per experiment were performed (a minimum of four technical replicates for imaging experiments). Analysis of variance (ANOVA) or Welch's ANOVA testing of trends was performed where appropriate using the Excel Real Statistics add-in. The null hypothesis in this

case is that all sample means for all concentrations of D-ala assayed are equal. One-tailed Student's t tests were calculated using the built-in Excel statistics toolbox.

## 2.3 Results

We have implemented a tunable chemogenetic tool, a D-amino acid oxidase construct targeted to the mitochondrial matrix (DAAO-mito)[19] (Figure 2.1a), to systematically study the effects of elevated mitochondrial $H_2O_2$. Thus far, this tool has not been used in the mitochondria, so it is not yet understood how these perturbations might affect cells' downstream phenotypes. DAAO reacts with D-amino acids and oxygen to generate imino acids and $H_2O_2$ using flavin adenine dinucleotide (FAD) as a cofactor (Figure 2.1b). Here, we have used D-alanine (D-ala) to control the onset and amount of $H_2O_2$ produced. DAAO's reaction with D-ala is characterized by a Michaelis-Menten constant, $K_m$, in the mM concentration regime [20]. We stimulated cells with a range of $H_2O_2$ doses by supplying D-ala at concentrations ranging from 0 – 50 mM over periods of up to 6.5 hours. D-ala alone is not toxic to HeLa cells even at the highest concentration and time combination used (Figure 2.1c) so it is a viable substrate for these experiments. To validate the function of the tool in the mitochondria, cells were analyzed as a function of time for post-translational protein modifications that provide evidence of $H_2O_2$ generation. After dose-response trends were observed in two different kinds of molecular measurements, changes in mitochondrial morphology and membrane potentials, as well as phenotypic responses of cells to a range of perturbations were assessed. In order to monitor the morphological changes that took place as cells were perturbed with $H_2O_2$, the $H_2O_2$ biosensor HyPer was targeted to the mitochondria of HeLa cells, as presented in Figure 2.1d [21]. In contrast with destructive analysis techniques such as immunoblotting and immunocytochemistry, HyPer allows live-cell imaging; a commercially-available RFP targeted to the mitochondria was used to verify mitochondrial localization of HyPer-mito (Figure 2.1d). Considering these new results in the context of previous findings, increased

$H_2O_2$ fluxes in the mitochondria are considerably more toxic than increased $H_2O_2$ fluxes in the cytosol, and a mitochondrial permeability transition (MPT) rather than mitochondrial fragmentation accompanies this toxicity.

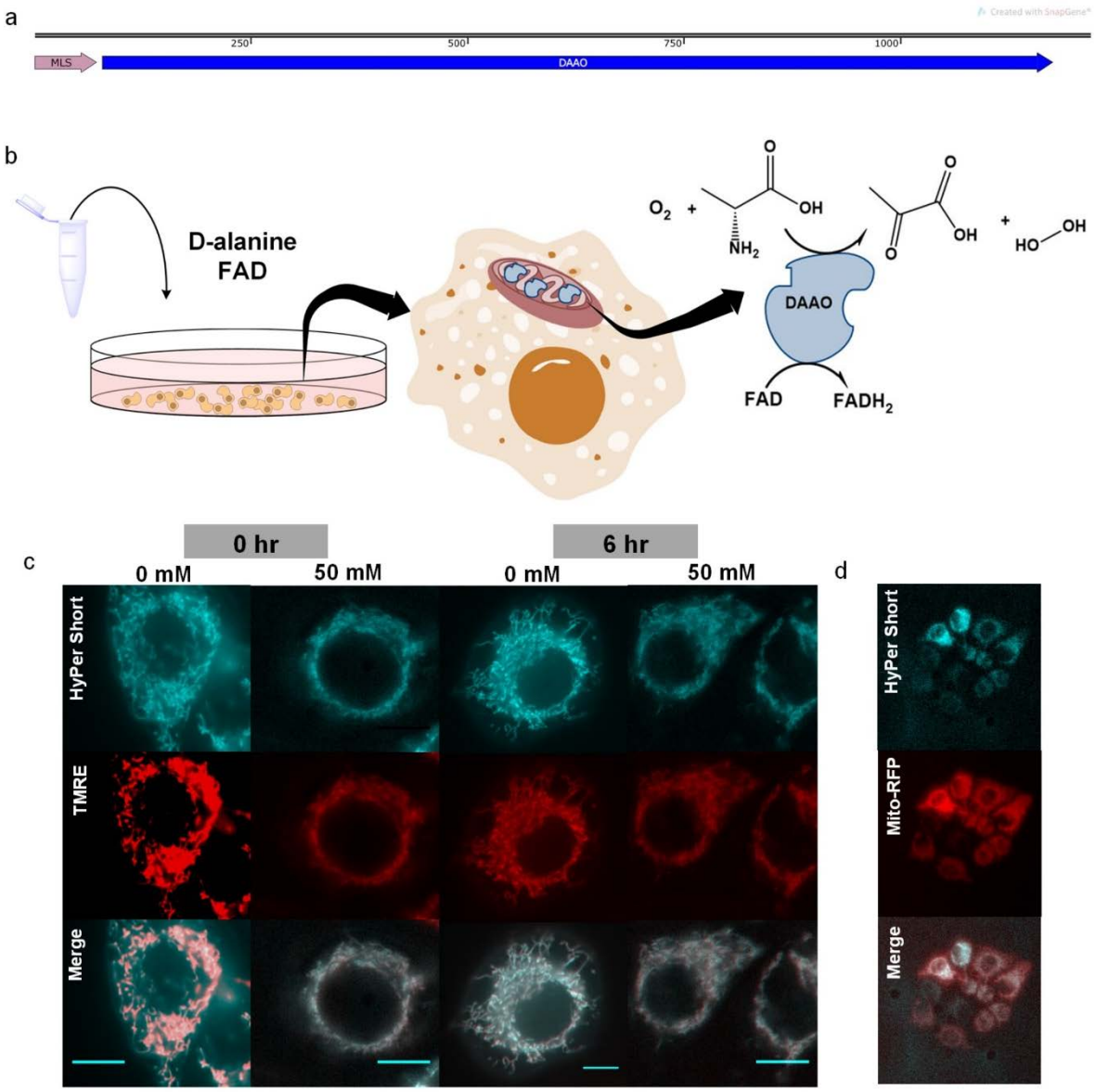


*Figure 2.1: Schematic overview of synthetic construct and experimental mechanism. a) A mitochondrial localization sequence (MLS) on the N-terminus of the DAAO protein codes for the short peptide sequence necessary for protein import to the mitochondrial matrix. b) Cells expressing the synthetic DAAO-mito were exogenously given D-alanine and FAD to induce mitochondrial $H_2O_2$ generation in a dose-response fashion. DAAO performs oxidative deamination on D-alanine to produce pyruvate and $H_2O_2$ using FAD as a cofactor. c) Control cells not expressing DAAO-mito stimulated with 50 mM D-ala for 6.5 hours did not show signs of mitochondrial stress or toxicity. Scale bars represent 50 µm. Full microscopy images are shown in SI Figure S1. d) HeLa cells co-expressing DAAO-mito and HyPer-mito imaged with mito-RFP to verify mitochondrial localization of the biosensor HyPer.*

To assess function of DAAO in the mitochondria, the Peroxiredoxin (Prx) family of proteins was probed using redox Western blotting techniques to detect direct molecular evidence of changes in $H_2O_2$ (Figure 2.2). Increased fluxes of $H_2O_2$ in different organelles is detectable

based on the oxidation status of different Prx isoforms [15,22]. In the cytoplasm, Prx-2 is expected to be the dominant antioxidant in the network involved in clearing physiologically relevant concentrations of $H_2O_2$ [9,11]. Similarly, in the mitochondria, Prx-3 is expected to dominate, with an abundance of 60 μM and a second-order rate constant of $2x10^7$ $M^{-1}s^{-1}$ [5,15]. Catalase, the most familiar scavenger of $H_2O_2$, is generally not found in mitochondria, or is found at concentrations nearly four orders of magnitude lower than Prx-3 in specialized tissues, so it is not expected to contribute appreciably to the mitochondrial antioxidant network [5,15]. Similarly, Glutathione peroxidase 1 (Gpx 1) is present at an order of magnitude lower concentration than Prx-3, so despite the fact that the second-order rate constant of Gpx 1 is similarly high at $6x10^7$ $M^{-1}s^{-1}$, it is expected to make at most a minor contribution to the mitochondrial antioxidant network [15].

Redox Western blots were performed on cell lysates to determine the relative changes in reduced and oxidized Prx-2 and Prx-3 across the different treatments, as schematically depicted in Figure 2.2a. Methyl methanethiosulfonate (MMTS) was reacted with cultures prior to lysis to convert sulfhydryl groups to -SS-$CH_3$ groups (Figure 2.2b), so increases in the dimer Prx species from the 0 mM D-ala are indicators of intracellular $H_2O_2$ fluxes rather than lysis-induced oxidation artifacts. Analogously, the reduced status of monomers is preserved. Analysis of mitochondrial Prx-3 in Figure 2.2b demonstrates that, as more peroxide was generated, the amount of monomer decreased, with a resulting increase in the amount of dimer. This finding is consistent with what one would expect from the local action of $H_2O_2$. In the cytoplasm, at low doses of $H_2O_2$, there was an increase from control in the dimer band of Prx-2. Interestingly, however, the dimer bands disappeared at higher levels of $H_2O_2$, implying either suddenly low levels of $H_2O_2$ or hyperoxidation, as Prx-2 cannot dimerize when its thiol has been hyperoxidized to a sulfinic or sulfonic acid [3,23]. To confirm whether this was indeed hyperoxidation and not simply reduced Prx-

2, a Western blot was performed without any MMTS thiol-blocking steps prior to cell lysis; disappearance of the dimer indicates hyperoxidation [23]. This methodology following the protocol established by Cox *et al.* was preferred over blotting with antibodies specific to the sulfinic/sulfonic forms of Prx because existing antibodies are not specific to particular Prx isoforms, ergo all compartment-specific information is lost [23]. Figure 2.2c depicts the results of the hyperoxidation blot, which confirm that at low levels of $H_2O_2$ generation in the mitochondria, Prx-2 did not differ from control, but at higher levels of $H_2O_2$, Prx-2 became hyperoxidized in the cytoplasm. These results suggest that large amounts of $H_2O_2$ were present in the cytoplasm above some threshold of mitochondrial $H_2O_2$ generation, as more than 150 nM of cytosolic $H_2O_2$ (~100 μM external bolus) would be necessary to induce this reaction [24]. In summary, redox (+MMTS) and hyperoxidation (-MMTS) Western blots of Prx-3 (mitochondrial) and Prx-2 (cytosolic) oxidation states validated the function of DAAO-mito in elevating $H_2O_2$ flux in the mitochondria, and increases in $H_2O_2$ flux appeared to correlate with the concentration of D-ala, substrate of DAAO.

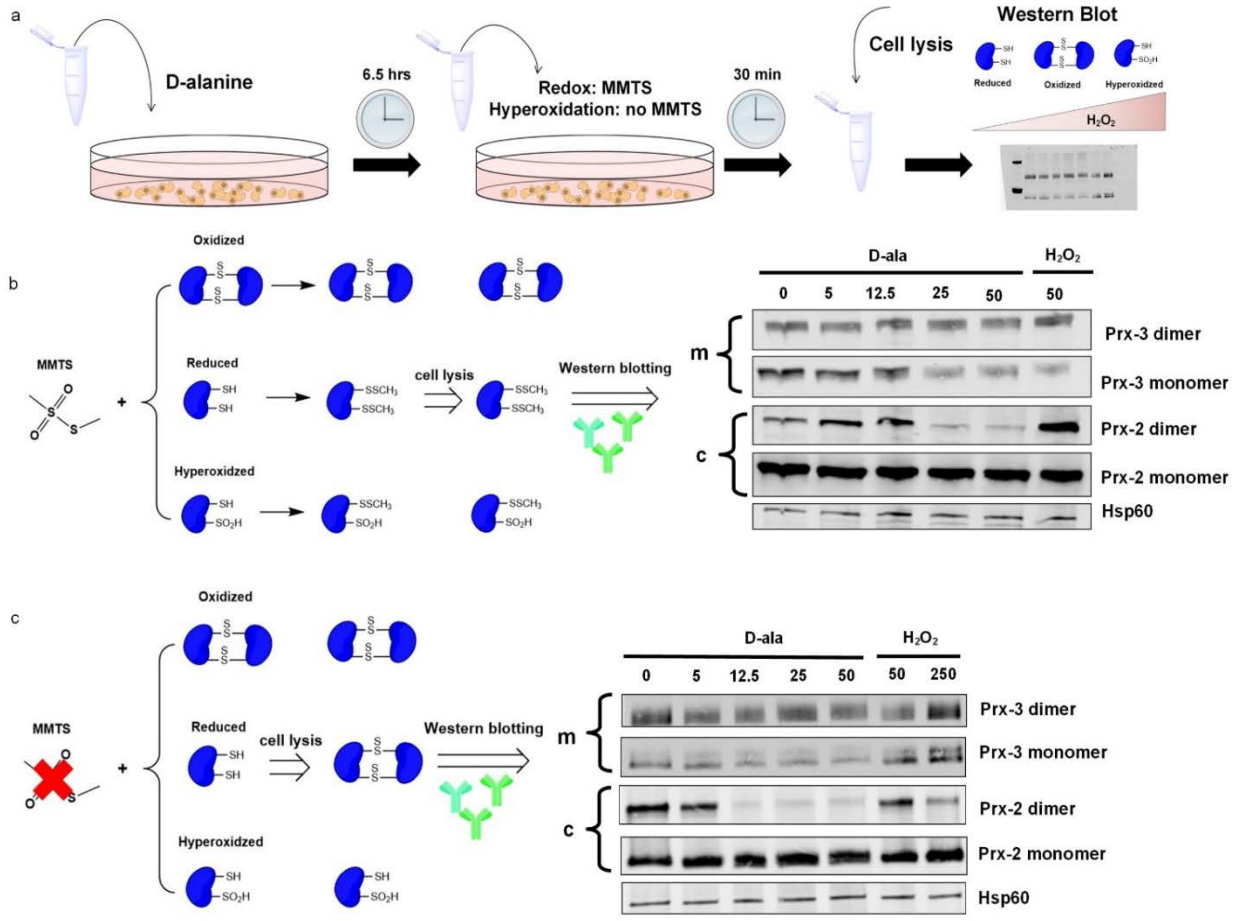


*Figure 2.2: Redox Western Blots Demonstrate Increasing Mitochondrial and Cytoplasmic $H_2O_2$ upon Stimulation of DAAO-mito Cells with D-ala. a) HeLa cells co-expressing HyPer-mito and DAAO-mito were stimulated with the indicated concentration of D-ala (mM) for 6.5 hours or given the indicated bolus of H2O2 (μM) as a positive control. Then cells were either blocked with the alkylating agent methyl methanethiosulfonate (MMTS), which reacts with free thiols (Redox western blot, b), prior to cell lysis or lysed without alkylating agents (Hyperoxidation western blot, c). b) Redox blots for Prx-3 and Prx-2. Dimerized species indicate oxidation, as indicated in the schematic. The disappearance of the Prx-2 dimer at higher concentrations of D-ala suggests hyperoxidation, implying high concentrations of H2O2 in the cytosol. c) Hyperoxidation blots, where disappearance of dimer species indicates hyperoxidation, as indicated in the schematic. Suspected hyperoxidation from b) is confirmed by the disappearance of the Prx-2 dimers. Corresponding densitometry plots, tabulates densitometry data, and full blot images for both b) and c) are presented in SI Figures S2-S7 and Table S1.*

To further validate the function of the tool and test for dose-dependent molecular modifications of proteins, we examined protein S-glutathionylation (Pr-SSG). This post-translational modification results when a cysteine residue of a protein is oxidized by $H_2O_2$ to form a sulfenic acid. The sulfenic acid form of the protein then reacts with glutathione to form a disulfide linkage between the protein and glutathione (Pr-SSG). Protein S-glutathionylation has been hypothesized to be important in the redox regulation of mitochondria. The primary proposed role

for Pr-SSG is to protect proteins from further oxidation; the mixed disulfide bond with glutathione is readily reduced by glutaredoxin (Grx), whereas a sulfinic or sulfonic acid is not so easily reversed. It has also been proposed that Pr-SSG regulates protein function as a post-translational modification, especially in the mitochondria [25]. Cells were therefore probed for Pr-SSG conjugates using immunofluorescence. Figure 2.3 demonstrates that, as $H_2O_2$ dose increases due to stimulation of DAAO-mito with D-ala, the abundance of Pr-SSG increases as well. In addition, the pattern of Pr-SSG shifts from localized at low $H_2O_2$ concentrations to ubiquitous at high $H_2O_2$ concentrations; the single-cell images in Figure 2.3b better illustrate this change. The distribution of feature sizes is shown in Figure 2.3d, and demonstrates a marked shift from small features at low D-ala concentrations, to distributions that span several orders of magnitude at 25 mM, shown by the peak flattening as D-ala concentration increases. This finding suggests that at low levels, the effects of $H_2O_2$ signaling are localized, but at high levels, those effects are no longer confined to subcellular regions. Additionally, the observed staining pattern coupled with the changes in Prx oxidation suggest some kind of threshold in cellular response between 12.5 and 25 mM D-ala.

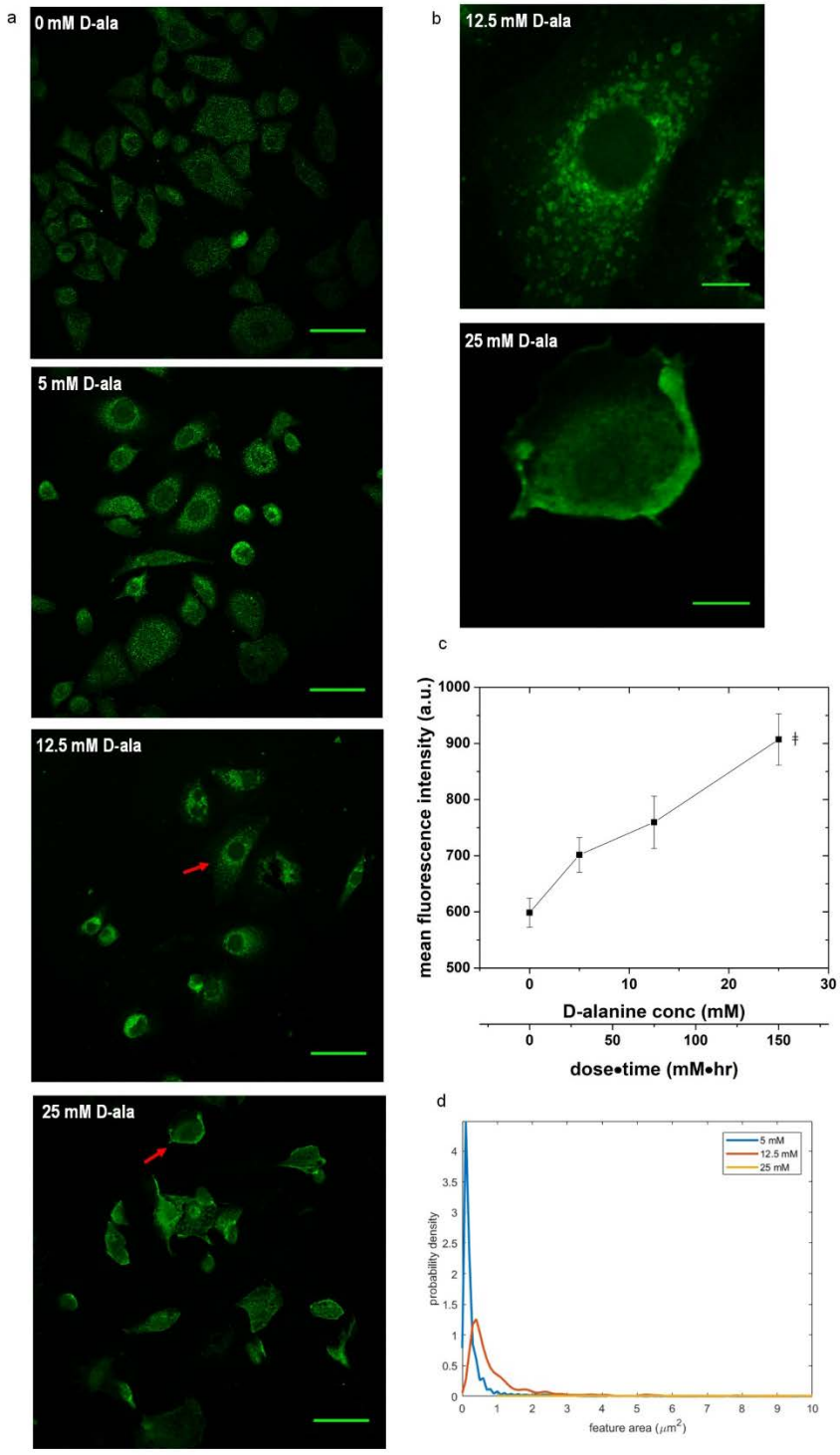


*Figure 2.3: Pr-SSG Abundance and Localization Depends on $H_2O_2$ Dose. a) HeLa cells co-expressing HyPer-mito and DAAO-mito stimulated with the indicated concentration of D-ala for 6 hours, labeled with an antibody specific for protein-GSH conjugates. Signal at 0 mM D-ala indicates baseline Pr-SSG. Scale bars represent 50 μm. b) Close-up of cells indicated by red arrows in a. Scale bar represents 10 μm. c) Mean fluorescence intensity vs. D-ala concentration of the cells stained for Pr-SSG. Points represent mean ± SEM of the cells across four fields of view. ǂ denotes $P<0.005$ by ANOVA. d) Probability distribution of feature sizes identified by Pr-SSG staining, given by the area in $\mu m^2$.*

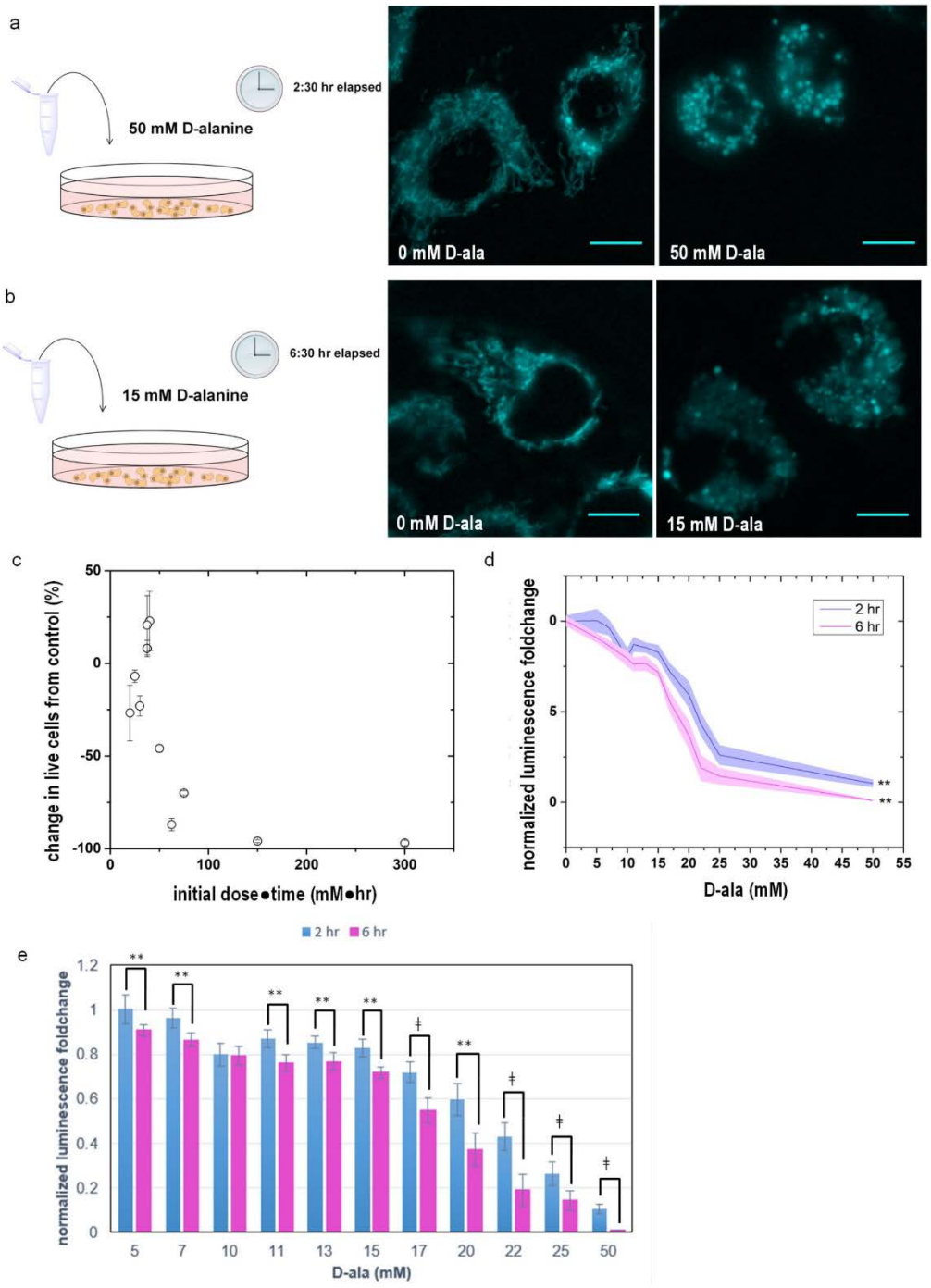


*Figure 2.4: Localizing a $H_2O_2$* Perturbation to the Mitochondria Causes Morphological Changes and Cell Death. *a) HeLa cells co-expressing HyPer-mito and DAAO-mito stimulated with 50 mM D-ala for 2.5 hours. b) HeLa cells co-expressing HyPer-mito and DAAO-mito stimulated with 15 mM D-ala for 6.5 hours. Additional microscopy images for a) and b) can be found in SI Figure S8. c) Decrease in live cells as measured by Trypan blue exclusion compared to control (0 mM D-ala) vs. the initial dose of D-ala multiplied by treatment time (mM·hr). Points represent mean ± SEM. d) Normalized luminescence foldchange, as measured by CellTiter Glo, for cells treated with D-ala for 2 hours (blue) and 6 hours (magenta). Lower luminescence corresponds to lower cell viability. Lines represent the average of 16 cultures, and shaded regions represent SEM. ** denotes P<0.05 for ANOVA. e) Data from d represented as a bar chart to more clearly show the differences between 2 and 6 hours. ** denotes P<0.05, ǂ denotes P<0.001 for one-tailed t-test.*

Once specific, molecular evidence of $H_2O_2$-mediated reactions had been established, it was next of interest to investigate downstream phenotypic responses, including morphological changes to mitochondria as well as cell fate decisions. Unperturbed cells displayed a string-like mitochondrial morphology, consistent with published descriptions of healthy mitochondria (Figure 2.4b-c, 0 mM D-ala) [26]. Cells co-expressing DAAO-mito and HyPer-mito were monitored at various intervals over the generation periods, up to 7 hours, with D-ala concentrations of 0 – 50 mM to note any changes. Figure 2.4 depicts representative results of these experiments, with Figure 2.4a showing a short, high intensity D-ala perturbation and Figure 2.4b showing a longer, lower intensity D-ala perturbation. At shorter generation times, the highest concentrations of $H_2O_2$ had induced drastic morphological changes (Figure 2.4a) and cell detachment. Mitochondria became swollen and punctate, consistent with qualitative signs of mitochondrial stress. Lower concentrations of $H_2O_2$ did not induce these morphological changes until longer generation times (Figure 2.4b). This was indicative of a temporal component to $H_2O_2$-induced toxicity in the mitochondria, consistent with previous findings in the cytoplasm [7]. Change in live cells is plotted as a function of D-ala dose·time [mM·hr] in Figure 2.4c for all perturbations, demonstrating a trend of increasing toxicity with increasing dose·time combinations, with a 98% decrease in cell survival observed with the highest dose·time combination of 300 mM·hr. This trend is echoed in the cell viability data obtained by CellTiter Glo assay, depicted in Figure 2.4d-e. Holding dosing time constant, cell viability decreases as a function of D-ala concentration, plotted in Figure 4d. On the other hand, holding concentrations constant, cell viability also decreases as a function of dosing time, depicted in the bar chart in Figure 2.4e. Though we calculated HyPer ratios during these experiments and observed an increasing trend with increasing D-ala concentration, cell-to-cell heterogeneity made the probe more useful for observing morphological changes than for exact

quantification of $H_2O_2$ in these long-term experiments where monitoring individual cells for the duration of the experiment was not practical (SI Figures S9 – S10).

Punctate mitochondrial morphology and mitochondrial swelling is typical of cell stress [27]**.** A mitochondrial depolarization assay was performed in order to attribute this morphological change to mitochondrial fragmentation or mitochondrial permeability transition (MPT); an increase in mitochondrial polarization would indicate the former, while a decrease implies the latter [26,28]. As demonstrated in Figure 2.5, using the cationic lipophilic dye tetramethylrhodamine ethyl ester (TMRE), mitochondria were initially polarized, indicated by the bright TMRE fluorescence. As $H_2O_2$ was generated, polarization was lost, as indicated by the loss in TMRE fluorescence signal. The dark panel at 50 mM D-ala (325 mM·hr) in Figure 2.5a indicates the complete depolarization at the highest dose of $H_2O_2$ assayed, demonstrating that mitochondria became completely depolarized over the investigated dose range. The plot in Figure 2.5b marks the trend of decreasing TMRE fluorescence as the mitochondria were exposed to increasing doses of $H_2O_2$. These data are consistent with changes associated with the MPT.

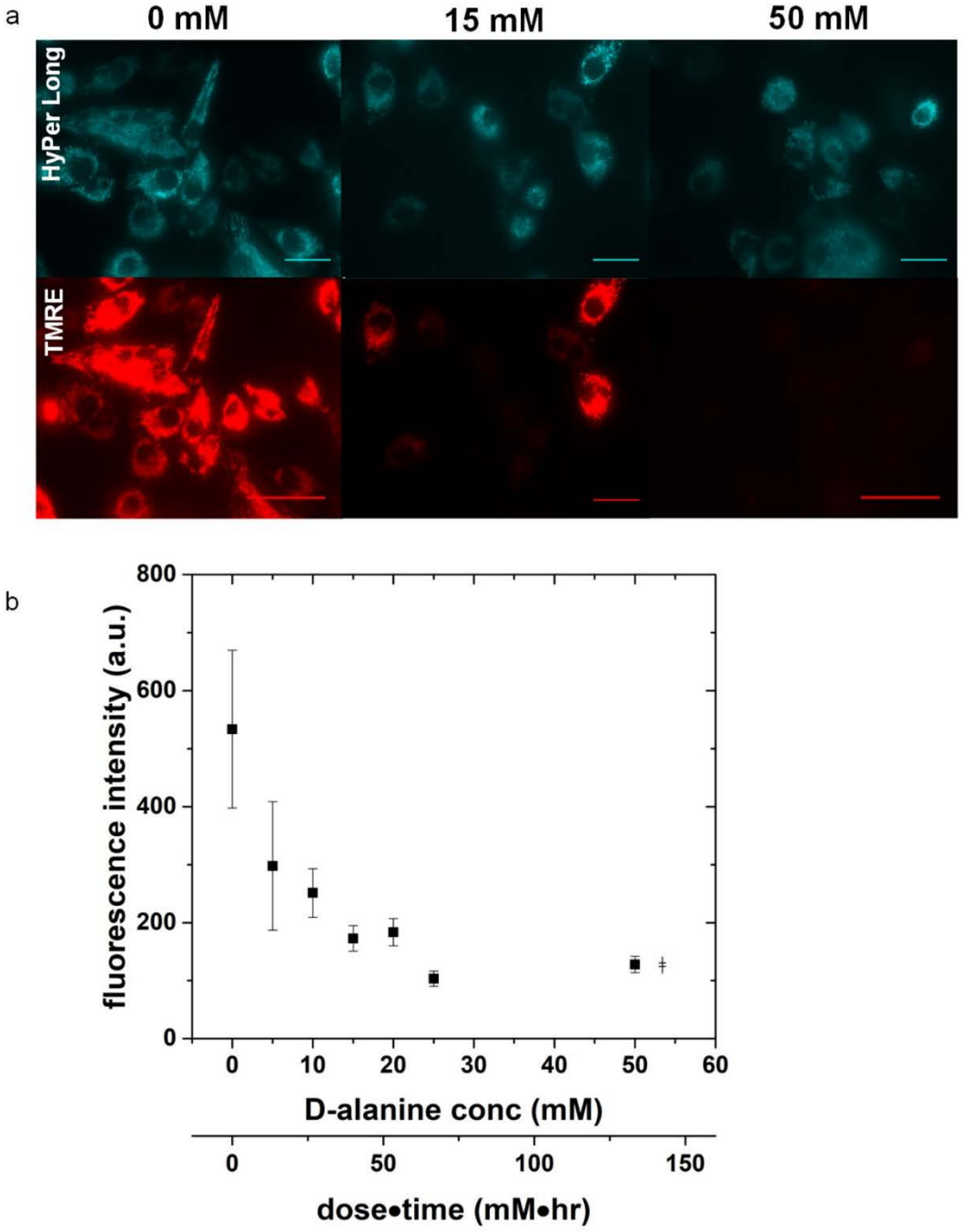


*Figure 2.5: Mitochondrial Depolarization Assay Consistent with MPT. a) HeLa cells co-expressing HyPer-mito and DAAO-mito stimulated with the indicated concentration of D-ala for 6.5 hr. More concentrations shown in SI Figure S11. HyPer Long signal shown on the top row and TMRE signal shown on the bottom row. Scale bars represent 50 μm. b) Trend in average TMRE signal across D-ala doses after 2.75 hr of stimulation. Points represent mean ± SEM of at least four fields of view. ǂ indicates $P<0.005$ by ANOVA.*

## 2.4 Discussion

Uncovering the signaling reactions underlying the mechanism of cell death initiated by mitochondrial $H_2O_2$ generation is an intriguing line of study prompted by these results. Understanding how the cell death signal is being transmitted, and which proteins are involved, will enable better manipulation of the cellular environment for therapeutic purposes. Several proteins in the mitochondria are hypothesized to be redox-sensitive and targets for signaling via $H_2O_2$, including the adenine nucleotide translocase (ANT), which plays a role in the mitochondrial permeability transition pore (MPTP) [29]. In addition, Prx-3 itself is thought to play a role in signal transduction [5,15,30]. The transcription factor signal transducer and activator of transcription 3 (STAT3) has also been described as a redox-responsive signaling molecule, responding to changes in $H_2O_2$ levels throughout the cell and propagating the signal downstream [31,32]. STAT3 is now thought to play several important roles in the mitochondria, including regulation of the MPTP [31]. While there are missing links in how the cell converts the input of $H_2O_2$ into a cell death signal, this work has demonstrated the ability to make controlled perturbations in order to study these pathways mechanistically. Investigating spatiotemporal aspects of $H_2O_2$ reactions and signaling will provide important supplementary information to existing bolus-addition-based experiments.

Finally, one of the most notable aspects of this work is the dramatic increase in cell death with $H_2O_2$ generation in the mitochondria compared to control. Previous work in the cytoplasm demonstrated at most an approximately 45% increase in toxicity compared to control, much lower than the 98% decrease in survival observed with mitochondrial localization, even with shorter generation times [7]. It is thought that redox-based therapeutics work by raising the levels of intracellular oxidants, though the mechanisms are only beginning to be understood. This work suggests that redox-based chemotherapeutics may be more deleterious to cells if targeted to the

mitochondria, as previously hypothesized [33]. Efforts exist to both target existing redox-active compounds to the mitochondria and also understand the mechanisms of compounds that seem to act via the mitochondria [34,35]. Making controlled perturbations with a peroxide generator has been useful in elucidating drug mechanisms in the cytoplasm, and could be a key tool in understanding chemotherapeutics in the mitochondria [36].

## 2.5 References


(1) Sies, H. (2017) Hydrogen peroxide as a central redox signaling molecule in physiological oxidative stress: Oxidative eustress. *Redox Biol. 11*, 613–619.
(2) D'Autréaux, B., and Toledano, M. B. (2007) ROS as signalling molecules: mechanisms that generate specificity in ROS homeostasis. *Nat. Rev. Mol. Cell Biol. 8*, 813–824.
(3) Lennicke, C., Rahn, J., Lichtenfels, R., Wessjohann, L. A., and Seliger, B. (2015) Hydrogen peroxide – production, fate and role in redox signaling of tumor cells. *Cell Commun. Signal. 13*, 39.
(4) Gough, D. R., and Cotter, T. G. (2011) Hydrogen peroxide: a Jekyll and Hyde signalling molecule. *Cell Death Dis. 2*, e213.
(5) Rhee, S. G., and Kil, I. S. (2016) Mitochondrial H2O2 signaling is controlled by the concerted action of peroxiredoxin III and sulfiredoxin: Linking mitochondrial function to circadian rhythm. *Free Radic. Biol. Med. 100*, 73–80.
(6) Matlashov, M. E., Belousov, V. V., and Grigori, E. (2014) How Much H2O2 Is Produced by Recombinant D-Amino Acid Oxidase in Mammalian Cells? *Antioxid. Redox Signal. 20*, 1039–44.
(7) Huang, B. K., Stein, K. T., and Sikes, H. D. (2016) Modulating and Measuring Intracellular H 2 O 2 Using Genetically Encoded Tools to Study Its Toxicity to Human Cells. *ACS Synth. Biol. 5*, 1389–1395.
(8) Liou, G.-Y., and Storz, P. (2010) Reactive oxygen species in cancer. *Free Radic. Res. 44*, 479–496.
(9) Lim, J. B., Huang, B. K., Deen, W. M., and Sikes, H. D. (2015) Analysis of the lifetime and spatial localization of hydrogen peroxide generated in the cytosol using a reduced kinetic model. *Free Radic. Biol. Med. 89*, 47–53.
(10) Lim, J. B., Langford, T. F., Huang, B. K., Deen, W. M., and Sikes, H. D. (2016) A reaction-diffusion model of cytosolic hydrogen peroxide. *Free Radic. Biol. Med. 90*, 85–90.
(11) Winterbourn, C. C. (2008) Reconciling the chemistry and biology of reactive oxygen species. *Nat. Chem. Biol. 4*, 278–286.
(12) Sobotta, M. C., Barata, A. G., Schmidt, U., Mueller, S., Millonig, G., and Dick, T. P. (2013) Exposing cells to H2O2: A quantitative comparison between continuous low-dose and one-time high-dose treatments. *Free Radic. Biol. Med. 60*, 325–335.
(13) Kang, J., and Pervaiz, S. (2012) Mitochondria: Redox Metabolism and Dysfunction. *Biochem. Res. Int. 2012*, 1–14.
(14) Shadel, G. S., and Horvath, T. L. (2015) Mitochondrial ROS Signaling in Organismal Homeostasis. *Cell 163*, 560–569.
(15) Cox, A. G., Winterbourn, C. C., and Hampton, M. B. (2010) Mitochondrial peroxiredoxin

involvement in antioxidant defence and redox signalling. *Biochem. J. 425*, 313–325.
(16) Cao, X., Zhao, S., Liu, D., Wang, Z., Niu, L., Hou, L., and Wang, C. (2011) ROS-Ca2+ is associated with mitochondria permeability transition pore involved in surfactin-induced MCF-7 cells apoptosis. *Chem. Biol. Interact. 190*, 16–27.
(17) Milane, L., Trivedi, M., Singh, A., Talekar, M., and Amiji, M. (2015) Mitochondrial Biology, Targets, and Drug Delivery. *J. Control. Release 207*, 40–58.
(18) Sullivan, L. B., and Chandel, N. S. (2014) Mitochondrial reactive oxygen species and cancer. *Cancer Metab. 2*, 17.
(19) Alim, I., Haskew-Layton, R. E., Aleyasin, H., Guo, H., and Ratan, R. R. (2014) Spatial, Temporal, and Quantitative manipulation of Intracellular Hydrogen Peroxide in Cultured Cells. *Methods Enzymol. 547*, 251–273.
(20) Pollegioni, L., Langkau, B., Tischer, W., Ghisla, S., and Pilone, M. S. (1993) Kinetic mechanism of D-amino acid oxidases from Rhodotorula gracilis and Trigonopsis variabilis. *J. Biol. Chem. 268*, 13850–13857.
(21) Belousov, V. V, Fradkov, A. F., Lukyanov, K. A., Staroverov, D. B., Shakhbazov, K. S., Terskikh, A. V, and Lukyanov, S. (2006) Genetically encoded fluorescent indicator for intracellular hydrogen peroxide. *Nat. Methods 3*, 281–286.
(22) Pastor-Flores, D., Becker, K., and Dick, T. P. (2017) Monitoring yeast mitochondria with peroxiredoxin-based redox probes: the influence of oxygen and glucose availability. *Interface Focus 7*, 20160143.
(23) Cox, A. G., Winterbourn, C. C., and Hampton, M. B. (2010) Measuring the Redox State of Cellular Peroxiredoxins by Immunoblotting, in *Methods in enzymology* 1st ed., pp 51–66. Elsevier Inc.
(24) Huang, B. K., and Sikes, H. D. (2014) Quantifying intracellular hydrogen peroxide perturbations in terms of concentration. *Redox Biol. 2*, 955–962.
(25) Mailloux, R. J., and Treberg, J. R. (2016) Protein S-glutathionlyation links energy metabolism to redox signaling in mitochondria. *Redox Biol. 8*, 110–118.
(26) Liesa, M., and Shirihai, O. S. (2013) Mitochondrial dynamics in the regulation of nutrient utilization and energy expenditure. *Cell Metab. 17*, 491–506.
(27) Dvorakova, K., Waltmire, C. N., Payne, C. M., Tome, M. E., Briehl, M. M., and Dorr, R. T. (2001) Induction of mitochondrial changes in myeloma cells by imexon. *Blood 97*, 3544–3551.
(28) Zorov, D. B., Filburn, C. R., Klotz, L.-O., Zweier, J. L., and Sollott, S. J. (2000) Reactive Oxygen Species (ROS)-induced ROS Release: A New Phenomenon Accompanying Induction of the Mitochondrial Permeability Transition in Cardiac Myocytes. *J. Exp. Med. 192*, 1001–1014.
(29) Halestrap, A. P., and Brenner, C. (2003) The Adenine Nucleotide Translocase: A Central Component of the Mitochondrial Permeability Transition Pore and Key Player in Cell Death. *Curr. Med. Chem. 10*, 1507–1525.
(30) Cox, A. G., Pullar, J. M., Hughes, G., Ledgerwood, E. C., and Hampton, M. B. (2008) Oxidation of mitochondrial peroxiredoxin 3 during the initiation of receptor-mediated apoptosis. *Free Radic. Biol. Med. 44*, 1001–1009.
(31) Meier, J. A., Hyun, M., Cantwell, M., Raza, A., Mertens, C., Raje, V., Sisler, J., Tracy, E., Torres-Odio, S., Gispert, S., Shaw, P. E., Baumann, H., Bandyopadhyay, D., Takabe, K., and Larner, A. C. (2017) Stress-induced dynamic regulation of mitochondrial STAT3 and its association with cyclophilin D reduce mitochondrial ROS production. *Sci. Signal. 10*, eaag2588.
(32) Sobotta, M. C., Liou, W., Stöcker, S., Talwar, D., Oehler, M., Ruppert, T., Scharf, A. N. D., and Dick, T. P. (2014) Peroxiredoxin-2 and STAT3 form a redox relay for H2O2 signaling. *Nat.*

*Chem. Biol. 11*, 64–70.
(33) Vyas, S., Zaganjor, E., and Haigis, M. C. (2016) Mitochondria and Cancer. *Cell 166*, 555–566.
(34) Galina, A. (2014) Mitochondria: 3-bromopyruvate vs. mitochondria? A small molecule that attacks tumors by targeting their bioenergetic diversity. *Int. J. Biochem. Cell Biol. 54*, 266–271.
(35) Smith, M. R., Vayalil, P. K., Zhou, F., Benavides, G. A., Beggs, R. R., Golzarian, H., Nijampatnam, B., Oliver, P. G., Smith, R. A. J., Murphy, M. P., Velu, S. E., and Landar, A. (2016) Mitochondrial thiol modification by a targeted electrophile inhibits metabolism in breast adenocarcinoma cells by inhibiting enzyme activity and protein levels. *Redox Biol. 8*, 136–148.
(36) Huang, B. K., Langford, T. F., and Sikes, H. D. (2016) Using Sensors and Generators of H2O2 to Elucidate the Toxicity Mechanism of Piperlongumine and Phenethyl Isothiocyanate. *Antioxid. Redox Signal. 24*, 924–938.

## 2.6 Appendix

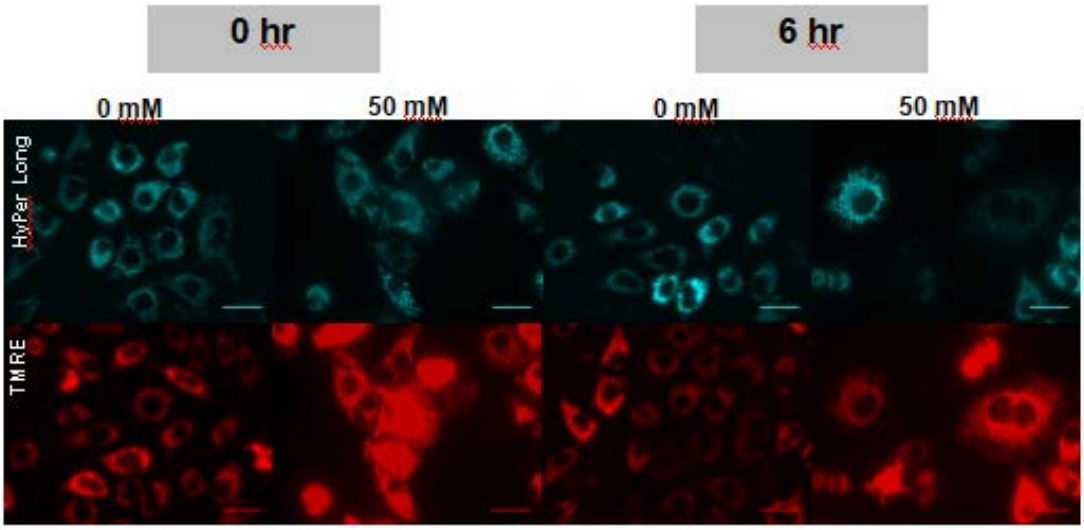


*Figure 2.6: Full microscopy images for Figure 2.1. Scale bars represent 50 µm.*

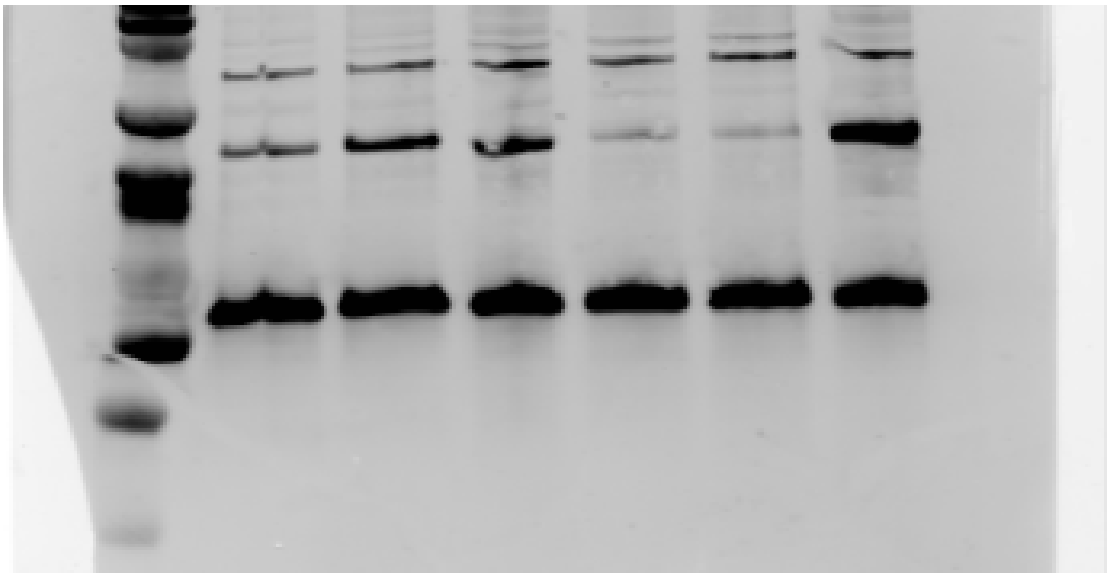

*Figure 2.7: Full redox Western blot image from Figure 2.2, depicting bands for Hsp60 (top), Prx-2 dimer (middle), and Prx-2 monomer (bottom).*

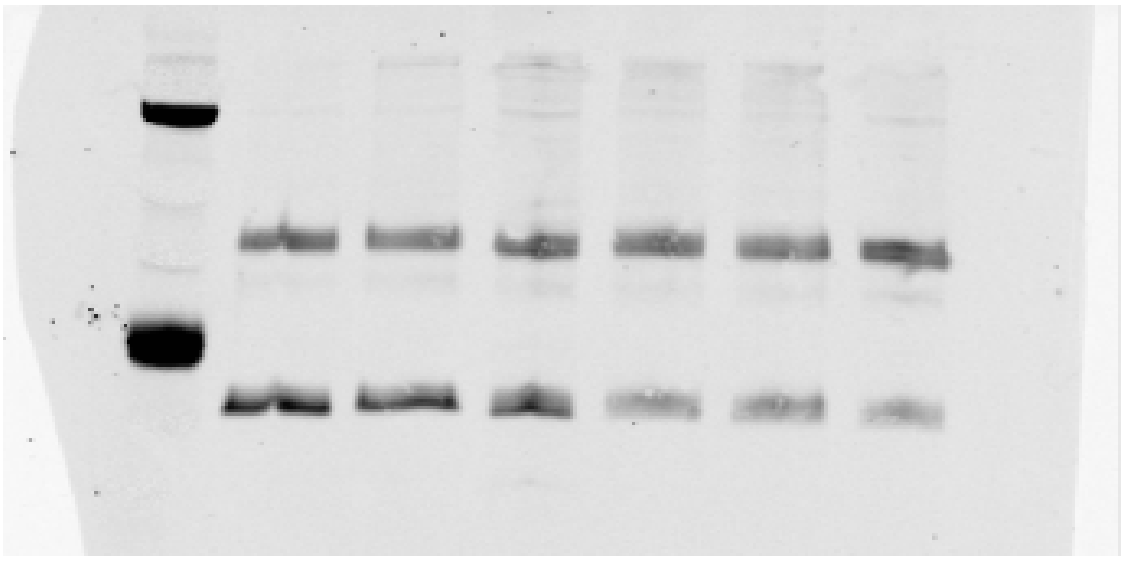

*Figure 2.8: Full redox Western blot image from Figure 2.2, depicting Prx-3 dimer (top) and Prx-3 monomer (bottom).*

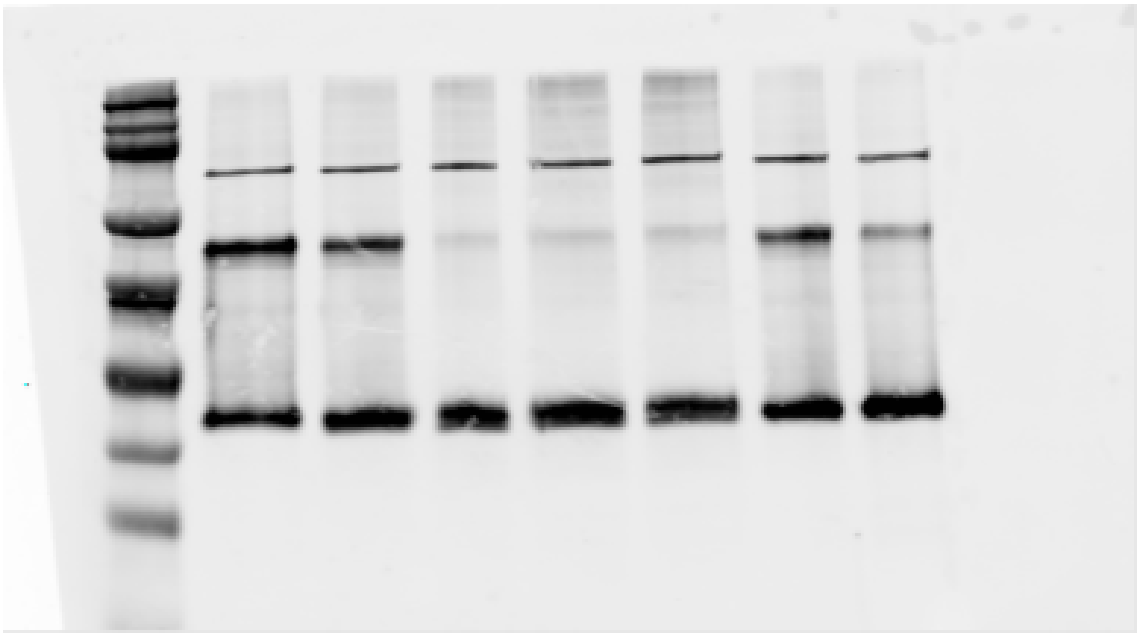

*Figure 2.9: Full hyperoxidation Western blot from Figure 2.2, depicting Hsp60 (top), Prx-2 dimer (middle), and Prx-2 monomer (bottom).*

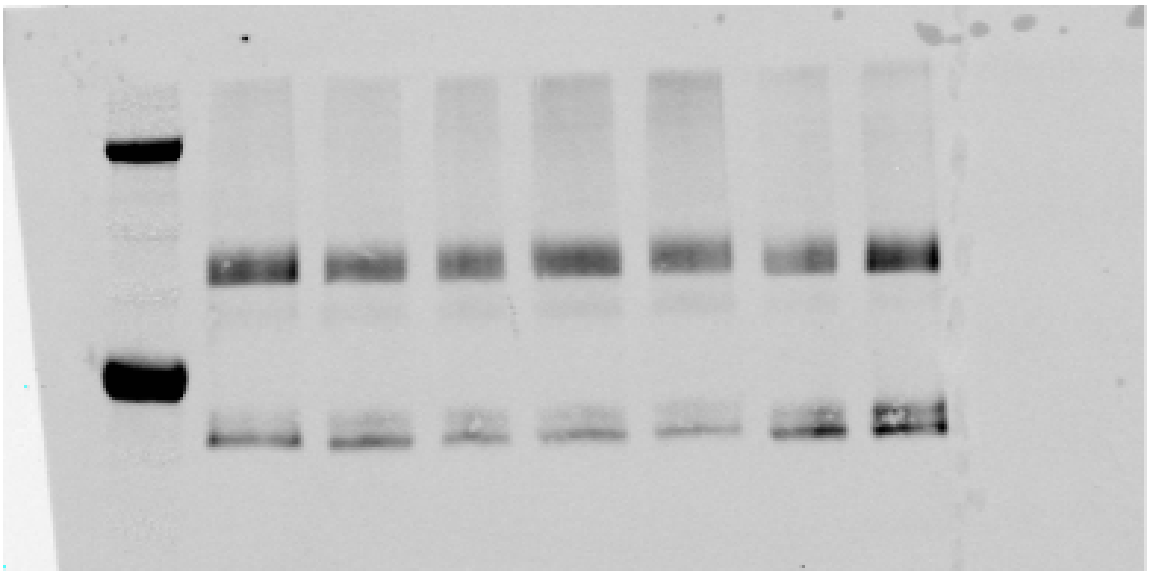

*Figure 2.10: Full hyperoxidation Western blot from Figure 2.2, depicting Prx-3 dimer (top) and Prx-3 monomer (bottom).*

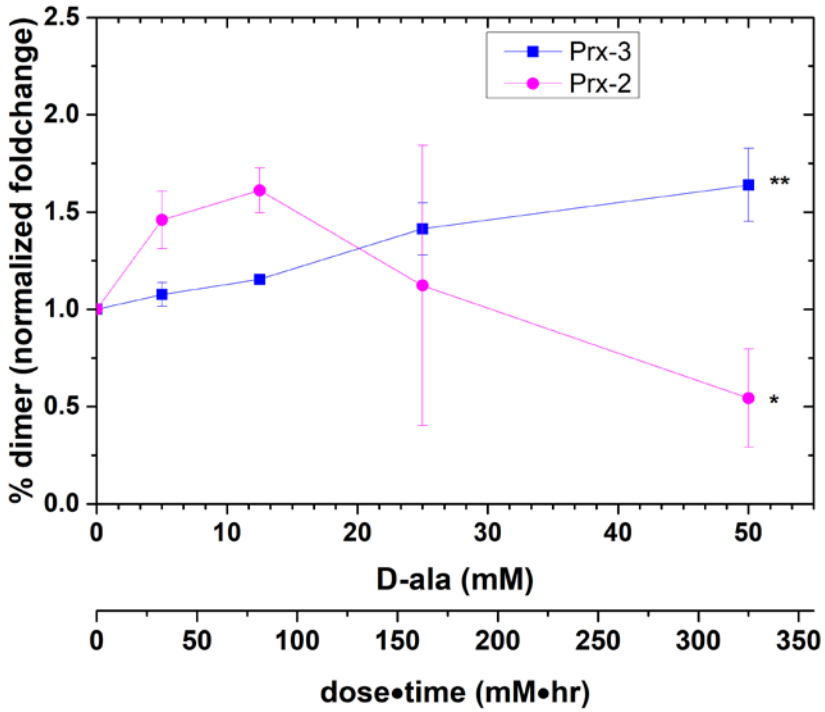


*Figure 2.11: Densitometry plot for redox Western blot depicted in Figure 2.2, normalized to the intensity of the loading control Hsp60. Points represent average of two independent experiments +/- SEM. ANOVA (Prx-3) or Welch's ANOVA (Prx-2) was performed to test the trends. * indicates P<0.1 and ** indicates P<0.05 for the series.*

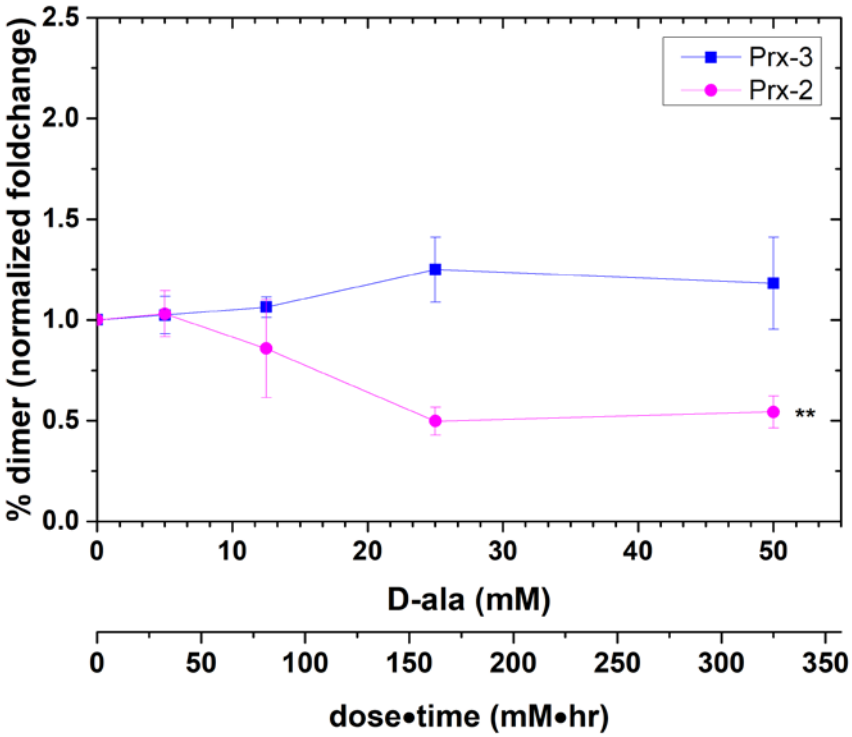


*Figure 2.12: Densitometry plots for hyperoxidation Western blots depicted in Figure 2.2, normalized to the intensity of the loading control Hsp60. Points represent the average of three independent experiments +/- SEM. Welch's ANOVA was performed to test the trends. ** indicates P<0.05 for the series. Prx-3 data demonstrated no statistically significant trend.*

*Table 2.1: Densitometry values from Figure 2.2, Figure 2.11, and Figure 2.12. All values were normalized to the loading controls in their respective blots.*

| **D-ala concentration (mM)** | | **Prx-3 monomer** | **Prx-3 dimer** | **Prx-2 monomer** | **Prx-2 dimer** | **Fraction Prx-3 dimer** | **Fraction Prx-2 dimer** |
|---|---|---|---|---|---|---|---|
| +MMTS | 0 | 62156+/-24228 | 35131+/-22608 | 134912+/-9702.6 | 28262+/-4399.5 | 0.2294+/-0.0762 | 0.1722+/-0.0121 |
| | 5 | 55002+/-13592 | 31645+/-15355 | 130478+/-7435.6 | 45359+/-12647 | 0.2426+/-0.0621 | 0.2530+/-0.0430 |
| | 12.5 | 42238+/-225.62 | 26941+/-10338 | 102437+/-12125 | 39072+/-4695.8 | 0.2654+/-0.0921 | 0.2761+/-$3.68x10^{-3}$ |
| | 25 | 33727+/-4749.1 | 32602+/-14685 | 113375+/-1449.2 | 28015+/-18809 | 0.3315+/-0.151 | 0.1846+/-0.110 |
| | 50 | 28036+/-3042.1 | 31959+/-11227 | 103398+/-2741.5 | 10358+/-4334.0 | 0.3659+/-0.0641 | 0.09053+/-0.0368 |
| -MMTS | 0 | 168343+/-70401 | 103304+/-16894 | 248726+/-63181 | 127650+/-13120 | 0.4195+/-0.106 | 0.3598+/-0.057 |
| | 5 | 141375+/-38840 | 93877+/-11540 | 247723+/-55652 | 137910+/-33708 | 0.4218+/-0.101 | 0.3583+/-0.0231 |
| | 12.5 | 176510+/-69196 | 113229+/-7843.4 | 317624+/-99019 | 149466+/-64090 | 0.4432+/-0.111 | 0.2840+/-0.0621 |
| | 25 | 134234+/-47757 | 120969+/-20753 | 268272+/-68041 | 55391+/-14079 | 0.5008+/-0.0936 | 0.1740+/-0.0214 |
| | 50 | 101386+/-32385 | 85484+/-22418 | 223757+/-53016 | 51760+/-12977 | 0.4654+/-0.0867 | 0.1891+/-0.0221 |

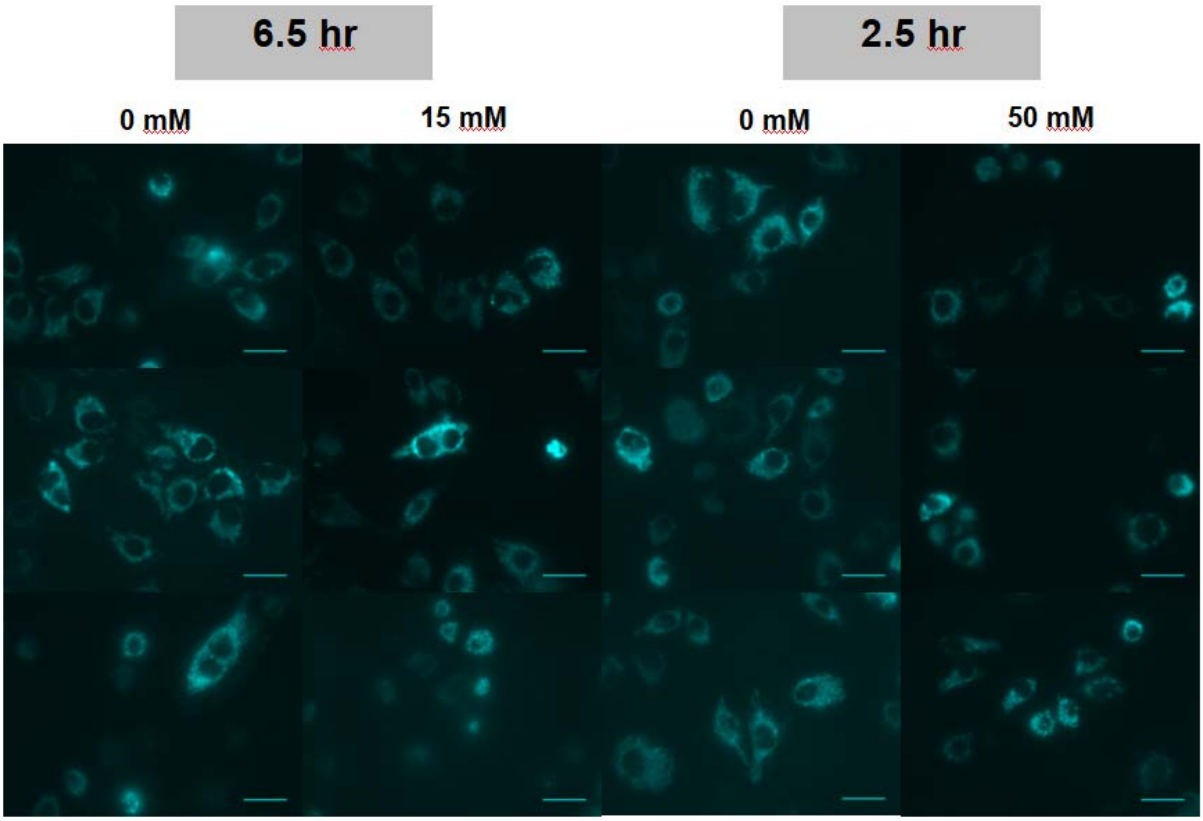


*Figure 2.13: Supporting microscopy image for Figure 2.4. Scale bars represent 50 µm.*

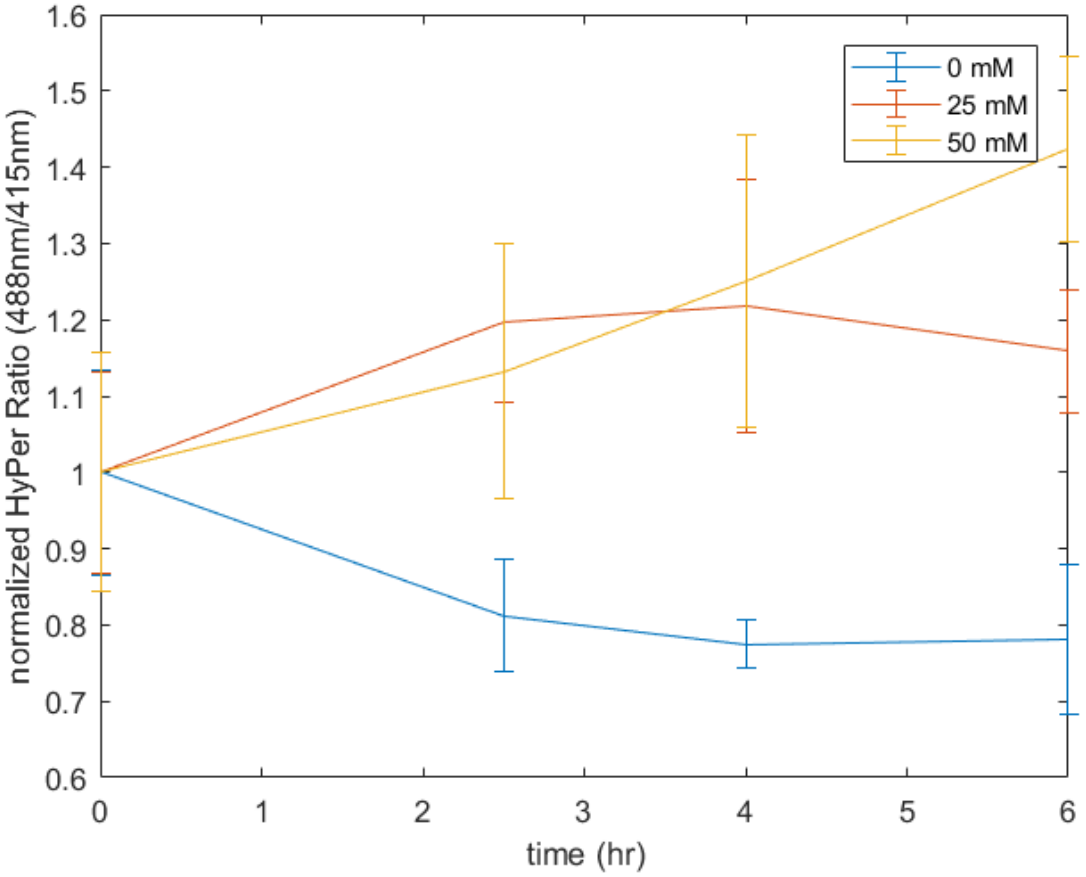


*Figure 2.14: Normalized HyPer ratios over time for three different D-alanine concentrations. Each point represents the mean +/- std of at least 15 cells. On average, the signal from HyPer-mito increases when cells expressing DAAO are stimulated with D-ala. A large degree of cell-to-cell heterogeneity of HyPer ratios was observed, as evidenced by the error bars.*

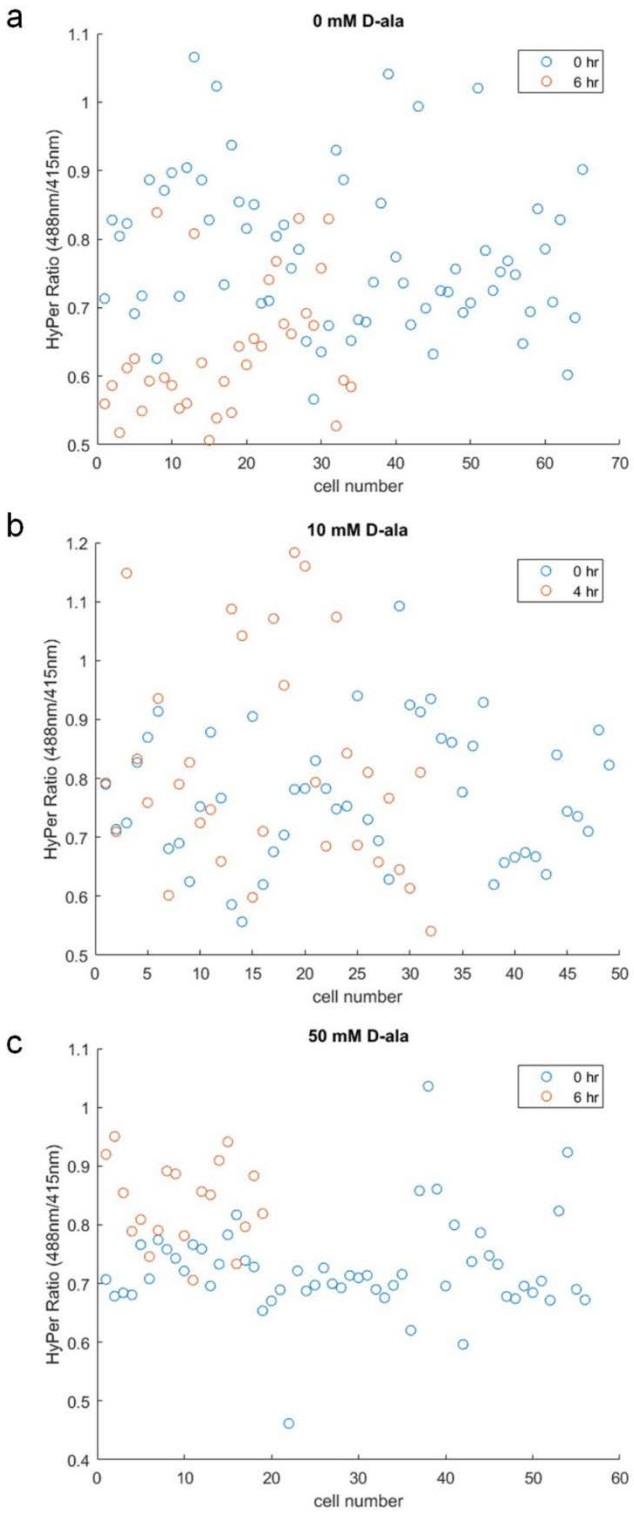


*Figure 2.15: HyPer ratio vs. cell number for three different D-alanine concentrations, showing the significant amount of scatter in the data even without $H_2O_2$ perturbation (a), as well as the change in the scatter of the ratios as the cells are perturbed with $H_2O_2$ (b and c).*

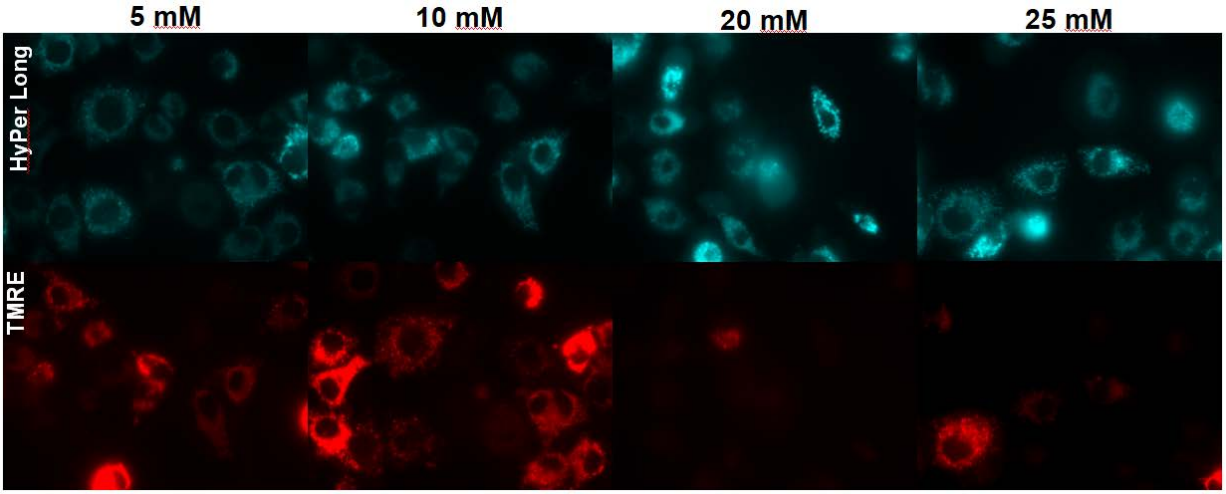


*Figure 2.16: Microscopy plots continued from Figure 2.5.*

### *2.6.1 : Quantification of HyPer ratios*

A rolling ball background subtraction method was applied to all images using a radius of 100 prior to quantification using ImageJ. Fluorescence intensities of individual cells were then measured in the HyPer Short (415 nm excitation) and HyPer Long (488 nm excitation). The ratio was taken as the HyPer Long intensity divided by the HyPer Short intensity. Ratios at each time point for each D-ala concentration were normalized to the average of the ratio at t=0.

### *2.6.2 : Sequence for DAAO-mito construct*

Mitochondrial localization sequence (MLS) underlined

ATGTTGAGCCGCGCAGTGTGCGGCACCAGCCGGCAGCTGGCTCCGGCTTTGGGGTAT
CTGGGCTCCAGGCAGGCTAGGATGCACTCGCAGAAGCGCGTCGTTGTCCTCGGATC
AGGCGTTATCGGTCTGAGCAGCGCCCTCATCCTCGCTCGGAAGGGCTACAGCGTGCA
TATTCTCGCGCGCGACTTGCCGGAGGACGTCTCGAGCCAGACTTTCGCTTCACCATG
GGCTGGCGCGAATTGGACGCCTTTCATGACGCTTACAGACGGTCCTCGACAAGCAA
AATGGGAAGAATCGACTTTCAAGAAGTGGGTCGAGTTGGTCCCGACGGGCCATGCC
ATGTGGCTCAAGGGGACGAGGCGGTTCGCGCAGAACGAAGACGGCTTGCTCGGGCA
CTGGTACAAGGACATCACGCCAAATTACCGCCCCCTCCCATCTTCCGAATGTCCACC
TGGCGCTATCGGCGTAACCTACGACACCCTCTCCGTCCACGCACCAAAGTACTGCCA
GTACCTTGCAAGAGAGCTGCAGAAGCTCGGCGCGACGTTTGAGAGACGGACCGTTA
CGTCGCTTGAGCAGGCGTTCGACGGTGCGGATTTGGTGGTCAACGCTACGGGACTTG
GCGCCAAGTCGATTGCGGGCATCGACGACCAAGCCGCCGAGCCAATCCGCGGCCAA
ACCGTCCTCGTCAAGTCCCCATGCAAGCGATGCACGATGGACTCGTCCGACCCCGCT
TCTCCCGCCTACATCATTCCCCGACCAGGTGGCGAAGTCATCTGCGGCGGGACGTAC
GGCGTGGGAGACTGGGACTTGTCTGTCAACCCAGAGACGGTCCAGCGGATCCTCAA
GCACTGCTTGCGCCTCGACCCGACCATCTCGAGCGACGGAACGATCGAAGGCATCG

AGGTCCTCCGCCACAACGTCGGCTTGCGACCTGCACGACGAGGCGGACCCCGCGTC
GAGGCAGAACGGATCGTCCTGCCTCTCGACCGGACAAAGTCGCCCCTCTCGCTCGGC
AGGGGCAGCGCACGAGCGGCGAAGGAGAAGGAGGTCACGCTTGTGCATGCGTATG
GCTTCTCGAGTGCGGGATACCAGCAGAGTTGGGGCGCGGCGGAGGATGTCGCGCAG
CTCGTCGACGAGGCGTTCCAGCGGGACCACGGCGCGGCGCGGGAGTAG

# **Chapter 3 :** Kinetic modeling of $H_2O_2$ dynamics in human epithelial mitochondria

Hydrogen peroxide ($H_2O_2$) promotes a range of phenotypes depending on its intracellular concentration and dosing kinetics, including cell death. While this qualitative relationship has been well established, the quantitative mechanisms of $H_2O_2$ signaling are still being elucidated. Mitochondria, a putative source of intracellular $H_2O_2$, have recently been demonstrated to be particularly vulnerable to localized $H_2O_2$ perturbations, eliciting a dramatic cell death response in comparison to similar cytosolic perturbations. We sought to improve our dynamic and mechanistic understanding of the mitochondrial $H_2O_2$ reaction network in HeLa cells by creating a kinetic model of this system. This model uses the most current quantitative proteomics and kinetic data available to model species abundances and rate constants, respectively. This model also considers responses on different time scales. We predict that basal mitochondrial $H_2O_2$ will be in the low nM range (~3 nM) and will be inversely dependent on the total pool of peroxiredoxin-3 (Prx3). We additionally expect the mitochondrial reaction network to control perturbations well, up to $H_2O_2$ generation rates ~50 μM/s (0.25 nmol/mg-protein/s), above which point the (Prx3) system collapses. We found Prx3 to control the observed $H_2O_2$ dynamics. Experimental validation of these results demonstrated good trend agreement at short times (≤ 15 min) but at longer times suggested a greater impact of transport of $H_2O_2$ out of the mitochondria and into the cytosol, as evidenced by peroxiredoxin-2 (Prx2) oxidation. These results have applications for understanding the physiologically relevant concentration ranges of $H_2O_2$ in mammalian epithelial cells, as well as which thiol modifications are possible under these conditions via direct, bimolecular reaction mechanisms.

## 3.1 Introduction

Reactive oxygen species (ROS) are a class of chemical species that promote diverse phenotypes depending on intracellular concentration and cumulative dose over time, spanning the gamut from homeostasis to toxicity [1,2]. Among ROS, the behavior of hydrogen peroxide ($H_2O_2$) most closely resembles that of a classical signaling molecule, based on the specificity of its reactions and its *in vivo* half-life [3–6]. Mitochondria are putatively a main intracellular source of $H_2O_2$ under basal conditions as a result of the electron transport chain (ETC) and oxidative phosphorylation (OxPhos) [2,7]. This organelle is also hypothesized to be an important site for $H_2O_2$-mediated signaling [8,9].

Previous work in our group has demonstrated that $H_2O_2$ perturbations directed to the mitochondrial matrix elicit a marked toxicity in HeLa cells, especially when contrasted against comparable perturbations delivered in the cytoplasm [10,11]. This toxicity was both concentration- and time-dependent, indicating the importance of a dynamic understanding of the $H_2O_2$ reaction network. Building upon our experimental results, we sought to further our mechanistic understanding of mitochondrial $H_2O_2$ kinetics by constructing a computational model of the reaction network. Detailed molecular mechanisms that connect changes in $H_2O_2$ with phenotypic responses such as changes in mitochondrial morphology, mitochondrial permeability transition (MPT), and programmed cell death have not been elucidated. Since these signaling responses occur during excursions in $H_2O_2$ concentration from the basal steady state, we expect that establishing a quantitative range that can be connected with phenotypic responses will help inform whether particular cysteine residues are likely to become directly oxidized [12]. Existing models on mitochondrial ROS so far have largely fallen into two categories: detailed kinetic models focusing on fast-respiring cells, like cardiac cells [13,14], or models that exclude the thioredoxin/peroxiredoxin (Trx/Prx) system [15]. While models of cardiac mitochondrial $H_2O_2$ reaction networks are well-

validated in their experimental systems, we do not expect them to generalize to epithelial cells, as their rates of cellular respiration are much faster [16], and it has additionally been demonstrated that the abundance of mitochondrial proteins can vary greatly between tissues and cell types [17]. The Prxs are so abundant and react with $H_2O_2$ with such a high second-order rate constant ($10^6$-$10^8$ $M^{-1}s^{-1}$) that this antioxidant system cannot be neglected [18,19]. Some additional modeling efforts have focused on the kinetics of species other than $H_2O_2$ specifically [20] or on parameter estimation [21]. To our knowledge, this model represents the first kinetic model of the mitochondrial $H_2O_2$ reaction network in epithelial cells, incorporating the most recent quantitative data specific for HeLa cells.

Here, we implement this new model to predict basal $H_2O_2$ concentrations in HeLa cell mitochondria. We also predict network behavior in response to sustained $H_2O_2$ perturbations, including the degree of oxidation of four major antioxidant species present in epithelial mitochondria: Prx3, glutathione peroxidase 1 (Gpx1), Prx5, and Gpx4. This system was modeled by mass action kinetics using a system of 28 reactions, 29 parameters, and 28 species in MATLAB. Basal mitochondrial $H_2O_2$ as well as reaction network response to $H_2O_2$ perturbations were predicted. Modeling was validated experimentally by redox Western blots of the Prxs using the mitochondrially-localized $H_2O_2$ generator D-amino acid oxidase (mito-DAAO). HeLa cells were exposed to a range of D-alanine concentrations, a substrate for mito-DAAO, over time, and Western blots were performed on the cell lysates to observe the change in Prx3 and Prx2 oxidation with the different treatments.

## 3.2 Methods

*3.2.1 : Model Formulation: Baseline Model*

This model was adapted from our previously published kinetic model of the cytoplasmic antioxidant network, and consists of a system of first-order ordinary differential equations of the form

$$\frac{dC_i}{dt} = R_i \tag{0.1}$$

where $C_i$ is the species concentration, $t$ is time and $R_i$ is the net reaction for that species [22]. It assumes species concentrations are homogeneous throughout the compartment. The baseline model investigates the steady state conditions in the mitochondria, where the only source of endogenous $H_2O_2$ is assumed to be from the ETC due to cellular respiration. For the purposes of this simulation, the rate of $H_2O_2$ generation due to OxPhos is assumed to be invariant. As a first approximation, no transport of $H_2O_2$ between the mitochondria and the cytoplasm is assumed. This system quickly reaches steady state (less than 1 s), so baseline simulations are carried out to 5 s. The stiff equation solver ode15s in MATLAB was implemented to solve the system of equations.

The main reaction systems that this model captures are the thioredoxin/peroxiredoxin/thioredoxin reductase (Trx/Prx/TR) and the glutathione/glutathione peroxidase/glutaredoxin (GSH/Gpx/Grx) networks. The Prx isoforms found in the mitochondria are Prx3 and Prx5 [23,24], which are reduced by Trx2 [25,26]. Trx2 also reduces disulfide bonds to protein dithiols [27]. Both Gpx1 and Gpx4 are found in the mitochondria, though at low concentrations in epithelial cells [28]. Grx2 is the most abundant mitochondrial Grx isoform, and is responsible for reducing S-glutathionylated proteins [29–31]. While the prior proteins are all considered mitochondrially localized, both GSH and sulfiredoxin (Srx) are generally considered cytoplasmic molecules that must be imported into the mitochondria [17,32–34]. The mitochondria maintains a large pool of the former, but the latter is only imported based upon a stimulus [33,34]. Catalase is not included because it is not expected to be found in the mitochondria for most cell types, including HeLa cells [17,28,35]. A schematic representation of the reaction networks captured by this model is shown in Figure 3.1.

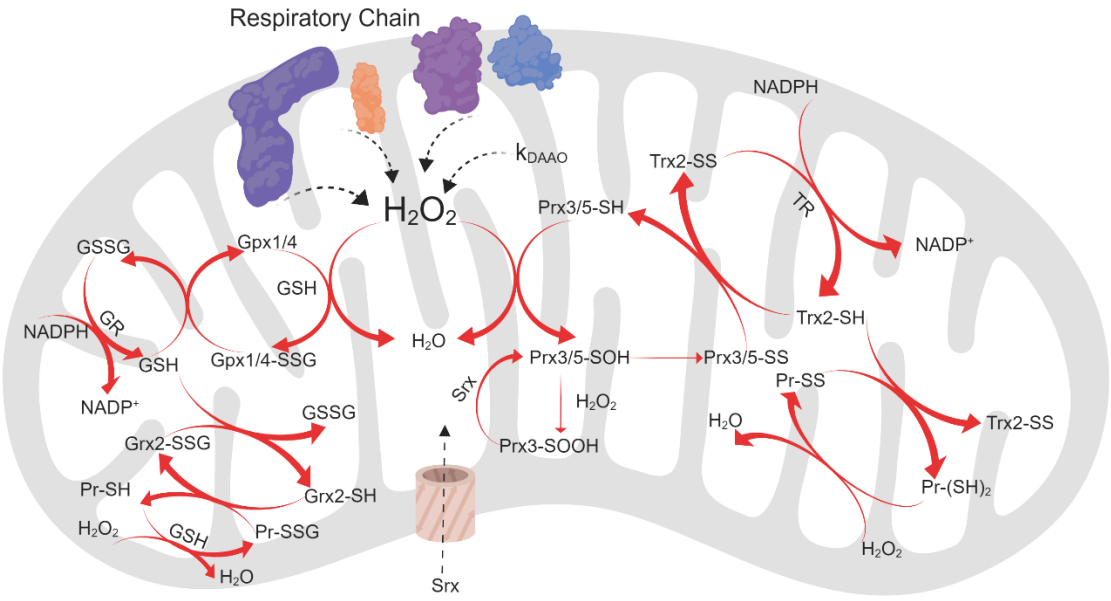


*Figure 3.17: Schematic representation of the $H_2O_2$ reaction network in the mitochondria. $H_2O_2$ is evolved as a result of cellular respiration and the respiratory complexes at a rate that is taken as fixed for the purposes of this model. For the perturbation model only, $H_2O_2$ is also added to the system by a variable source term, $k_{DAAO}$. It can then participate in reactions with the two Prx isoforms present in the mitochondria (Prx3 and Prx5), which are reduced by Trx2. $H_2O_2$ can also react with one of the Gpx isoforms in the mitochondria (Gpx1 and Gpx4), which involves reduction by GSH. Both of these networks require NADPH for reduction [36,37]. Only Prx3 can undergo the hyperoxidation pathway, forming a sulfinic acid, which is reduced by Srx. Srx is imported into the mitochondria. Finally, $H_2O_2$ can react with protein thiols and dithiols, which are reduced by Trx2 and Grx2, respectively. Image created with Biorender.com.*

The reaction rate parameters for mass action or Michaelis-Menten kinetics in Eq.(3.1) were found in the peer-reviewed literature or derived from published data. Details on calculations used for derivations can be found in Supporting Information. For any cases where mitochondria-specific values could not be located, the cytosolic equivalent was assumed. These parameters are summarized in Table 3.1. One major difference between previously published models and this one is the treatment of Srx. Previous work has assumed zeroth-order kinetics with respect to Srx, and the form of the rate law for hyperoxidized Prx3 has been:

$$\frac{d\left[Prx3-SOOH\right]}{dt} = k_{hyperox}\left[Prx3-SOH\right]\left[H_2O_2\right] - k_{cat}\left[Prx3-SOOH\right] \qquad (0.2)$$

where $k_{hyperox}$ is the rate of hyperoxidation of Prx3 and $k_{cat}$ is the turnover number reported for Srx

by Chang and colleagues [38]. However, overexpression studies have clearly demonstrated an increase in reduction rate of the sulfinic acid with increased Srx concentration [39]. The form of the rate law proposed by Eq. (3.2) fails to capture any dependence on Srx, so we propose a rate law with first-order dependence on Srx as a first approximation.

$$\frac{d\left[Prx3-SOOH\right]}{dt} = k_{hyperox}\left[Prx3-SOH\right]\left[H_2O_2\right] - k'\ \left[Prx3-SOOH\right]\left[Srx\right] \qquad (0.3)$$

where $k'$ is the estimated second-order rate constant. These parameters, $k_{hyperox}$ and $k'$ correspond to $k_7$ and $k_8$ in Table 3.1, respectively.

*Table 3.2: Kinetic parameters. Calculations for parameters that were derived can be found in the Appendix.*

| **Reaction** | **Parameter** |
|---|---|
| Generation of $H_2O_2$ by OxPhos | $k_1 = 4$ µM/s [16,40] |
| $k_2$[Gpx1red][$H_2O_2$] | $k_2 = 60$ µM$^{-1}$s$^{-1}$ [35,41] |
| $k_3$[Gpx1ox][GSH] | $k_3 = 0.04$ µM$^{-1}$s$^{-1}$ [42] |
| $k_4$[Gpx-SSG][GSH] | $k_4 = 10$ µM$^{-1}$s$^{-1}$ [42] |
| $k_{20}$[$NADP^+$]/($k_5$+[$NADP^+$]) | $k_5 = 57$ µM [43] |
| $k_6$[Prx3-SH][$H_2O_2$] | $k_6 = 20$ µM$^{-1}$s$^{-1}$ [23] |
| $k_7$[Prx3-SOH][$H_2O_2$] | $k_7 = 0.014$ µM$^{-1}$s$^{-1}$ [44] |
| $k_8$[Prx3-SOOH][Srx] | $k_8 = 3x10^{-3}$ µM$^{-1}$s$^{-1}$ [38] |
| $k_9$[Prx3-SOH] | $k_9 = 20$ s$^{-1}$ [44] |
| $k_{10}$[Prx3-SS][Trx2-SH] | $k_{10} = 0.22$ µM$^{-1}$s$^{-1}$ [26,45] |
| $k_{11}$[GSH] | $k_{11} = 7.4x10^{-5}$ s$^{-1}$ [46] |
| $k_{12}$[Pr-SH][$H_2O_2$] | $k_{12} = 1x10^{-4}$ µM$^{-1}$s$^{-1}$ [47,48] |
| $k_{13}$[Pr-SOH][GSH] | $k_{13} = 0.12$ µM$^{-1}$s$^{-1}$ [49,50] |
| $k_{14}$[Grx2-SH][Pr-SSG] | $k_{14} = 0.01$ µM$^{-1}$s$^{-1}$ [51] |
| $k_{15}$[Grx2-SSG][GSH] | $k_{15} = 0.04$ µM$^{-1}$s$^{-1}$ [52] |
| $k_{16}$[Pr-$(SH)_2$][$H_2O_2$] | $k_{16} = 1x10^{-4}$ µM$^{-1}$s$^{-1}$ [47] |
| $k_{17}$[Pr-SS][Trx2-SH] | $k_{17} = 1x10^{-4}$ µM$^{-1}$s$^{-1}$ [47] |
| $k_{18}$[GSSG][NADPH] | $k_{18} = 3.2$ µM$^{-1}$s$^{-1}$ [53] |
| $k_{19}$[Trx2-SS][NADPH] | $k_{19} = 20$ µM$^{-1}$s$^{-1}$ [54] |
| $k_{20}$[$NADP^+$]/($k_5$+[$NADP^+$]) | $k_{20} = 375$ µM/s [43] |
| GSH synthesis | $k_{21} = 0.41$ µM/s [55] |
| Trx2 synthesis | $k_{22} = 6.97x10^{-4}$ µM/s [56] |
| $k_{23}$[Prx5-SH][$H_2O_2$] | $k_{23} = 0.3$ µM$^{-1}$s$^{-1}$ [23,25] |
| $k_{24}$[Prx5-SOH] | $k_{24} = 14.7$ s$^{-1}$ [25] |
| $k_{25}$[Prx5-SS][Trx2-SH] | $k_{25} = 2$ µM$^{-1}$s$^{-1}$ [25] |
| $k_{26}$[Gpx4red][$H_2O_2$] | $k_{26} = 0.05$ µM$^{-1}$s$^{-1}$ [57] |
| $k_{27}$[Gpx4ox][GSH] | $k_{27} = 0.02$ µM$^{-1}$s$^{-1}$ [57] |
| Srx import | $k_{29} = 1.23x10^{-5}$ µM/s [58] |

Species abundances for model initialization were also either found in literature, calculated from published datasets, or calculated based on molar balances and rate laws. Species that were found in literature/published datasets are summarized in Table 3.2 and species that were calculated are summarized in Table 3.3. Gpx1 and Gpx4 were found to be at a much lower abundance than previously reported (2 and 1 order of magnitude lower, respectively) [59]. Prx3-SH abundance is given as a range rather than a single value. This is the result of the assumptions necessary to convert the proteomics dataset in [28] to a concentration, and represents potential cell-to-cell variability. For these calculations, mitochondrial volume was taken as 0.29 $\mu m^3$ [60] and mitochondrial number in a HeLa cell has been reported to range from 383 – 882 [61]. A total protein density throughout the cell was reported as $2x10^5$ mg/L in [28] so we assumed this density was invariant between organelles. Additional details regarding these calculations can be found in the Appendix. While all the proteins that were calculated based on the data in [28] produced a range of possible values, Prx3-SH was by far the most abundant and/or had the potential to vary most from what was reported previously in literature. Therefore, in all but this instance, we took the median value calculated or kept the literature value if these were very close. Because several species are initialized by molar balance, the range in Prx3-SH initialization results in several species in Table 3.3 to initialize differently depending on its concentration.

*Table 3.3: Initial species abundances*

| Species | Concentration (µM) |
|---|---|
| Prx3-SH | 48 – 110 [28,60,61] |
| Prx5-SH | 14 [28,60,61] |
| Gpx1 | $1.5x10^{-2}$ [17,28,60,61] |
| Gpx4 | 0.23 [17,28,60,61] |
| Grx2 | 1 [28,60,61] |
| Trx2-SH | 7.7 [28,60–63] |
| Trx2-SS | 0.075 [64] |
| GSH | $5x10^{3}$ [23] |
| GSSG | 1.78 [64] |
| NADPH | 30 [65] |
| $NADP^+$ | 0.03 [66] |
| Pr-SH | $1x10^{-3}$ [47] |
| Pr-$(SH)_2$ | $1.09x10^{3}$ [64] |
| Srx | $8.8x10^{-3}$ [28] |

*Table 3.4: Derived initial species abundances*

| Species | Concentration (µM) |
|---|---|
| $H_2O_2$ | $2x10^{-3}$ – $4x10^{-3}$ |
| Prx3-SOH | 0.18 – 0.20 |
| Prx3-SS | 2.2 – 2.3 |
| Prx3-SOOH | 0.19 – 0.42 |
| Prx5-SOH | $5x10^{-4}$ – $1x10^{-3}$ |
| Prx5-SS | $5x10^{-4}$ – $1x10^{-3}$ |
| Gpx1ox | $8x10^{-6}$ – $2x10^{-5}$ |
| Gpx1-SSG | $3x10^{-8}$ – $7x10^{-8}$ |
| Gpx4ox | 0 |
| Gpx4-SSG | 0 |
| Grx2-SSG | $1x10^{-16}$ |
| Pr-SOH | $3x10^{-13}$ – $6x10^{-13}$ |
| Pr-SSG | $1x10^{-8}$ – $3x10^{-8}$ |
| Pr-SS | 0.26 – 0.59 |

### *3.2.2 : Model Formulation: $H_2O_2$ Perturbation*

The second part of this modeling endeavor sought to investigate the effects of a source of $H_2O_2$ perturbation, similar to what is introduced by the synthetic biology tool D-amino acid oxidase (DAAO) targeted to the mitochondrial matrix. This was modeled as a constant source

term, $k_{DAAO}$, within the $H_2O_2$ rate equation, as depicted in Figure 3.1. Because we were interested in how the network would respond to perturbations of varying magnitudes, we swept this parameter across a range of values until we reached an upper limit of physiological relevance, which we defined as the complete collapse of the Prx3 system. This part of the simulation was carried out to 3600 s (1 hr).

*3.2.3 : Sensitivity Analysis*

In order to calculate the sensitivity of $H_2O_2$ concentration and Prx3-SS concentration to the model parameters, the finite difference approximation method was used [67]. The sensitivities were calculated using the following equation:

$$s_i(t) = \frac{\partial C_j(t)}{\partial k_i} = \frac{C_j(k_i + \Delta k_i, t) - C_j(k_i, t)}{\Delta k_i} \tag{0.4}$$

Where $s_i$ is the sensitivity corresponding to parameter $k_i$ and $C_j$ is the concentration of the either $H_2O_2$ or Prx3-SS. Parameters were perturbed by 10% to reflect an estimate of typical experimental error, and sensitivities were normalized to adjust for differences in orders of magnitude:

$$\overline{s_i}(t) = \frac{\partial C_j(t) / C_j(t)}{\partial k_i / k_i} \tag{0.5}$$

Here, we report only $\overline{s_i}$. All sensitivities were calculated at the end of the perturbation analysis for all values of $k_{DAAO}$.

*3.2.4 : Model Validation*

**Cell Culture**

HeLa cells (a generous gift from Dane Wittrup) that had previously been transfected by lentivirus to stably express a mitochondrially-targeted D-amino acid oxidase (mito-DAAO) $H_2O_2$ generator [10] were maintained in Dulbecco's modified Eagle's medium (DMEM; Lonza)

supplemented `with 10% fetal bovine serum (FBS; ATCC) at 37 °C in a humidified atmosphere with 5% $CO_2$. Cells were passaged approximately every 3 days and were maintained under selective pressure using 6 μg/mL puromycin (Sigma) until 24 hrs before any experiments.

**Analysis of Prx Response to Mitochondrial $H_2O_2$ Perturbations**:

HeLa cells expressing mito-DAAO were seeded at $3.5x10^5$ cells/well in 6-well plates ~18 hours prior to the start of generation (target confluence ~50% at start of experiment). Cells were exposed to 5 μM flavin adenine dinucleotide (FAD; Sigma) and concentrations of D-alanine (Sigma) from 0 – 25 mM in Roswell Park Memorial Institute 1640 medium (RPMI; Invitrogen) without phenol red. At the end of the $H_2O_2$ generation period, cells were washed with ice cold 1x phosphate buffered saline (PBS) and then incubated on ice with 2 mL 100 mM methyl methanethiosulfonate (MMTS; Sigma) for 30 min to block free thiols. Cells were washed twice more with cold PBS, then lysed in 100 μL of lysis buffer (0.5% Triton X-100 (Sigma), 1x HALT protease and phosphatase inhibitor (ThermoFisher), 1x PBS). Lysates were centrifuged on a cooled rotor for 10 min at 10,000xg and the supernatant was collected and stored at -80 °C for further analysis. Western blotting was carried out according to the protocol in [68]. Proteins were separated by non-reducing SDS-PAGE using a pre-cast 12% polyacrylamide stain-free gel (Bio-Rad). Following SDS-PAGE, the gel was activated for 45 s using a ChemiDoc MP (Bio-Rad), then proteins were transferred to a polyvinylidene difluoride (PVDF) membrane for immunoblotting. Blots were blocked using Odyssey blocking buffer (Licor), and incubated with primary antibodies against Prx3 (Abcam, ab73349), Prx2 (R&D Systems, AF3489), and Hsp60 (R&D Systems, Clone# 264233) either overnight at 4 °C or 2 hr at room temperature. Blots were incubated for 1 hr at room temperature with Licor IRDye secondary antibodies. The ChemiDoc MP system was used to image the blots, then ImageJ was used to quantify the images for densitometry.

**Statistical Analysis**

Analysis of variance (ANOVA) was used to test for trends in the fractional oxidation of the Prx protein, as measured by Western blot. At least three biological replicates per time point were used for trend testing. Post-hoc Tukey's Honest Significant Difference (Tukey-HSD) testing was performed to determine which sample means were different from the control (0 mM D-ala) within each time point.

## 3.3 Results

The first quantity investigated was the baseline concentration of $H_2O_2$ in the mitochondria. This steady-state concentration showed a strong inverse dependence on the available pool of Prx3, as shown in Figure 3.2a. Basal mitochondrial $H_2O_2$ concentration was predicted to range between 1.8 – 4.2 nM, higher than the basal concentration of 80 pM predicted for the cytoplasm, a necessary condition for mitochondria-to-cytoplasm transport [22]. We also investigated the effect of the total available pool of Prx3 on the relative basal oxidation levels, calculated as

$$\text{fraction oxidized} = \frac{Prx3 - SS}{Prx3_{total}} \tag{0.6}$$

This quantity is one often measured experimentally by Western blotting, and at baseline can characterize the variability between different cell types [10,69]. Similar to the basal $H_2O_2$ concentration, the fraction of oxidized Prx3 demonstrates an inverse relationship with the total pool of Prx3, as depicted in Figure 3.2b. Finally, for subsequent questions, we fixed the Prx3 concentration; prior literature has reported Prx3 concentrations at ~60 μM, so we examined the 62 μM condition [35]. Figure 3.2c demonstrates the basal concentrations of the oxidized and reduced isoforms of the four major antioxidant species with the 62 μM total Prx3 pool. Only Prx3 experienced any major oxidation at baseline, as summarized in Table 3.4.

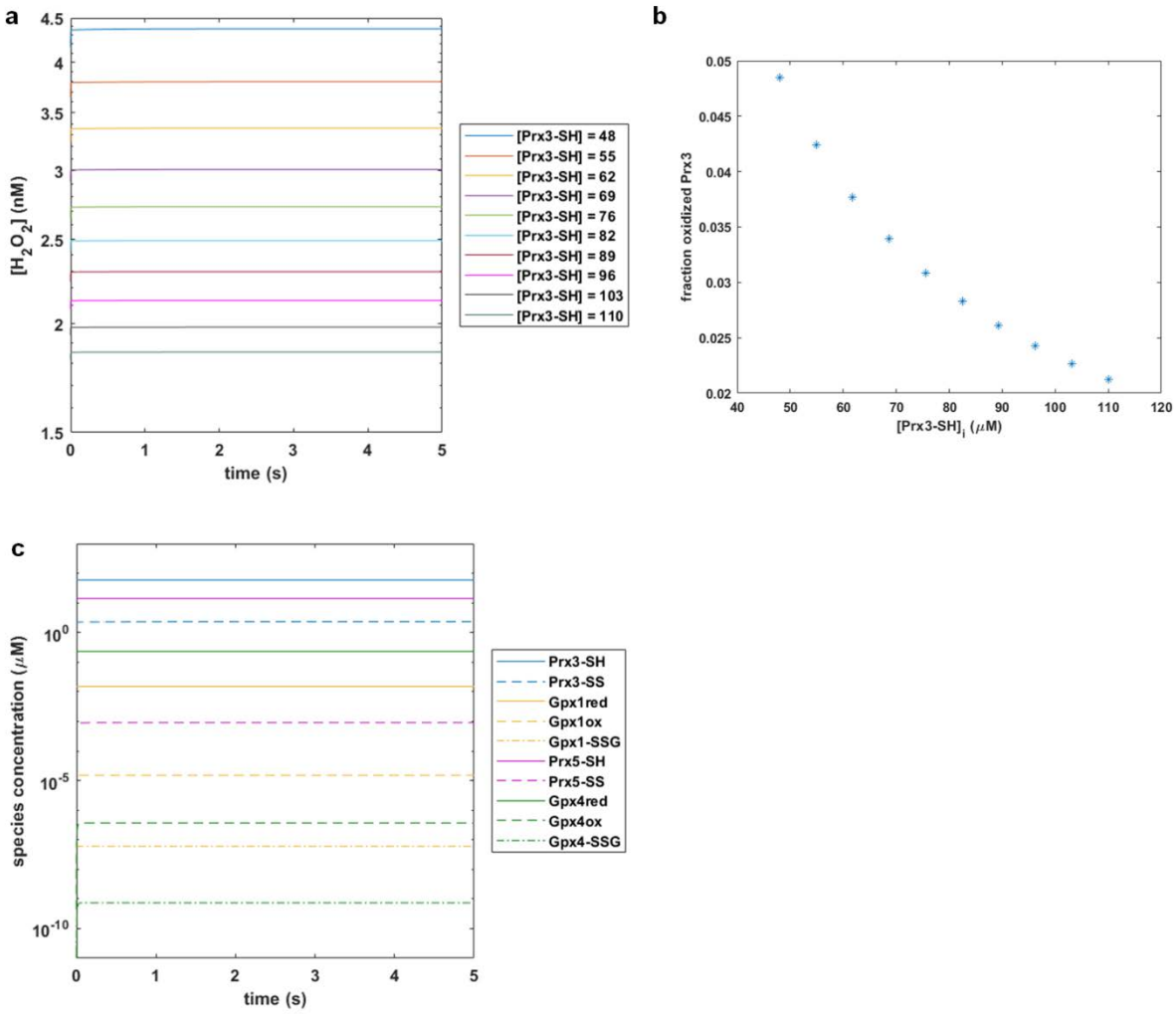


*Figure 3.18: Baseline Conditions.Steady state [$H_2O_2$] in the mitochondria with fixed $H_2O_2$ generation from OxPhos (4 µM/s) for different initial concentrations of Prx3-SH. Range of Prx3-SH based on possible range calculated from [28]. b) Fraction of oxidized Prx3 (Prx3-SS/total Prx3) vs. initial concentration of Prx3-SH for fixed $H_2O_2$ generation from OxPhos (4 µM/s). c) Steady state concentrations of oxidized and reduced isoforms for the four major antioxidants in the mitochondria for fixed initial pool of Prx3-SH (62 µM) and fixed $H_2O_2$ generation from OxPhos (4 µM/s). Similar plots for a fixed $H_2O_2$ generation rate from OxPhos of 11 µM/s can be found in Appendix Figure 3.6-3.8.*

*Table 3.5: Summary of fractional oxidation of major antioxidants in the network*

| **Species** | **Fraction oxidized** |
|---|---|
| Prx3 | 0.037 |
| Gpx1 | $1.0 \times 10^{-3}$ |
| Prx5 | $6.5 \times 10^{-5}$ |
| Gpx4 | $1.6 \times 10^{-6}$ |

Once the baseline was established, we next sought to evaluate the network response to $H_2O_2$ perturbations. The magnitude of the perturbation term, $k_{DAAO}$, was varied up to 70 µM/s, at which point the reaction network showed evidence of nearing saturation, demonstrated in Figure 3.3 by changes in the shape of the $H_2O_2$ traces at high perturbation rates. Figure 3.3a depicts the concentration of $H_2O_2$ over time for each perturbation rate simulated. For all but the highest values of $k_{DAAO}$, the $H_2O_2$ concentration settled out to a new steady state. It can be observed from the plots of Prx3 dynamics in Figure 3.3b – d that this antioxidant pool controls the dynamics of mitochondrial $H_2O_2$. Prx3-SH concentration reached a new steady state for each perturbation rate, reflecting the predicted $H_2O_2$ behavior. Prx3-SS concentrations jumped to correspondingly higher levels for each perturbation rate, and slowly declined over the 1 hr simulation, accompanied by a slow increase in the Prx3-SOOH isoform. At perturbations above 54 µM/s, the $H_2O_2$ concentration followed a sigmoid trend that reached an asymptote in the mid-micromolar range. This was accompanied by a collapse of the Prx3 network, demonstrated by Figure 3.3b – c. At these very high perturbations, all of the Prx3 became trapped as the hyperoxidized isoform, seen in Figure 3.3d. It is unlikely that a physiologically relevant perturbation would cause a total collapse of the Prx3 network, so we concluded that the top of our $k_{DAAO}$ range is an excessive and unrealistic limit. It is only when the capacity of the Prx3/Trx/TR system was exceeded that other antioxidants were able to kinetically compete and react with $H_2O_2$, as summarized by Table 3.5, which lists the fractional oxidation for the four major antioxidant species at each perturbation rate. It is important to note that the observed steady states that result from this $H_2O_2$ perturbation analysis are the net effect of the rate of $H_2O_2$ generation by OxPhos and the additional $k_{DAAO}$ generation term; a higher OxPhos generation rate would result in a lower $k_{DAAO}$ that causes non-physiological behavior in the reaction network (Appendix).

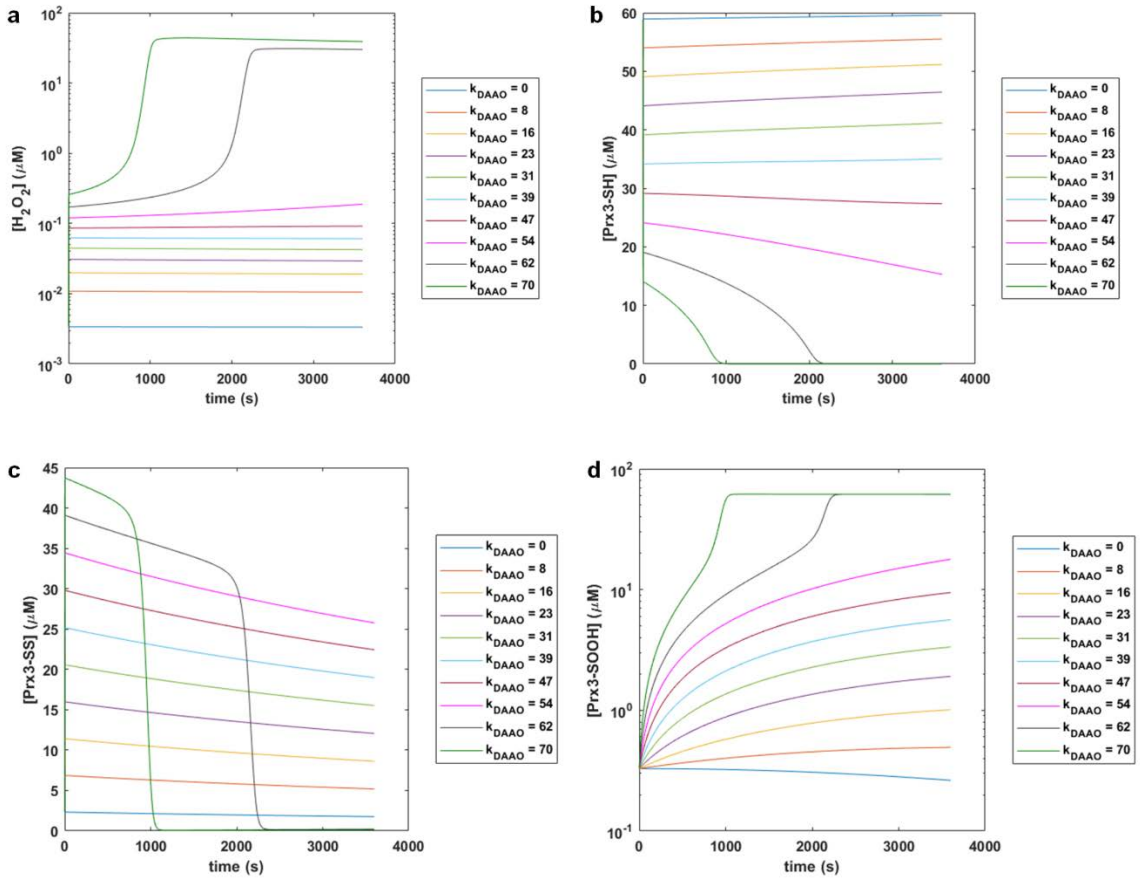


*Figure 3.19: Perturbation Analysis. Plots showing the dynamics of a) [$H_2O_2$], b) [Prx3-SH], c) [Prx3-SS], and d) [Prx3-SOOH] for increasing rates of $k_{DAAO}$. All values of $k_{DAAO}$ in μM/s.*

*Table 3.6: Summary of fractional oxidation with changing $H_2O_2$ perturbations for the major antioxidants in the network at 1 hr*

| **$k_{DAAO}$ (μM/s)** | **Fraction Oxidized** | | | |
|---|---|---|---|---|
| | **Prx3** | **Gpx1** | **Prx5** | **Gpx4** |
| 0 | 0.03 | $7.7x10^{-4}$ | $4.9x10^{-5}$ | $1.2x10^{-6}$ |
| 8 | 0.08 | $2.4x10^{-3}$ | $1.5x10^{-4}$ | $3.9x10^{-6}$ |
| 16 | 0.14 | $4.4x10^{-3}$ | $2.8x10^{-4}$ | $7.0x10^{-6}$ |
| 23 | 0.20 | 0.01 | $4.3x10^{-4}$ | $1.1x10^{-5}$ |
| 31 | 0.25 | 0.01 | $6.2x10^{-4}$ | $1.6x10^{-5}$ |
| 39 | 0.31 | 0.01 | $8.9x10^{-4}$ | $2.2x10^{-5}$ |
| 47 | 0.36 | 0.02 | $1.3x10^{-3}$ | $3.4x10^{-5}$ |
| 54 | 0.42 | 0.04 | $2.8x10^{-3}$ | $7.0x10^{-5}$ |
| 62 | $3.4x10^{-3}$ | 0.87 | 0.22 | 0.01 |
| 70 | $2.6x10^{-3}$ | 0.90 | 0.24 | 0.01 |

In order to evaluate the impact that parameter uncertainties may have on the model predictions, we performed a sensitivity analysis. The value of $\overline{s_i}$ can inform us about both the magnitude and direction that changes in a particular parameter will have on the predictions for a given species of interest. For example, a sensitivity of 1 indicates that a 10% increase in the parameter resulted in a 10% increase in the model output, and likewise, a sensitivity of -1 would signify a 10% decrease in the model output. Figure 3.4 depicts tornado plots of the sensitivities for the concentrations of each $H_2O_2$, Prx3-SH, Prx3-SS, and Prx3-SOOH when there is no perturbation. These plots order the parameters from greatest to least effect on the model output. The model prediction for [$H_2O_2$] was most sensitive to the rate constant of oxidation of Prx3-SH, $k_6$, closely followed by $k_1$, the rate of generation of $H_2O_2$ by OxPhos. Prx3-SS was similarly sensitive to $k_1$ but was most sensitive to $k_{10}$, the rate constant of reduction of Prx3-SS by Trx2-SH. Prx3-SH was not very sensitive to any single model parameter, and Prx3-SOOH was sensitive to several parameters but none with a particularly large magnitude. $k_1$ appeared in all four sensitivity analyses as a top parameter, indicating its importance to all the model predictions. Increasing the value of $k_{DAAO}$ caused the sensitivies to shift, with all four model outputs showing an increasing dependence on $k_{DAAO}$ (Appendix Figure 3.9-3.10). Higher rates of $H_2O_2$ perturbation also caused all four model outputs to become more sensitive to a few more parameters, but all within the Trx2/Prx3 pathway. The sensitivity analysis, therefore, pointed to the model's overall dependence on the rate of $H_2O_2$ input into the system and the kinetic parameters within the Trx2/Prx3 pathway.

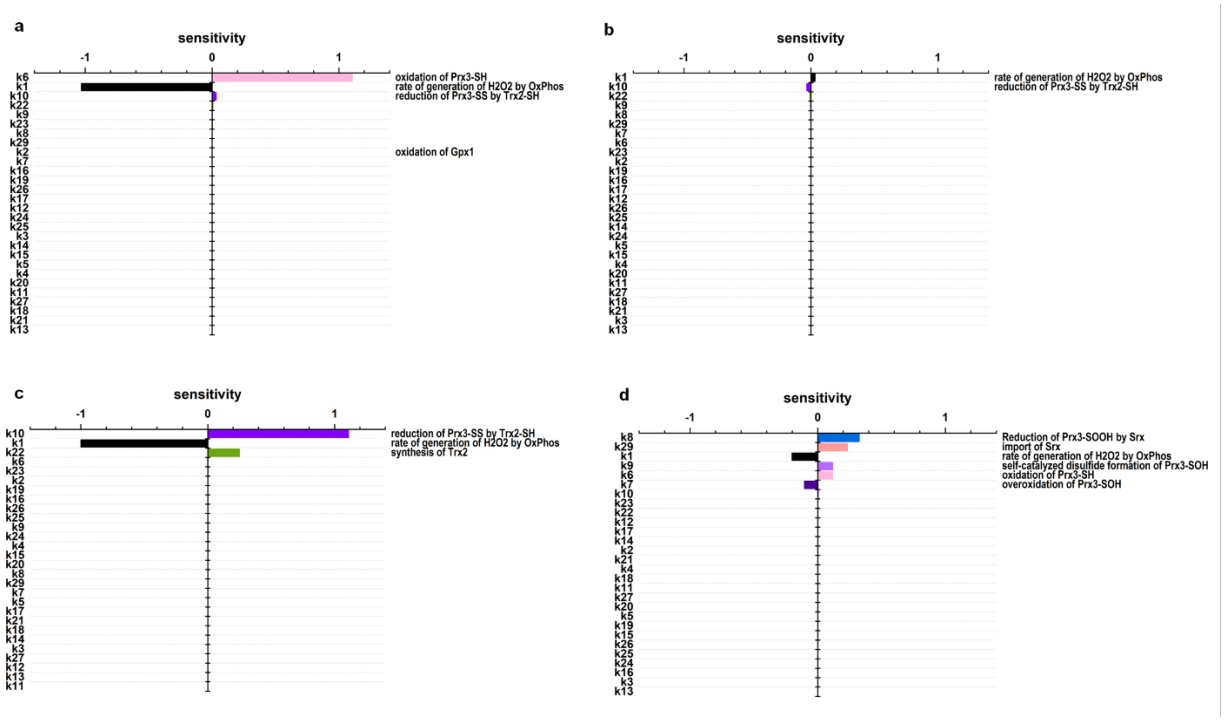


*Figure 3.20: Sensitivity Analysis. Tornado plots of sensitivities to model rate parameters for a) [$H_2O_2$], b) [Prx3-SH], c) [Prx3-SS], and d) [Prx3-SOOH] when $k_{DAAO}$=0. Plots show model rate constants in descending order of sensitivities (absolute value).*

In order to validate the trends predicted by the model as well as test our assumptions, we used the genetically-encoded $H_2O_2$ generator mito-DAAO, which localizes a $H_2O_2$ perturbation to the mitochondrial matrix [10,70]. We varied the concentration of D-alanine (D-ala) substrate the cells were exposed to for up to 1 hr, then probed the Prx isoforms using redox Western blots. The Western blot results are summarized in Figure 3.5. The experimental data demonstrates consistently higher fractions of oxidized Prx3 than what the model predicts, though this discrepancy is most prominent at high perturbations. Where the model predicts disappearance of the dimer and a maximum fractional oxidation of Prx3 around 0.4, the experimental data continues to rise monotonically, reaching a fraction of oxidized Prx3 as high as 0.8. This suggests that the model may be over-predicting hyperoxidation, and therefore the steady-state concentration of $H_2O_2$ reached after each perturbation. The Prx2 data also demonstrate $H_2O_2$ flux in the cytoplasm at certain perturbations after 15 min. At 15 min, while one-way ANOVA testing determined there

was a statistically significant trend in Prx3 mean fractional oxidation at the 95% confidence level (P=0.041), the same test found the Prx2 means to *not* differ across D-ala concentrations (P=0.095) suggesting little effect of transport at this time scale. However, at subsequent times, both Prx3 and Prx2 oxidation demonstrated significant trends at the 99% confidence level, as determined by one-way ANOVA (P=0.004 and P=0.003 for Prx3 and Prx2 at 30 min, $P=1.76\,x\,10^{-5}$ and $P=2.05\,x\,10^{-5}$ for Prx3 and Prx2 at 1 hr). This suggests that transport effects may be playing a larger role at these longer times, as Prx2 oxidation becomes increasingly significant.

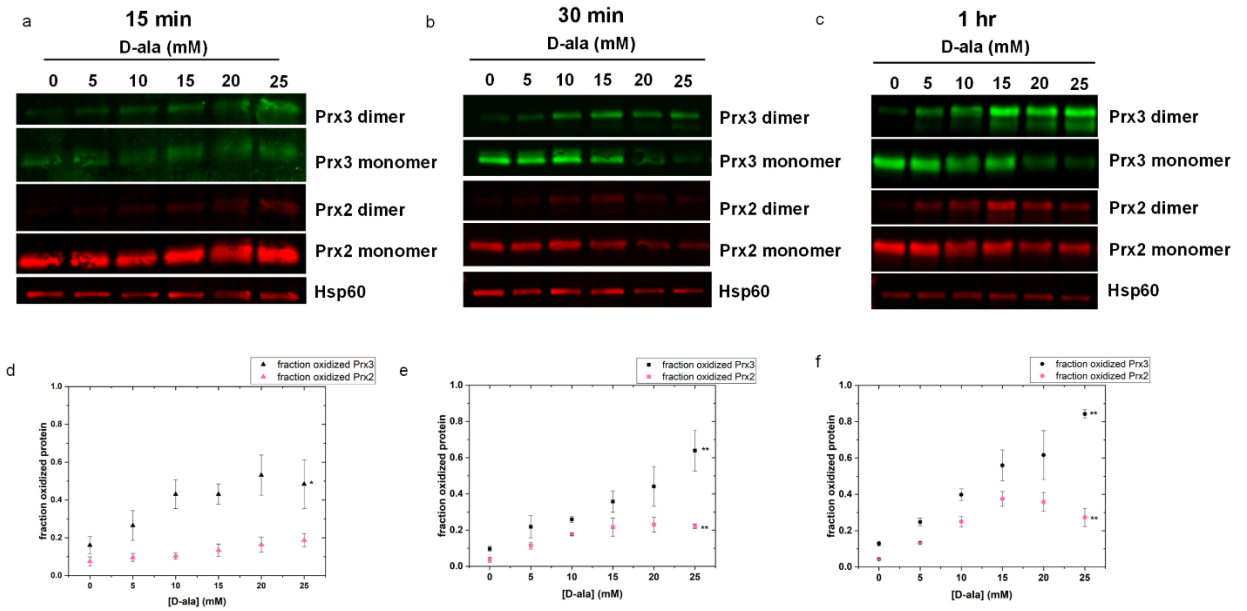


*Figure 3.21: Experimental Validation. Western blot analysis of the oxidized (dimer) and reduced (monomer) Prx isoforms after a) 15 min, b) 30 min, and c) 1 hr of $H_2O_2$ generation by mito-DAAO, with corresponding densitometry plots in d, e, and f, respectively. * represents P<0.05 for one-factor ANOVA, ** represents P<0.01 for one-factor ANOVA. Full Western blot images can be found in Appendix Figure 3.11-3.19.*

## 3.4 Discussion

This model has demonstrated that Prx3 is the controlling antioxidant in the mitochondrial $H_2O_2$ reaction network, as has been previously hypothesized [35]. Because of the dynamics of Prx3, the mitochondrial reaction network is able to control $H_2O_2$ perturbations in the low µM/s range. Only at perturbations that cause total saturation of the Prx3 system do we expect oxidation of Gpx1, Prx5, and Gpx4. Even so, Prx5 and Gpx4 are not really involved in the $H_2O_2$ reaction

network, consistent with the peer-reviewed literature describing their other roles. It has been previously reported that, though Prx5 and Gpx4 are able to react with $H_2O_2$, that is not their primary biological function; Prx5 is the putative reductant of reactive nitrogen species and Gpx4 is hypothesized to react with lipid hydroperoxides [23,57,71].

The model currently predicts a great deal of hyperoxidation of Prx3 at moderate to large perturbation rates. This is inconsistent with experimental observations (Figure 3.5) as well as the field's understanding of the kinetics of Prx3 oxidation. Prx3 is known to be less prone to hyperoxidation as compared with Prx2, as it has faster resolution kinetics of disulfide formation [44,72]. One limitation to accurately predicting hyperoxidation is that the reduction kinetics of the sulfinic acid form of Prx3 have not been well characterized, nor the dynamics of Srx import into and export from the mitochondria. In addition, the reduction of Srx itself is still poorly understood [73]. More careful quantitative analyses of the kinetics governing this reaction pathway will improve our understanding of the dynamics of hyperoxidation.

Currently, transport between the mitochondria and the cytoplasm is ignored. The validity of this assumption is concentration- and time-dependent, as demonstrated by the Prx2 data in Figure 3.5. Under low-perturbation conditions, Prx2 experiences relatively little change in oxidation, suggesting that there is little $H_2O_2$ flux in the cytoplasm under these conditions. However, for mid-range perturbations, the longer the perturbation persists, the greater the contribution of transport becomes (comparing 30 min vs. 1 hr Prx2 oxidation), and for large perturbations, transport appears to be altering cytoplasmic $H_2O_2$ flux even at early times. Physiologically, we expect a variety of transport-related phenomena that might occur over the range of perturbation rates we simulated, including aquaporin-mediated diffusion of $H_2O_2$ into the cytoplasm and even possible depolarization of the mitochondrial membrane cause by the

mitochondrial permeability transition (MPT) [74–76]. Transport of $H_2O_2$ into the cytoplasm could account for why this model over-predicts hyperoxidation, as $H_2O_2$ concentrations in the mitochondria would be too high. Future modeling work can explore how transport of $H_2O_2$ out of the mitochondria affects the reaction network dynamics, which will require quantitative experimental studies to understand these important transport processes and their associated parameters.

Finally, this modeling work helps us understand physiologically relevant concentration regimes in epithelial cell mitochondria, using HeLa cells as a model system. We predicted basal conditions to be in the low nM range, lower than the previously predicted 40 nM [20]. This previous estimate was derived using parameters for a faster respiring cell type, which would produce more $H_2O_2$ through OxPhos, so we expect our basal prediction to be lower. It also demonstrates the usefulness of measuring Prx oxidation as a marker of $H_2O_2$ flux. Other groups have pointed out that the Prxs could be informative biomarkers for certain cancers [77,78]. This model corroborates that idea, and demonstrates not only a relationship between Prx oxidation and $H_2O_2$ perturbation, but also Prx oxidation and the total available pool. Moving forward, this model can be used as a general framework for understanding mitochondrial $H_2O_2$ reaction networks, that can be parametrized to match other cells and tissues as data becomes available.

## 3.5 References


(1) Sies, H. Hydrogen Peroxide as a Central Redox Signaling Molecule in Physiological Oxidative Stress: Oxidative Eustress. *Redox Biol.* **2017**, *11*, 613–619.

(2) Angelova, P. R.; Abramov, A. Y. Functional Role of Mitochondrial Reactive Oxygen Species in Physiology. *Free Radic. Biol. Med.* **2016**, *100*, 81–85.

(3) Lennicke, C.; Rahn, J.; Lichtenfels, R.; Wessjohann, L. A.; Seliger, B. Hydrogen Peroxide – Production, Fate and Role in Redox Signaling of Tumor Cells. *Cell Commun. Signal.* **2015**, *13* (1), 39.

(4) Fu, L.; Liu, K.; Sun, M.; Tian, C.; Sun, R.; Morales Betanzos, C.; Tallman, K. A.; Porter, N. A.; Yang, Y.; Guo, D.; et al. Systematic and Quantitative Assessment of Hydrogen

Peroxide Reactivity With Cysteines Across Human Proteomes. *Mol. Cell. Proteomics* **2017**, *16* (10), 1815–1828.
(5) Lim, J. B.; Langford, T. F.; Huang, B. K.; Deen, W. M.; Sikes, H. D. A Reaction-Diffusion Model of Cytosolic Hydrogen Peroxide. *Free Radic. Biol. Med.* **2016**, *90*, 85–90.
(6) Winterbourn, C. C. Are Free Radicals Involved in Thiol-Based Redox Signaling? *Free Radic. Biol. Med.* **2015**, *80*, 164–170.
(7) Mailloux, R. J.; McBride, S. L.; Harper, M. E. Unearthing the Secrets of Mitochondrial ROS and Glutathione in Bioenergetics. *Trends Biochem. Sci.* **2013**, *38* (12), 592–602.
(8) Bak, D. W.; Weerapana, E. Cysteine-Mediated Redox Signalling in the Mitochondria. *Mol. Biosyst.* **2015**, *11* (3), 678–697.
(9) Hamanaka, R. B.; Chandel, N. S. Mitochondrial Reactive Oxygen Species Regulate Cellular Signaling and Dictate Biological Outcomes. *Trends Biochem. Sci.* **2010**, *35* (9), 505–513.
(10) Stein, K. T.; Moon, S. J.; Sikes, H. D. Mitochondrial H2O2 Generation Using a Tunable Chemogenetic Tool To Perturb Redox Homeostasis in Human Cells and Induce Cell Death. *ACS Synth. Biol.* **2018**, *7* (9), 2037–2044.
(11) Huang, B. K.; Stein, K. T.; Sikes, H. D. Modulating and Measuring Intracellular H 2 O 2 Using Genetically Encoded Tools to Study Its Toxicity to Human Cells. *ACS Synth. Biol.* **2016**, *5* (12), 1389–1395.
(12) Winterbourn, C. C. Reconciling the Chemistry and Biology of Reactive Oxygen Species. *Nat. Chem. Biol.* **2008**, *4* (5), 278–286.
(13) Gauthier, L. D.; Greenstein, J. L.; O'Rourke, B.; Winslow, R. L. An Integrated Mitochondrial ROS Production and Scavenging Model: Implications for Heart Failure. *Biophys. J.* **2013**, *105* (12), 2832–2842.
(14) Kembro, J. M.; Aon, M. A.; Winslow, R. L.; O'Rourke, B.; Cortassa, S. Integrating Mitochondrial Energetics, Redox and ROS Metabolic Networks: A Two-Compartment Model. *Biophys. J.* **2013**, *104* (2), 332–343.
(15) Park, J.; Lee, J.; Choi, C. Mitochondrial Network Determines Intracellular ROS Dynamics and Sensitivity to Oxidative Stress through Switching Inter-Mitochondrial Messengers. *PLoS One* **2011**, *6* (8), e23211.
(16) Wagner, B. A.; Venkataraman, S.; Buettner, G. R. The Rate of Oxygen Utilization by Cells. *Free Radic. Biol. Med.* **2011**, *51* (3), 700–712.
(17) Calvo, S. E.; Clauser, K. R.; Mootha, V. K. MitoCarta2.0: An Updated Inventory of Mammalian Mitochondrial Proteins. *Nucleic Acids Res.* **2016**, *44* (D1), D1251–D1257.
(18) Hall, A.; Karplus, P. A.; Poole, L. B. Typical 2-Cys Peroxiredoxins - Structures, Mechanisms and Functions. *FEBS J.* **2009**, *276* (9), 2469–2477.
(19) Portillo-Ledesma, S.; Randall, L. M.; Parsonage, D.; Dalla Rizza, J.; Karplus, P. A.; Poole, L. B.; Denicola, A.; Ferrer-Sueta, G. Differential Kinetics of Two-Cysteine Peroxiredoxin Disulfide Formation Reveal a Novel Model for Peroxide Sensing. *Biochemistry* **2018**, acs.biochem.8b00188.
(20) Salvador, A.; Antunes, F.; Alves, R.; Marinho, H. S.; Pinto, R. E. Lipid Peroxidation in Mitochondrial Inner Membranes. I. An Integrative Kinetic Model. *Free Radic. Biol. Med.* **2002**, *21* (7), 917–943.
(21) Pannala, V. R.; Dash, R. K. Mechanistic Characterization of the Thioredoxin System in the Removal of Hydrogen Peroxide. *Free Radic. Biol. Med.* **2015**, *78*, 42–55.

(22) Lim, J. B.; Huang, B. K.; Deen, W. M.; Sikes, H. D. Analysis of the Lifetime and Spatial Localization of Hydrogen Peroxide Generated in the Cytosol Using a Reduced Kinetic Model. *Free Radic. Biol. Med.* **2015**, *89*, 47–53.
(23) Trujillo, M.; Carballal, S.; Zeida, A.; Radi, R. Comparative Analysis of Hydrogen Peroxide and Peroxynitrite Reactivity with Thiols. In *Hydrogen Peroxide Metabolism in Health and Disease*; Vissers, M. C. M., Hampton, M. B., Kettle, A. J., Eds.; CRC Press: Boca Raton, FL, 2018; pp 49–79.
(24) Cox, A. G.; Pullar, J. M.; Hughes, G.; Ledgerwood, E. C.; Hampton, M. B. Oxidation of Mitochondrial Peroxiredoxin 3 during the Initiation of Receptor-Mediated Apoptosis. *Free Radic. Biol. Med.* **2008**, *44* (6), 1001–1009.
(25) Trujillo, M.; Clippe, A.; Manta, B.; Ferrer-Sueta, G.; Smeets, A.; Declercq, J. P.; Knoops, B.; Radi, R. Pre-Steady State Kinetic Characterization of Human Peroxiredoxin 5: Taking Advantage of Trp84 Fluorescence Increase upon Oxidation. *Arch. Biochem. Biophys.* **2007**, *467* (1), 95–106.
(26) Hanschmann, E. M.; Lönn, M. E.; Schütte, L. D.; Funke, M.; Godoy, J. R.; Eitner, S.; Hudemann, C.; Lillig, C. H. Both Thioredoxin 2 and Glutaredoxin 2 Contribute to the Reduction of the Mitochondrial 2-Cys Peroxiredoxin Prx3. *J. Biol. Chem.* **2010**, *285* (52), 40699–40705.
(27) Holmgren, A. Thioredoxin Structure and Mechanism: Conformational Changes on Oxidation of the Active-Site Sulfhydryls to a Disulfide. *Structure* **1995**, *3* (3), 239–243.
(28) Itzhak, D. N.; Tyanova, S.; Cox, J.; Borner, G. H. H. Global, Quantitative and Dynamic Mapping of Protein Subcellular Localization. *Elife* **2016**, *5* (JUN2016), 1–36.
(29) Mailloux, R. J.; Craig Ayre, D.; Christian, S. L. Induction of Mitochondrial Reactive Oxygen Species Production by GSH Mediated S-Glutathionylation of 2-Oxoglutarate Dehydrogenase. *Redox Biol.* **2016**, *8*, 285–297.
(30) Ghezzi, P. Protein Glutathionylation in Health and Disease. *Biochim. Biophys. Acta - Gen. Subj.* **2013**, *1830* (5), 3165–3172.
(31) Beer, S. M.; Taylor, E. R.; Brown, S. E.; Dahm, C. C.; Costa, N. J.; Runswick, M. J.; Murphy, M. P. Glutaredoxin 2 Catalyzes the Reversible Oxidation and Glutathionylation of Mitochondrial Membrane Thiol Proteins: Implications for Mitochondrial Redox Regulation and Antioxidant Defense. *J. Biol. Chem.* **2004**, *279* (46), 47939–47951.
(32) Calvo, S. E.; Mootha, V. K. The Mitochondrial Proteome and Human Disease. *Annu. Rev. Genomics Hum. Genet.* **2010**, *11* (1), 25–44.
(33) Noh, Y. H.; Baek, J. Y.; Jeong, W.; Rhee, S. G.; Chang, T.-S. Sulfiredoxin Translocation into Mitochondria Plays a Crucial Role in Reducing Hyperoxidized Peroxiredoxin III. *J. Biol. Chem.* **2009**, *284* (13), 8470–8477.
(34) Ribas, V.; García-Ruiz, C.; Fernández-Checa, J. C. Glutathione and Mitochondria. *Front. Pharmacol.* **2014**, *5 JUL* (July), 1–19.
(35) Cox, A. G.; Winterbourn, C. C.; Hampton, M. B. Mitochondrial Peroxiredoxin Involvement in Antioxidant Defence and Redox Signalling. *Biochem. J.* **2010**, *425* (2), 313–325.
(36) Deponte, M. Glutathione Catalysis and the Reaction Mechanisms of Glutathione-Dependent Enzymes. *Biochim. Biophys. Acta - Gen. Subj.* **2013**, *1830* (5), 3217–3266.
(37) Holmgren, A.; Lu, J. Thioredoxin and Thioredoxin Reductase: Current Research with Special Reference to Human Disease. *Biochem. Biophys. Res. Commun.* **2010**, *396* (1), 120–124.

(38) Chang, T.-S.; Jeong, W.; Woo, H. A.; Lee, S. M.; Park, S.; Rhee, S. G. Characterization of Mammalian Sulfiredoxin and Its Reactivation of Hyperoxidized Peroxiredoxin through Reduction of Cysteine Sulfinic Acid in the Active Site to Cysteine. *J. Biol. Chem.* **2004**, *279* (49), 50994–51001.
(39) Chang, T.-S.; Woo, H. A.; Park, K. J.; Rhee, S. G.; Yang, J. S.; Jeong, W.; Park, S. J. Reduction of Cysteine Sulfinic Acid by Sulfiredoxin Is Specific to 2-Cys Peroxiredoxins. *J. Biol. Chem.* **2004**, *280* (5), 3125–3128.
(40) Treberg, J. R.; Munro, D.; Banh, S.; Zacharias, P.; Sotiri, E. Differentiating between Apparent and Actual Rates of H2O2 Metabolism by Isolated Rat Muscle Mitochondria to Test a Simple Model of Mitochondria as Regulators of H2O2 Concentration. *Redox Biol.* **2015**, *5*, 216–224.
(41) Flohé, L.; Loschen, G.; Gunzler, W. A.; Eichele, E. Glutathione Peroxidase, V. The Kinetic Mechanism. *Hoppe-Seyler's Z. Physiol. Chem.* **1972**, No. 353, 987–999.
(42) Ng, C. F.; Schafer, F. Q.; Buettner, G. R.; Rodgers, V. G. J. The Rate of Cellular Hydrogen Peroxide Removal Shows Dependency on GSH: Mathematical Insight into in Vivo H2O2 and GPx Concentrations. *Free Radic. Res.* **2007**, *41* (11), 1201–1211.
(43) Yeh, G. C.; Occhipinti, S. J.; Cowan, K. H.; Chabner, B. A.; Myers, C. E. Adriamycin Resistance in Human Tumor Cells Associated with Marked Alterations in the Regulation of the Hexose Monophosphate Shunt and Its Response to Oxidant Stress. *Cancer Res.* **1987**, *47* (22), 5994–5999.
(44) Peskin, A. V.; Dickerhof, N.; Poynton, R. A.; Paton, L. N.; Pace, P. E.; Hampton, M. B.; Winterbourn, C. C. Hyperoxidation of Peroxiredoxins 2 and 3: RATE CONSTANTS FOR THE REACTIONS OF THE SULFENIC ACID OF THE PEROXIDATIC CYSTEINE. *J. Biol. Chem.* **2013**, *288* (20), 14170–14177.
(45) Antunes, F.; Brito, P. M. Quantitative Biology of Hydrogen Peroxide Signaling. *Redox Biol.* **2017**, *13*, 1–7.
(46) Sasaki, K.; Bannai, S.; Makino, N. Kinetics of Hydrogen Peroxide Elimination by Human Umbilical Vein Endothelial Cells in Culture. *Biochim. Biophys. Acta - Gen. Subj.* **1998**, *1380* (2), 275–288.
(47) Huang, B. K.; Sikes, H. D. Quantifying Intracellular Hydrogen Peroxide Perturbations in Terms of Concentration. *Redox Biol.* **2014**, *2*, 955–962.
(48) Trujillo, M.; Alvarez, B.; Radi, R. One- and Two-Electron Oxidation of Thiols: Mechanisms, Kinetics and Biological Fates. *Free Radic. Res.* **2016**, *50* (2), 150–171.
(49) Gallogly, M. M.; Mieyal, J. J. Mechanisms of Reversible Protein Glutathionylation in Redox Signaling and Oxidative Stress. *Curr. Opin. Pharmacol.* **2007**, *7* (4), 381–391.
(50) Lo, H.-W.; Antoun, G. R.; Ali-Osman, F. The Human Glutathione S -Transferase P1 Protein Is Phosphorylated and Its Metabolic Function Enhanced by the Ser/Thr Protein Kinases, CAMP-Dependent Protein Kinase and Protein Kinase C, in Glioblastoma Cells. *Cancer Res.* **2004**, *64* (24), 9131–9138.
(51) Johansson, C.; Lillig, C. H.; Holmgren, A. Human Mitochondrial Glutaredoxin Reduces S-Glutathionylated Proteins with High Affinity Accepting Electrons from Either Glutathione or Thioredoxin Reductase. *J. Biol. Chem.* **2004**, *279* (9), 7537–7543.
(52) Srinivasan, U.; Mieyal, P. A.; Mieyal, J. J. PH Profiles Indicative of Rate-Limiting Nucleophilic Displacement in Thioltransferase Catalysis. *Biochemistry* **1997**, *36* (11), 3199–3206.
(53) Henderson, G. B.; Murgolo, N. J.; Kuriyan, J.; Osapay, K.; Kominos, D.; Berry, A.;

Scrutton, N. S.; Hinchliffe, N. W.; Perham, R. N.; Cerami, A. Engineering the Substrate Specificity of Glutathione Reductase toward That of Trypanothione Reduction. *Proc. Natl. Acad. Sci. U. S. A.* **1991**, *88* (19), 8769–8773.
(54) Arnér, E. S. J.; Zhong, L.; Holmgren, A. Preparation and Assay of Mammalian Thioredoxin and Thioredoxin Reductase. In *Methods in Enzymology*; 1999; pp 226–239.
(55) Kemp, M.; Go, Y.-M.; Jones, D. P. Nonequilibrium Thermodynamics of Thiol/Disulfide Redox Systems: A Perspective on Redox Systems Biology. *Free Radic. Biol. Med.* **2008**, *44* (6), 921–937.
(56) Kondo, N.; Ishii, Y.; Kwon, Y.-W.; Tanito, M.; Horita, H.; Nishinaka, Y.; Nakamura, H.; Yodoi, J. Redox-Sensing Release of Human Thioredoxin from T Lymphocytes with Negative Feedback Loops. *J. Immunol.* **2004**, *172* (1), 442–448.
(57) Han, X.; Fan, Z.; Yu, Y.; Liu, S.; Hao, Y.; Huo, R.; Wei, J. Expression and Characterization of Recombinant Human Phospholipid Hydroperoxide Glutathione Peroxidase. *IUBMB Life* **2013**, *65* (11), 951–956.
(58) Kil, I. S.; Ryu, K. W.; Lee, S. K.; Kim, J. Y.; Chu, S. Y.; Kim, J. H.; Park, S.; Rhee, S. G. Circadian Oscillation of Sulfiredoxin in the Mitochondria. *Mol. Cell* **2015**, *59* (4), 651–663.
(59) Arteel, G. E.; Briviba, K.; Sies, H. Protection against Peroxynitrite. *FEBS Lett.* **1999**, *445* (2–3), 226–230.
(60) Philips, R. M. & R. » {How} big are mitochondria? http://book.bionumbers.org/how-big-are-mitochondria/ (accessed Jun 1, 2018).
(61) Posakony, J. W.; England, J. M.; Attardi, G. Mitochondrial Growth and Division during the Cell Cycle in HeLa Cells. *J. Cell Biol.* **1977**, *74* (2), 468–491.
(62) Watabe S; Hiroi T; Yamamoto Y; Fujioka Y; Hasegawa H; Yago N; Takahashi S Y. SP-22 Is a Thioredoxin-Dependent Peroxide Reductase in Mitochondria. *Eur. J. Biochem.* **1997**, *249* (1), 52–60.
(63) Lee, M. H.; Han, J. H.; Lee, J. H.; Choi, H. G.; Kang, C.; Kim, J. S. Mitochondrial Thioredoxin-Responding off-on Fluorescent Probe. *J. Am. Chem. Soc.* **2012**, *134* (41), 17314–17319.
(64) Adimora, N. J.; Jones, D. P.; Kemp, M. L. A Model of Redox Kinetics Implicates the Thiol Proteome in Cellular Hydrogen Peroxide Responses. *Antioxid. Redox Signal.* **2010**, *13* (6), 731–743.
(65) Martinovich, G. G.; Cherenkevich, S. N.; Sauer, H. Intracellular Redox State: Towards Quantitative Description. *Eur. Biophys. J.* **2005**, *34* (7), 937–942.
(66) Schafer, F. Q.; Buettner, G. R. Redox Environment of the Cell as Viewed through the Redox State of the Glutathione Disulfide/Glutathione Couple. *Free Radic. Biol. Med.* **2001**, *30* (11), 1191–1212.
(67) Yue, H.; Brown, M.; Knowles, J.; Wang, H.; Broomhead, D. S.; Kell, D. B. Insights into the Behaviour of Systems Biology Models from Dynamic Sensitivity and Identifiability Analysis: A Case Study of an NF-KB Signalling Pathway. *Mol. Biosyst.* **2006**, *2* (12), 640–649.
(68) Cox, A. G.; Winterbourn, C. C.; Hampton, M. B. Measuring the Redox State of Cellular Peroxiredoxins by Immunoblotting. In *Methods in enzymology*; Elsevier Inc., 2010; Vol. 474, pp 51–66.
(69) Powers, J. F.; Cochran, B.; Baleja, J. D.; Sikes, H. D.; Zhang, X.; Lomakin, I.; Langford, T.; Stein, K. T.; Tischler, A. S. A Unique Model for SDH-Deficient GIST: An Endocrine-

Related Cancer. *Endocr. Relat. Cancer* **2018**, *25* (11), 943–954.
(70) Alim, I.; Haskew-Layton, R. E.; Aleyasin, H.; Guo, H.; Ratan, R. R. Spatial, Temporal, and Quantitative Manipulation of Intracellular Hydrogen Peroxide in Cultured Cells. *Methods Enzymol.* **2014**, *547* (1), 251–273.
(71) Yang, W. S.; SriRamaratnam, R.; Welsch, M. E.; Shimada, K.; Skouta, R.; Viswanathan, V. S.; Cheah, J. H.; Clemons, P. A.; Shamji, A. F.; Clish, C. B.; et al. Regulation of Ferroptotic Cancer Cell Death by GPX4. *Cell* **2014**, *156* (1–2), 317–331.
(72) Cox, A. G.; Pearson, A. G.; Pullar, J. M.; Jönsson, T. J.; Lowther, W. T.; Winterbourn, C. C.; Hampton, M. B. Mitochondrial Peroxiredoxin 3 Is More Resilient to Hyperoxidation than Cytoplasmic Peroxiredoxins. *Biochem. J.* **2009**, *421* (1), 51–58.
(73) Lowther, W. T.; Haynes, A. C. Reduction of Cysteine Sulfinic Acid in Eukaryotic, Typical 2-Cys Peroxiredoxins by Sulfiredoxin. *Antioxid. Redox Signal.* **2010**, *15* (1), 99–109.
(74) Halestrap, A. P.; Clarke, S. J.; Javadov, S. A. Mitochondrial Permeability Transition Pore Opening during Myocardial Reperfusion - A Target for Cardioprotection. *Cardiovasc. Res.* **2004**, *61* (3), 372–385.
(75) Hansson, M. J.; Månsson, R.; Morota, S.; Uchino, H.; Kallur, T.; Sumi, T.; Ishii, N.; Shimazu, M.; Keep, M. F.; Jegorov, A.; et al. Calcium-Induced Generation of Reactive Oxygen Species in Brain Mitochondria Is Mediated by Permeability Transition. *Free Radic. Biol. Med.* **2008**, *45* (3), 284–294.
(76) Marchissio, M. J.; Francés, D. E. A.; Carnovale, C. E.; Marinelli, R. A. Mitochondrial Aquaporin-8 Knockdown in Human Hepatoma HepG2 Cells Causes ROS-Induced Mitochondrial Depolarization and Loss of Viability. *Toxicol. Appl. Pharmacol.* **2012**, *264* (2), 246–254.
(77) Fischer, J.; Eglinton, T.; Frizelle, F.; Hampton, M. Peroxiredoxins in Colorectal Cancer: Predictive Biomarkers of Radiation Response and Therapeutic Targets to Increase Radiation Sensitivity? *Antioxidants* **2018**, *7* (10), 136.
(78) Poynton, R. a; Hampton, M. B. Peroxiredoxins as Biomarkers of Oxidative Stress. *Biochim. Biophys. Acta* **2014**, *1840* (2), 906–912.
(79) Jones, D. P. Radical-Free Biology of Oxidative Stress. *Am. J. Physiol. Physiol.* **2008**, *295* (4), C849–C868.
(80) Scott Fogler, H. Elements of Chemical Reaction Engineering. *Chem. Eng. Sci.* **2002**.

## 3.6 Appendix

*3.6.1 : Calculations*

The rate of $H_2O_2$ generation from the electron transport chain (ETC) due to oxidative phosphorylation (OxPhos) was calculated based on oxygen consumption rate (OCR) data and $H_2O_2$ production rate data from respiring mitochondria isolated from rat liver [16,40]. We reconciled the data from these two sources in order to estimate this important parameter.

The reported OCR from HeLa cells was $200\frac{\text{amol}}{\text{ng-protein*s}}$ [16]. HeLa cell protein concentration was reported as $2x10^5$ mg/L [28], so we used this number to convert the reported OCR to 40 µM/s. Up to 10% of the $O_2$ consumption can be assumed to get converted to $H_2O_2$ [79], giving a value of 4 µM/s $H_2O_2$ produced by OxPhos.

$$200\frac{\text{amol}}{\text{ng-protein*s}} * 2x10^{11}\frac{\text{ng-protein}}{\text{L}} * 10\% = 4x10^{13}\,\text{aM}/\text{s} = 4\,\mu\text{M}/\text{s} \tag{0.7}$$

The data reported by Treberg *et al.* provided a range of possible $H_2O_2$ production rates, as measured extramitochondrially. Based on the methodology presented in their paper, any measured extramitochondrial $H_2O_2$ rates are lower than what is actually produced because some $H_2O_2$ has already been consumed by the mitochondrial antioxidant network [40]. They propose the following equation:

$$\frac{V_p}{k} = \left[H_2O_2\right]_{ss} \tag{0.8}$$

where $V_p$ is the rate of $H_2O_2$ production, $k$ is the first order rate constant that describes the mitochondrial reaction network, and $\left[H_2O_2\right]_{ss}$ is the steady state concentration of $H_2O_2$. For our system, $k$ is the pseudo-first order rate constant of Prx3, equal to 1200 $s^{-1}$, as this is the largest

kinetic constant in our network. Applying our rate constants with the reported $\left[H_2O_2\right]_{ss}$ of $1\frac{\text{nmol}}{\text{min-mg}}$ [40] we can calculate an $H_2O_2$ production rate of 5 μM/s. This is the same order of magnitude as the 4 μM/s calculated by using the OCR approach above, and we took the number associated with the OCR data as this was measured from HeLa cells rather than rat liver mitochondria.

To convert copy number reported by Itzhak *et al.* [28] to a mitochondrial protein concentration, the following calculations were carried out:

$$c_i = \frac{n}{N_A N_{mito} V_{mito}} \tag{0.9}$$

where $c_i$ is the concentration of protein *i*, *n* is the protein copy number associated with all the mitochondria in a single cell (given in the proteomics dataset), $N_A$ is Avogadro's number, $N_{mito}$ is the number of mitochondria in a single cell (383 – 882) [61], and $V_{mito}$ is the volume of one mitochondrion (0.29 $\mu m^3$) [60]. If the protein was not reported in the organelle-specific dataset, but is known to localize in the mitochondria (the glutathione peroxidases) then its copy number was pulled from the proteome-wide dataset and then the mitochondrial concentration was still calculated in this manner.

The initial concentration of $H_2O_2$ used in the model at $t = 0$ was calculated based on the consumption by Prx3:

$$c_{H_2O_2,i} = \frac{k_1}{k_6 c_{Prx3-SH,T}} \tag{0.10}$$

The magnitude of the Prx3-SH term is much larger than any other terms we might have included in this calculation, so this reduced term is sufficient to initialize the model.

For related isoforms of proteins, the pseudo-steady state assumption was used to find the initial concentrations of each species [80]. For the Prx3 isoforms, those calculations were as follows:

$$c_{\mathrm{Prx3-SOH},i} = \frac{c_{\mathrm{Prx3-SH},T}}{\frac{k_9}{k_6 c_{H_2O_2,i}} + 1 + \frac{k_9}{k_{10} c_{Trx2-SH,i}} + \frac{k_7 c_{H_2O_2,i}}{k_8 c_{Srx,i}}} \tag{0.11}$$

$$c_{\mathrm{Prx3-SOOH},i} = \frac{k_7 c_{\mathrm{Prx3-SH},T} c_{H_2O_2,i}}{k_8 c_{Srx,i}\left(\frac{k_9}{k_6 c_{H_2O_2,i}} + 1 + \frac{k_9}{k_{10} c_{Trx2-SH,i}} + \frac{k_7 c_{H_2O_2,i}}{k_8 c_{Srx,i}}\right)} \tag{0.12}$$

$$c_{\mathrm{Prx3-SS},i} = \frac{k_9 c_{\mathrm{Prx3-SH},T}}{k_{10} c_{Trx2-SH,i}\left(\frac{k_9}{k_6 c_{H_2O_2,i}} + 1 + \frac{k_9}{k_{10} c_{Trx2-SH,i}} + \frac{k_7 c_{H_2O_2,i}}{k_8 c_{Srx,i}}\right)} \tag{0.13}$$

$$c_{\mathrm{Prx3-SH},i} = c_{\mathrm{Prx3-SH},T} - c_{\mathrm{Prx3-SOH}} - c_{\mathrm{Prx3-SOOH}} - c_{\mathrm{Prx3-SS}} \tag{0.14}$$

The same strategy was followed for the other protein families for consistent initialization.

*3.6.2 : System of ODEs*

$$\frac{dc_{H_2O_2}}{dt} = k_1 + k_{DAAO} - c_{H_2O_2}\left(k_2 c_{Gpx1red} - k_6 c_{Prx3-SH} - k_7 c_{Prx3-SOH} - k_{12} c_{Pr-SH} - k_{16} c_{Pr-(SH)_2} - k_{23} c_{Prx5-SH} - k_{26} c_{Gpx4red}\right) \tag{0.15}$$

$$\frac{dc_{Gpx1red}}{dt} = -k_2 c_{Gpx1red} c_{H_2O_2} + k_4 c_{Gpx1-SSG} c_{GSH} \tag{0.16}$$

$$\frac{dc_{Gpx1ox}}{dt} = k_2 c_{Gpx1red} c_{H_2O_2} - k_3 c_{Gpx1ox} c_{GSH} \tag{0.17}$$

$$\frac{dc_{Gpx1-SSG}}{dt} = k_3 c_{Gpx1ox} c_{GSH} - k_4 c_{Gpx1-SSG} c_{GSH} \tag{0.18}$$

$$\frac{dc_{GSH}}{dt} = c_{GSH}\left(-k_3 c_{Gpx1ox} - k_4 c_{Gpx1-SSG} - 2k_{11} - k_{13} c_{Pr-SOH} - k_{15} c_{Grx2-SSG} - k_{27} c_{Gpx4ox} - k_4 c_{Gpx4-SSG}\right) + 2k_{18} c_{GSSG} c_{NADPH} + k_{21} \tag{0.19}$$

$$\frac{dc_{GSSG}}{dt} = c_{GSH}\left(k_4 c_{Gpx1-SSG} + k_{11} + k_{15} c_{Grx-SSG} + k_4 c_{Gpx4-SSG}\right) - k_{18} c_{NADPH} c_{GSSG} \tag{0.20}$$

$$\frac{dc_{Prx3-SH}}{dt} = -k_6 c_{Prx3-SH} c_{H_2O_2} + k_{10} c_{Prx3-SS} c_{Trx2-SH} \tag{0.21}$$

$$\frac{dc_{Prx3-SOH}}{dt} = k_6 c_{Prx3-SH} c_{H_2O_2} - k_7 c_{Prx3-SOH} c_{H_2O_2} + k_8 c_{Prx3-SOOH} c_{Srx} - k_9 c_{Prx3-SOH} \tag{0.22}$$

$$\frac{dc_{Prx3-SOOH}}{dt} = k_7 c_{Prx3-SOH} c_{H_2O_2} - k_8 c_{Prx3-SOOH} c_{Srx} \tag{0.23}$$

$$\frac{dc_{Prx3-SS}}{dt} = k_9 c_{Prx3-SOH} - k_{10} c_{Prx3-SS} c_{Trx2-SH} \tag{0.24}$$

$$\frac{dc_{Trx2-SH}}{dt} = -c_{Trx2-SH}\left(k_{10} c_{Prx3-SS} + k_{17} c_{Pr-SS} + k_{25} c_{Prx5-SS}\right) + k_{19} c_{Trx2-SS} c_{NADPH} + k_{22} \tag{0.25}$$

$$\frac{dc_{Trx2-SS}}{dt} = c_{Trx2-SS}\left(k_{10} c_{Prx3-SS} + k_{17} c_{Pr-SS} + k_{25} c_{Prx5-SS}\right) - k_{19} c_{Trx2-SS} c_{NADPH} \tag{0.26}$$

$$\frac{dc_{Pr-SH}}{dt} = -k_{12} c_{Pr-SH} c_{H_2O_2} + k_{14} c_{Pr-SSG} c_{Grx2-SH} \tag{0.27}$$

$$\frac{dc_{Pr-SOH}}{dt} = k_{12} c_{Pr-SH} c_{H_2O_2} - k_{13} c_{Pr-SOH} c_{GSH} \tag{0.28}$$

$$\frac{dc_{Pr-SSG}}{dt} = k_{13} c_{Pr-SOH} c_{GSH} - k_{14} c_{Pr-SSG} c_{Grx2-SH} \tag{0.29}$$

$$\frac{dc_{Grx2-SH}}{dt} = k_{15} c_{Grx2-SSG} c_{GSH} - k_{14} c_{Grx2-SH} c_{Pr-SSG} \tag{0.30}$$

$$\frac{dc_{Grx2-SSG}}{dt} = k_{14} c_{Pr-SSG} c_{Grx2-SH} - k_{15} c_{Grx2-SSG} c_{GSH} \tag{0.31}$$

$$\frac{dc_{Pr-(SH)_2}}{dt} = -k_{16}c_{Pr-(SH)_2}c_{H_2O_2} + k_{17}c_{Pr-SS}c_{Trx2-SH} \tag{0.32}$$

$$\frac{dc_{Pr-SS}}{dt} = k_{16}c_{Pr-(SH)_2}c_{H_2O_2} - k_{17}c_{Pr-SS}c_{Trx2-SH} \tag{0.33}$$

$$\frac{dc_{NADPH}}{dt} = c_{NADPH}\left(-k_{18}c_{GSSG} - k_{19}c_{Trx2-SS}\right) + \frac{k_{20}c_{NADP^+}}{k_5 + c_{NADP^+}} \tag{0.34}$$

$$\frac{dc_{NADP^+}}{dt} = c_{NADPH}\left(k_{18}c_{GSSG} + k_{19}c_{Trx2-SS}\right) - \frac{k_{20}c_{NADP^+}}{k_5 + c_{NADP^+}} \tag{0.35}$$

$$\frac{dc_{Prx5-SH}}{dt} = -k_{23}c_{Prx5-SH}c_{H_2O_2} + k_{25}c_{Prx5-SS}c_{Trx2-SH} \tag{0.36}$$

$$\frac{dc_{Prx5-SOH}}{dt} = k_{23}c_{Prx5-SH}c_{H_2O_2} - k_{24}c_{Prx5-SOH} \tag{0.37}$$

$$\frac{dc_{Prx5-SS}}{dt} = k_{24}c_{Prx5-SOH} - k_{25}c_{Prx5-SS}c_{Trx2-SH} \tag{0.38}$$

$$\frac{dc_{Gpx4red}}{dt} = -k_{26}c_{Gpx4red}c_{H_2O_2} + k_4c_{Gpx4-SSG}c_{GSH} \tag{0.39}$$

$$\frac{dc_{Gpx4ox}}{dt} = k_{26}c_{Gpx4red}c_{H_2O_2} - k_{27}c_{Gpx4ox}c_{GSH} \tag{0.40}$$

$$\frac{dc_{Gpx4-SSG}}{dt} = k_{27}c_{Gpx4ox}c_{GSH} - k_4c_{Gpx4-SSG}c_{GSH} \tag{0.41}$$

$$\frac{dc_{Srx}}{dt} = k_{29} \tag{0.42}$$

*3.6.3 : Figures*

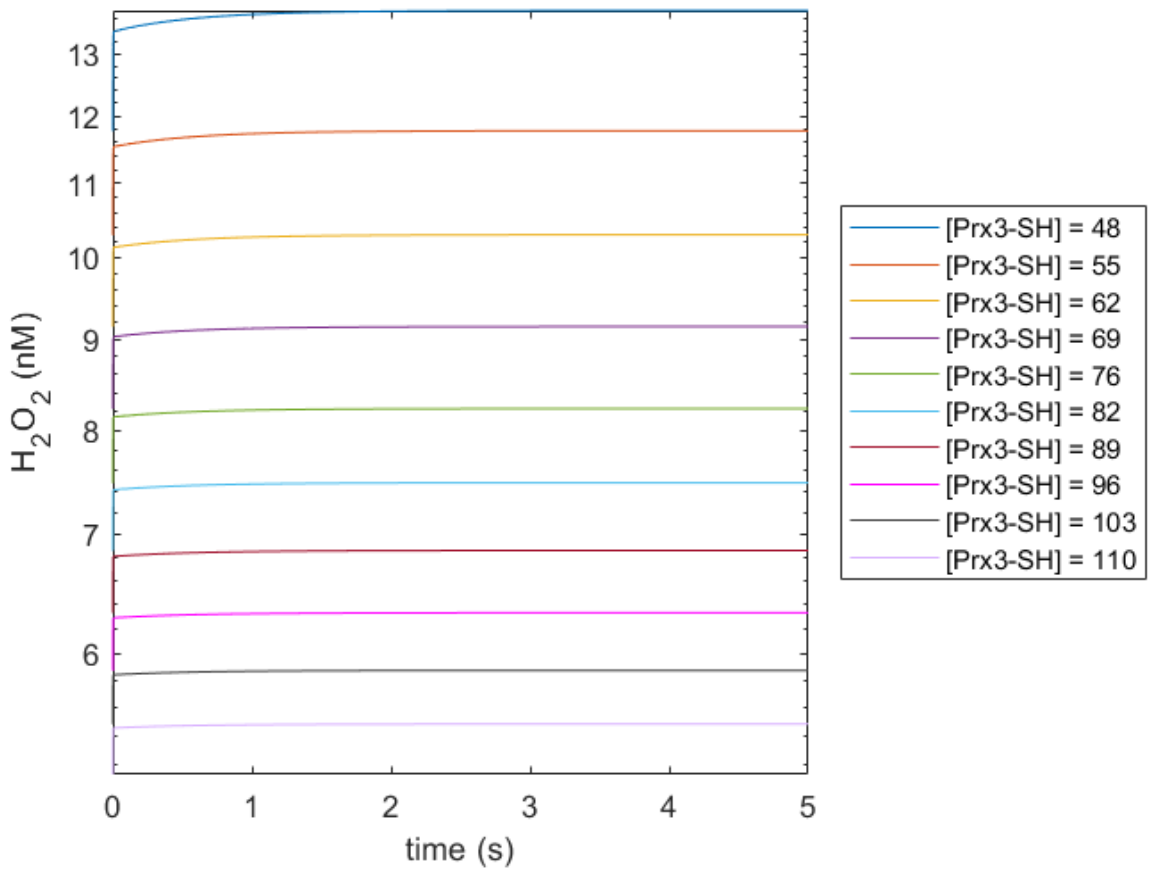


*Figure 3.22: Baseline $H_2O_2$ concentration as a function of Prx3 pool for a higher $H_2O_2$ generation rate by OxPhos (11 µM/s). A value of 4 µM/s was used to generate the figures used in the main text.*

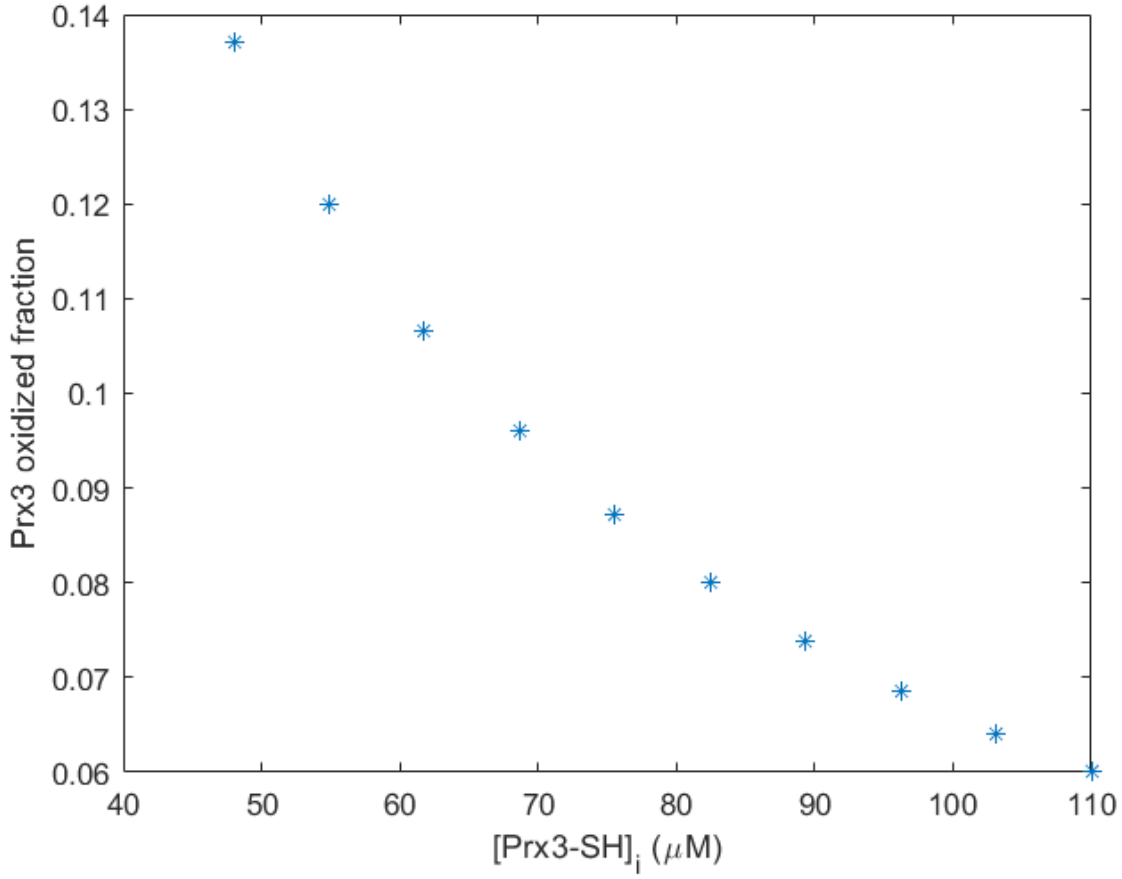


*Figure 3.23: Dimer fraction as a function of Prx3 pool for a higher rate of $H_2O_2$ generation from OxPhos (11 µM/s). A value of 4 µM/s was used to generate the figures used in the main text.*

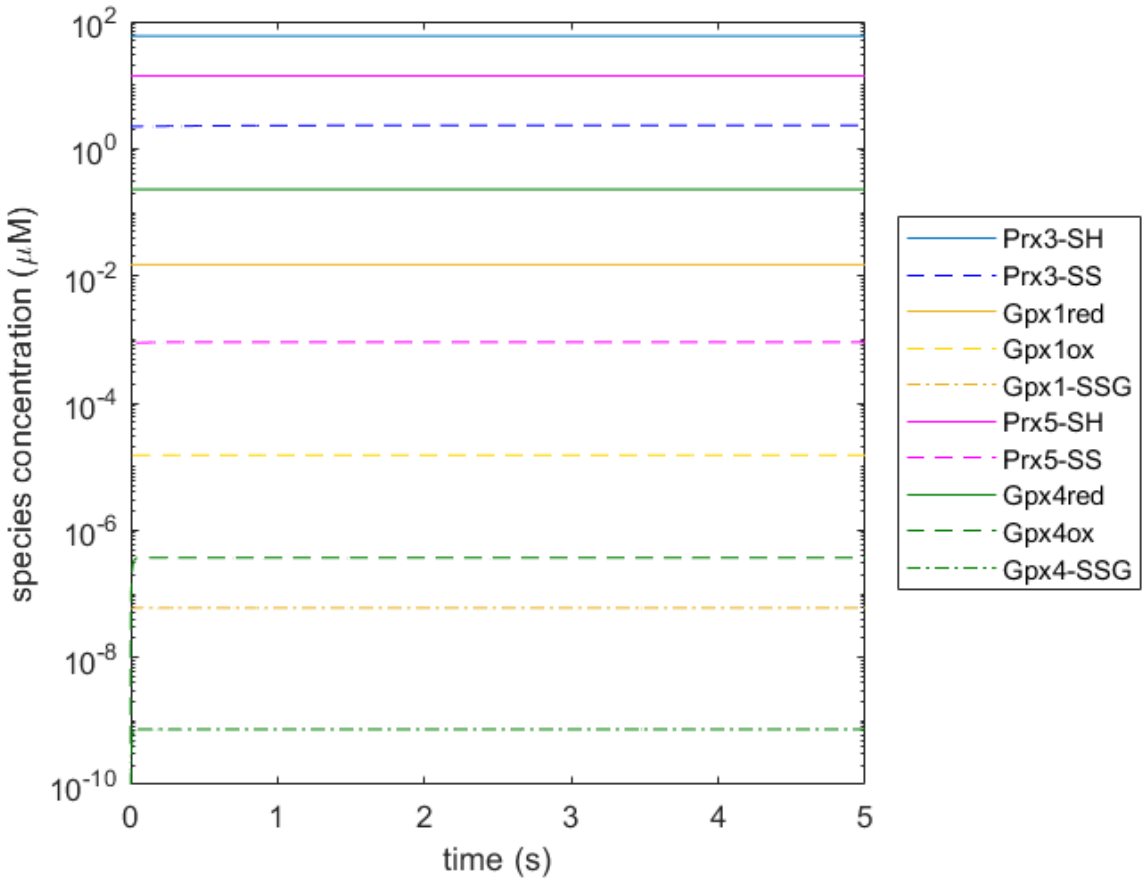


*Figure 3.24: Baseline concentrations of reduced and oxidized isoforms of major antioxidant species for a fixed pool of Prx3 (62 μM) and a higher rate of $H_2O_2$ generation by OxPhos (11 μM/s). A value of 4 μM/s was used to generate the figures used in the main text.*

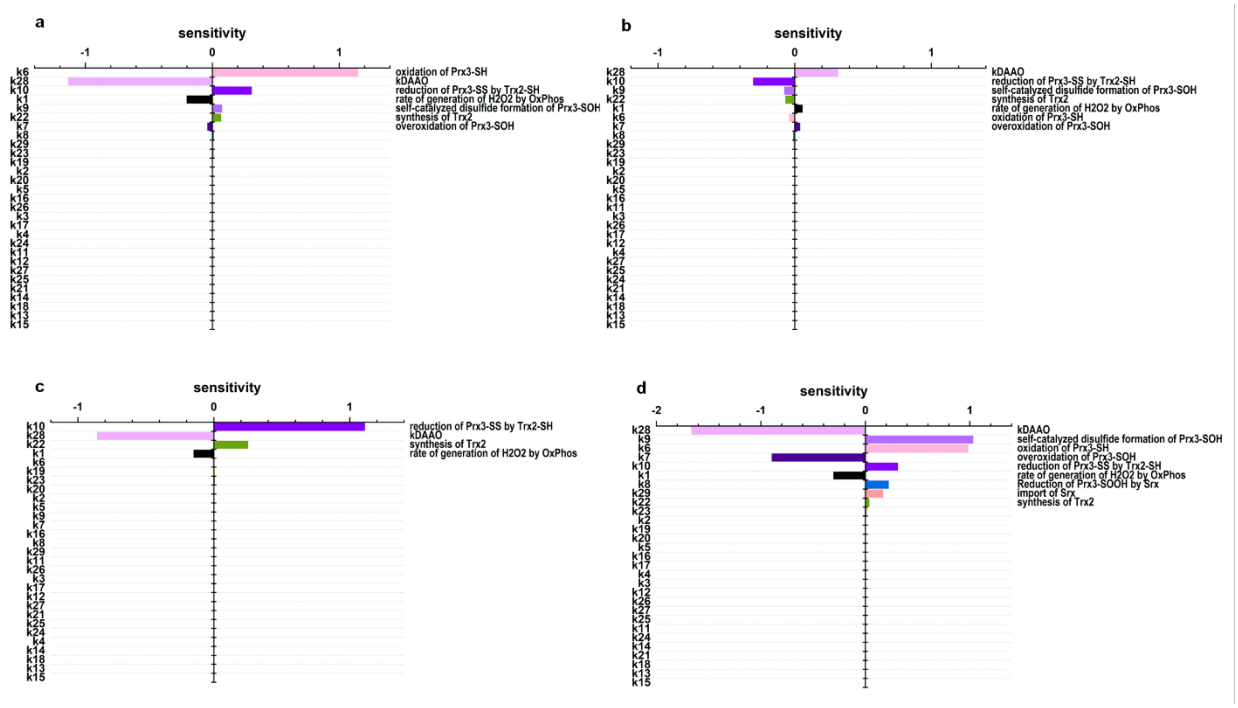


*Figure 3.25: Sensitivity Analysis. Tornado plots of sensitivities to model rate parameters for a) [H2O2], b) [Prx3-SH], c) [Prx3-SS], and d) [Prx3-SOOH] when kDAAO=23 µM/s. Plots show model rate constants in descending order of sensitivities (absolute value).*

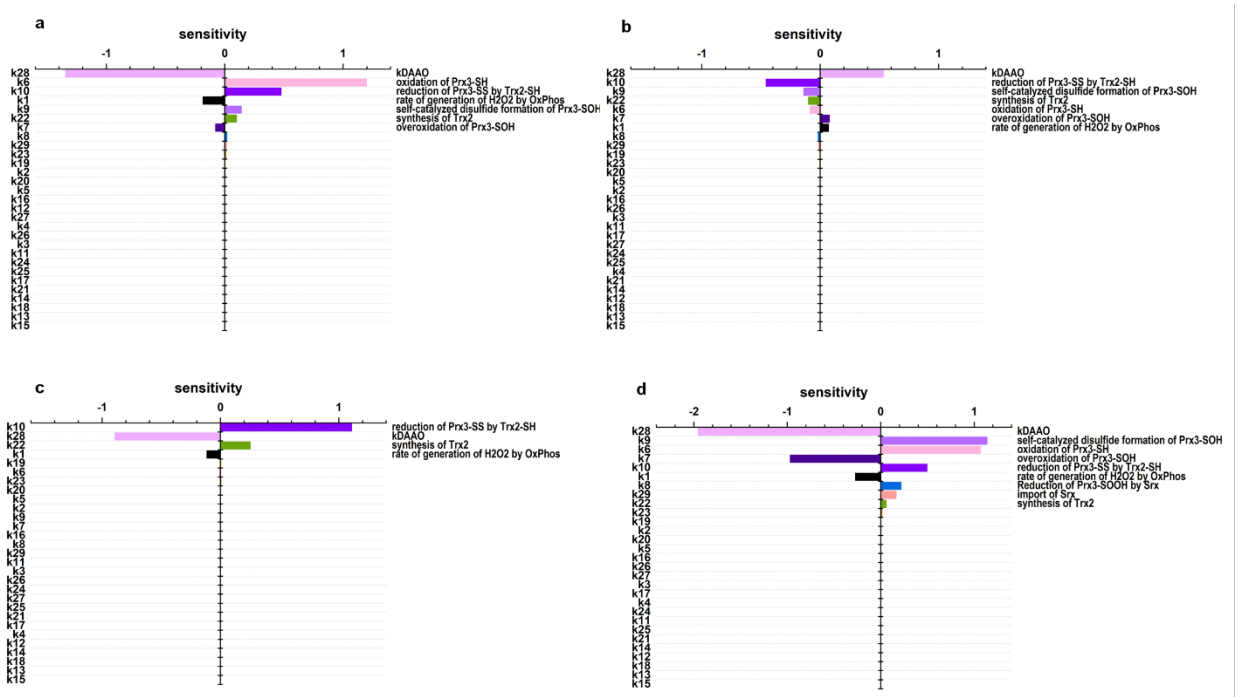


*Figure 3.26: Sensitivity Analysis. Tornado plots of sensitivities to model rate parameters for a) [H2O2], b) [Prx3-SH], c) [Prx3-SS], and d) [Prx3-SOOH] when kDAAO=31 µM/s. Plots show model rate constants in descending order of sensitivities (absolute value).*

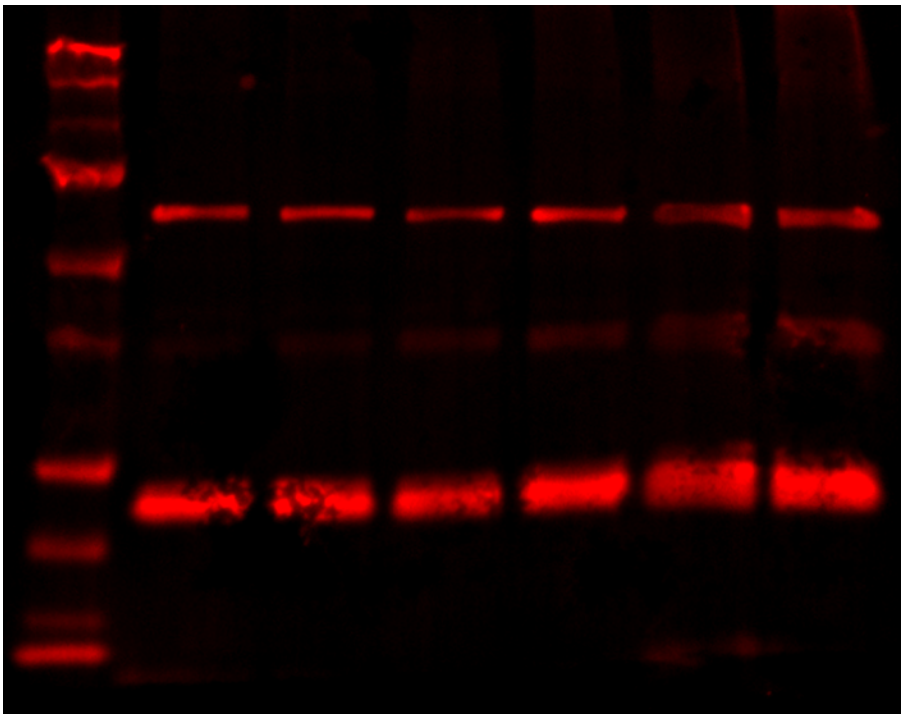

*Figure 3.27: Full Western blot image from Figure 3.5 stained for Prx2 and Hsp60, visualized using IRDye680, showing samples from 15 min of generation, 0 – 25 mM D-ala (left to right).*

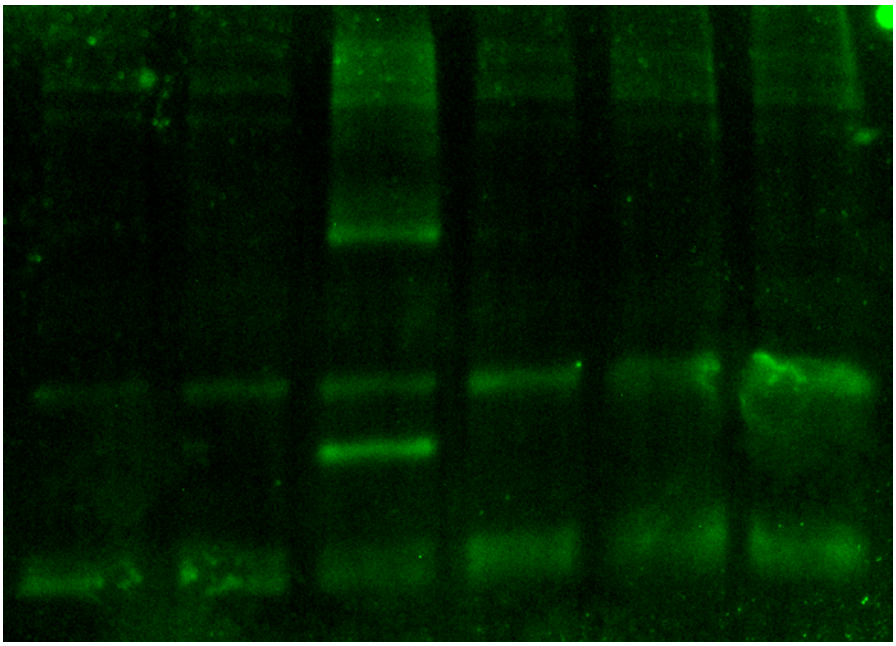

*Figure 3.28: Full Western blot image from Figure 3.5 stained for Prx3, visualized using IRDye800, showing samples from 15 min of generation, 0 – 25 mM D-ala (left to right).*

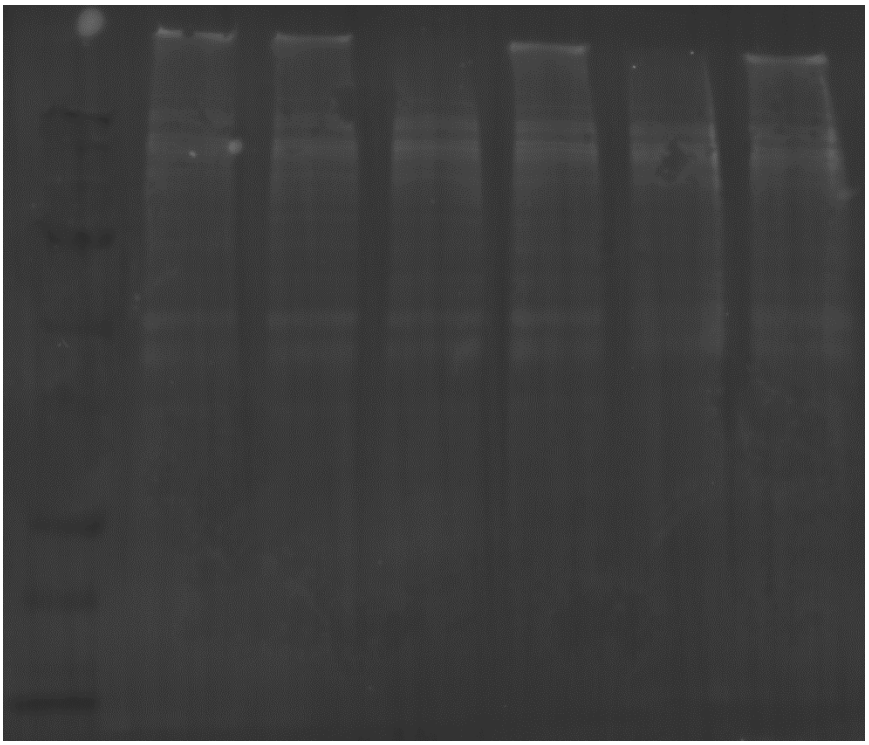

*Figure 3.29: Corresponding stain-free total protein image of 15 min Western blot*

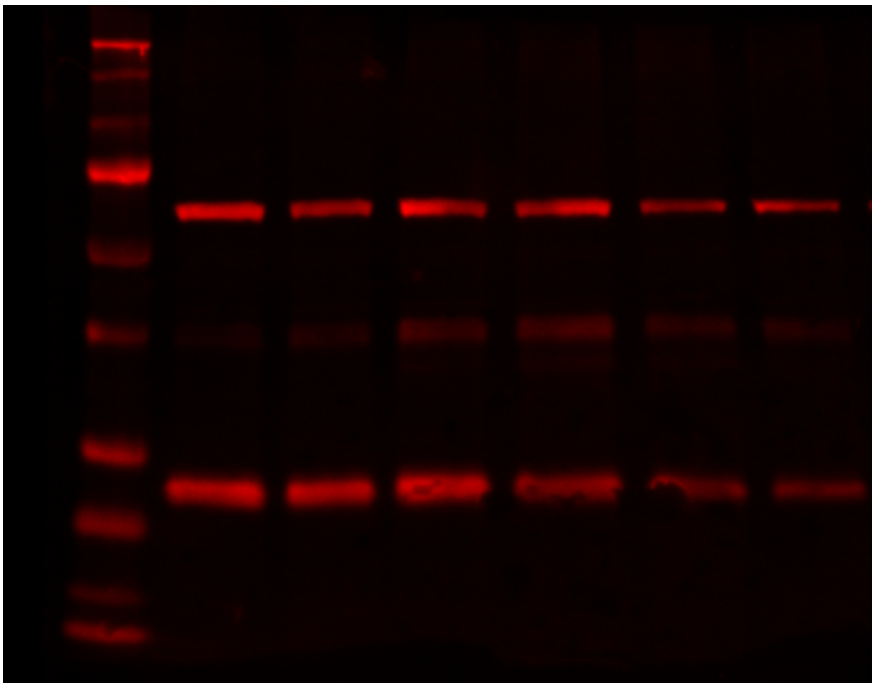

*Figure 3.30: Full Western blot image from Figure 3.5 stained for Prx2 and Hsp60, visualized using IRDye680, showing samples from 30 min of generation, 0 – 25 mM D-ala (left to right).*

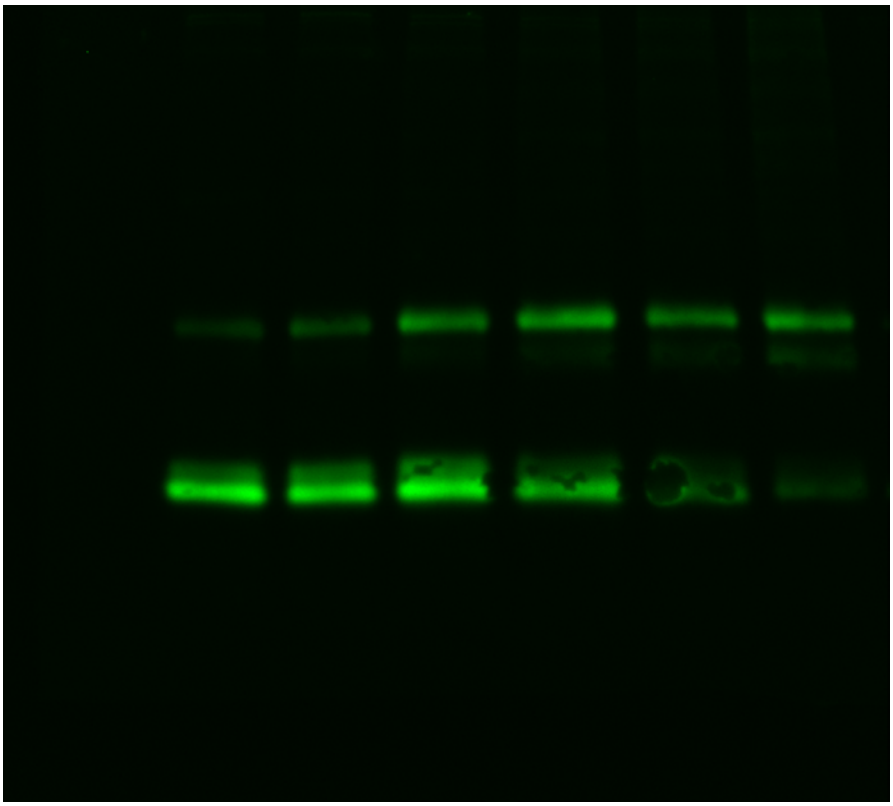

*Figure 3.31: Full Western blot image from Figure 3.5 stained for Prx3, visualized using IRDye800, showing samples from 30 min of generation, 0 – 25 mM D-ala (left to right).*

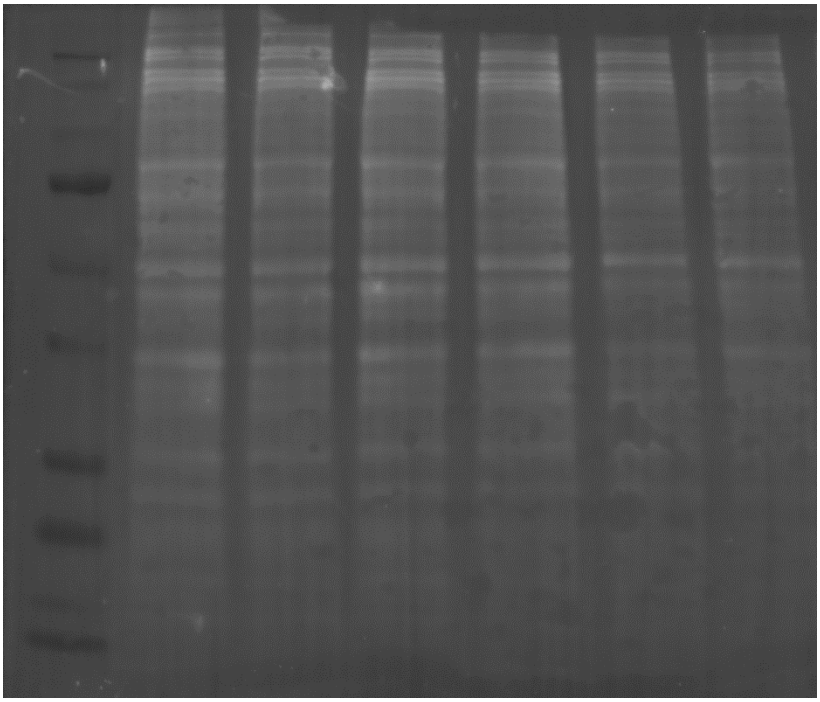

*Figure 3.32: Corresponding stain-free total protein image of 30 min Western blot*

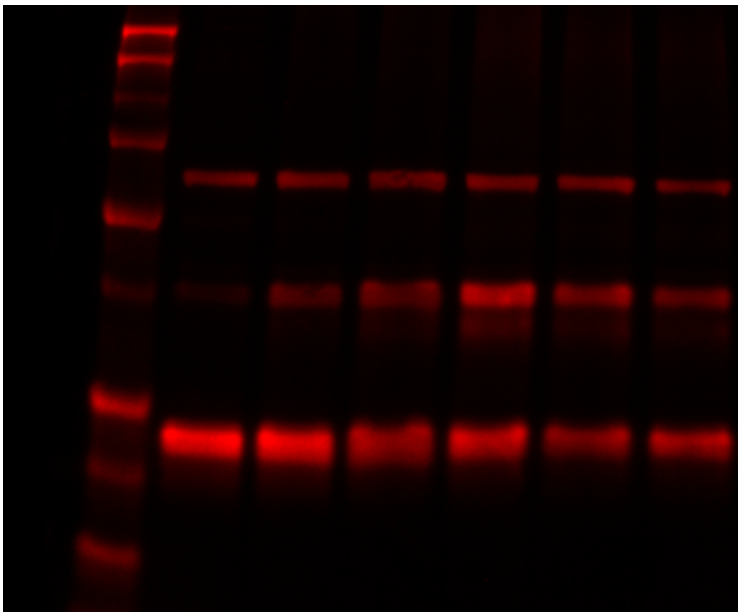

*Figure 3.33: Full Western blot image from Figure 3.5 stained for Prx2 and Hsp60, visualized using IRDye680, showing samples from 1 hr of generation, 0 – 25 mM D-ala (left to right).*

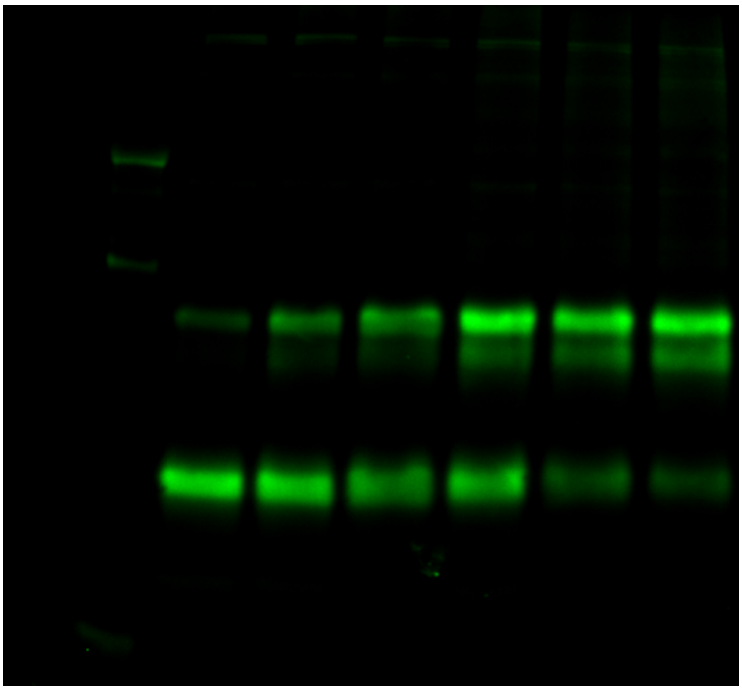

*Figure 3.34: Full Western blot image from Figure 3.5 stained for Prx3, visualized using IRDye800, showing samples from 1 hr of generation, 0 – 25 mM D-ala (left to right)*

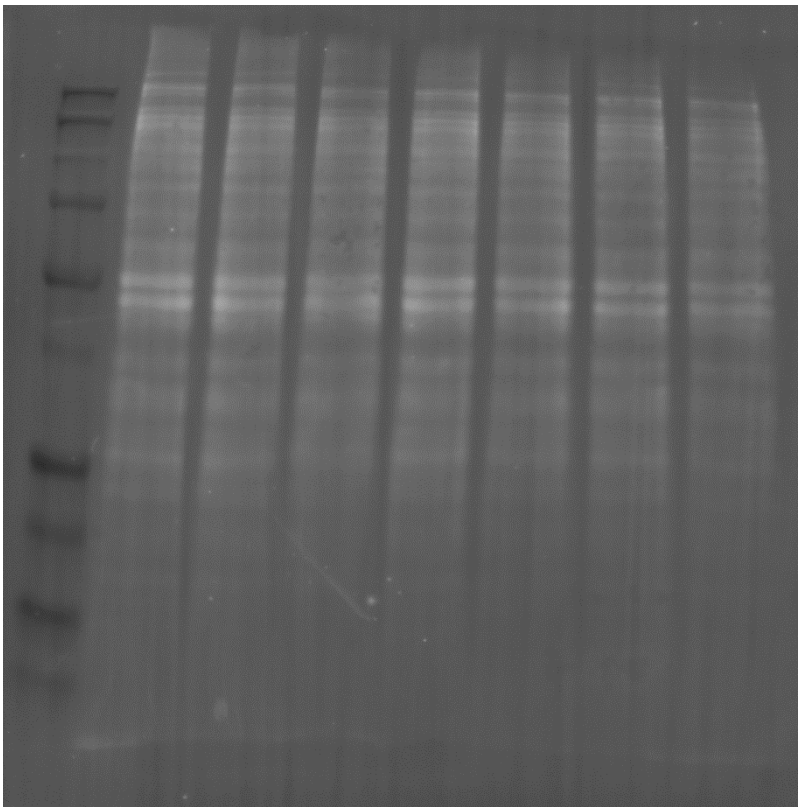

*Figure 3.35: Corresponding stain-free total protein image of 1 hr Western blot*

# Chapter 4 : Using high-throughput techniques to assess drug toxicity in primary patient samples

Pheochromocytoma and paraganglioma are rare but life-threatening cancers. Certain sub-types of these cancers carry succinate dehydrogenase b (SDHB) mutations in Complex II of the mitochondrial electron transport chain, which drive the disease. This mutation may make these tumors susceptible to treatment via a redox-based chemotherapeutic, but the lack of a model system currently makes it difficult to test this hypothesis. A method for using primary patient tumor samples and testing their susceptibility to treatment with a redox-based drug, piperlongumine, while maintaining rigorous statistical power was developed. This method leveraged high-throughput imaging systems and automated image analysis software. Preliminary data indicates that these tumors may be sensitive to piperlongumine.

## 4.1 Introduction

Pheochromocytoma (PCC) are a rare but nonetheless life-threatening type of neuroendocrine cancer that typically carries a poor prognosis [1]. Paraganglioma (PGL) are a related type of cancer that arise from a different type of cell in the nervous system [1]. Both cancers can be driven by a germline mutation in the electron transport chain (ETC), specifically in a defect in succinate dehydrogenase b (SDHB) of complex II in the mitochondria [2–4]. Gastrointestinal stromal tumors (GIST) are an additional type of tumor than can arise in patients with PGL, and neither type can be cured [5]. A present difficulty in studying these cancers is the lack of representative model cell lines/tumor systems. PC3 cells are commonly used as a proxy, but these do not fully recapitulate the disease [3,5].

Because of the deficiency in the ETC, it has been hypothesized that hypoxia may play an important role in the progression of PCC and PGL tumors [6,7]. The hypoxia-inducible factor (HIF) proteins, HIF-1α and HIF-2α have both been investigated as possible key players in the tumors'

metabolism [6,8,9]. The aberrant nature of the ETC complex II in this cancer coupled with the possible change in oxygen usage/dependency led us to wonder how these changes may have altered hydrogen peroxide ($H_2O_2$) flux through the mitochondria, and ultimately, if these cancers would be susceptible to treatment via a redox-based chemotherapeutic. We had previously demonstrated that piperlongumine (PL), an investigational therapeutic, exerted its toxic effects by a $H_2O_2$-dependent mechanism [10]. Early studies have demonstrated that PL may effective in these cell types [11]. Additionally, when performing a meta-analysis in The Cancer Proteome Atlas (TCPA) provided by MD Anderson Cancer Center, peroxiredoxin-1 (Prx1) came up as a "hit" for PCC with SDHB mutations, implying that there may be some kind of redox-related mechanism at play [12,13].

In these experiments, we sought to create a methodology for finding dose-response curves to PL or similar redox-based chemotherapeutics in primary patient samples. Our constraints in this system were primarily a lack of cells, so our main optimization objective was to split up a single sample into multiple dose and replicates to maximize the statistical power. We leveraged the availability of high-throughput imaging systems, as well as software that automatically processes images. We used this to gain some preliminary insight into the susceptibility of these tumor types to treatment by PL.

## 4.2 Materials and methods

*4.2.1 : Cell Culture*

Primary patient cells biopsied from pheochromocytoma (PCC), paraganglioma (PGL), or gastrointestinal stromal tumors (GIST) were provided by the group of Dr. Arthur Tischler at Tufts Medical Center. Cells were counted to estimate the total cell count in the sample so that it could be subdivided among the experimental conditions, which worked out to approximately $10^4$ cells/well. The cells were seeded onto Corning CellBind 96-well plates, and evenly divided among

9 doses and 4 replicates. Cells were dosed with piperlongumine (PL) for 48 hrs, and then fixed with 4% paraformaldehyde.

*4.2.2 : Cell staining and labeling*

Post-fixation, cells were permeabilized with 0.1% Triton X-100, and then labeled with DAPI to stain nuclei. PCC and PGL were also stained with an antibody against tyrosine hydroxylase (TH) to differentiate cancer cells from the surrounding epithelial cells. For some assays, cells were additionally stained with an antibody specific for S-glutathionylated proteins.

*4.2.3 : Cell imaging and post-processing*

Fixed and stained 96-well plates were imaged at the High-Throughput Screening core facility at the MIT Koch Institute at 5x or 10x magnification using the DAPI filter set for auto-focusing. The TRITC filter set was used to visualize the TH label, and where applicable, the FITC filter set was used to visualize protein S-glutathionylation. Images were exported to CellProfiler (Broad Institute) for post-processing. A custom image analysis pipeline was designed to determine the toxicity of each dose of PL based on absolute cell counts. The object identification functions of the software were used to automatically identify nuclei in each field of view, with filtering in place to avoid identifying large debris as a cell nucleus. Where additional stains were used, object identification was used to count and co-localize nuclei with stains in other channels.

## 4.3 Results and Discussion

Primary tumor samples contained a mix of cancer cells and surrounding non-cancer cells. As such, they could potentially provide insight into any toxicity differences between cancerous and non-cancerous cells when exposed to a redox-based chemotherapeutic like PL. Because data regarding both types of cells may have been interesting, dose-response curves for both cell types in PGL samples were created. An example is shown in Figure 4.1. Cancer cells were assumed to be any nuclei that co-localized with the TH stain, and all other nuclei were assumed to be non-

cancer cells. Toxicity was assessed by changes in cell count from the control. Both cancer and non-cancer cells demonstrated a significant decrease in cell count over the dose range tested, as evaluated by one-way ANOVA at the 95% confidence level. In post-hoc testing, however, no single dose showed a statistically significant decrease in cell number from the control for the non-cancer cells at the 95% confidence level (Figure 4.3). For the cancer cells, on the other, all doses starting at 6.3 µM were statistically different from the control at the 95% confidence level (Figure 4.2). This suggests that while overall trends in both cell types exist, individual differences between the dosed and un-dosed cells are stronger in the cancer cells. More experiments beyond these preliminary data will test whether this difference between cancer and non-cancer cells is real or an artifact.

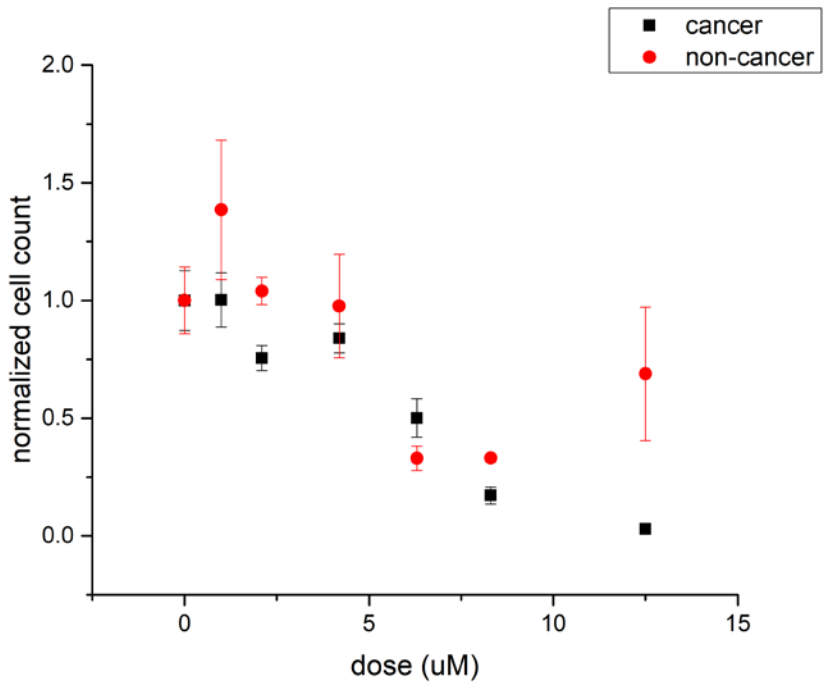


*Figure 4.1: Dose-response curve of PGL to PL doses. Points represent the mean ± SEM.*

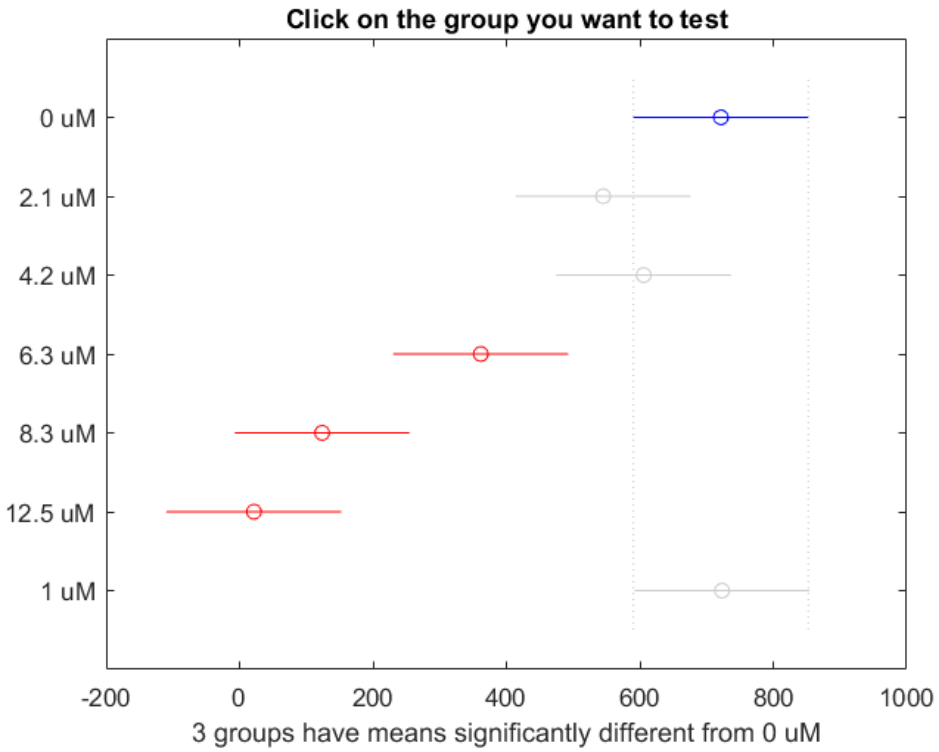


*Figure 4.2: Results of Tukey HSD post-hoc test for cancer cells from PGL primary tumor samples dosed with PL. Blue represents the mean that other samples were compared to (the control), grey represents non-statistically significant samples, and red represents samples that were found to be statistically different at the 95% confidence level.*

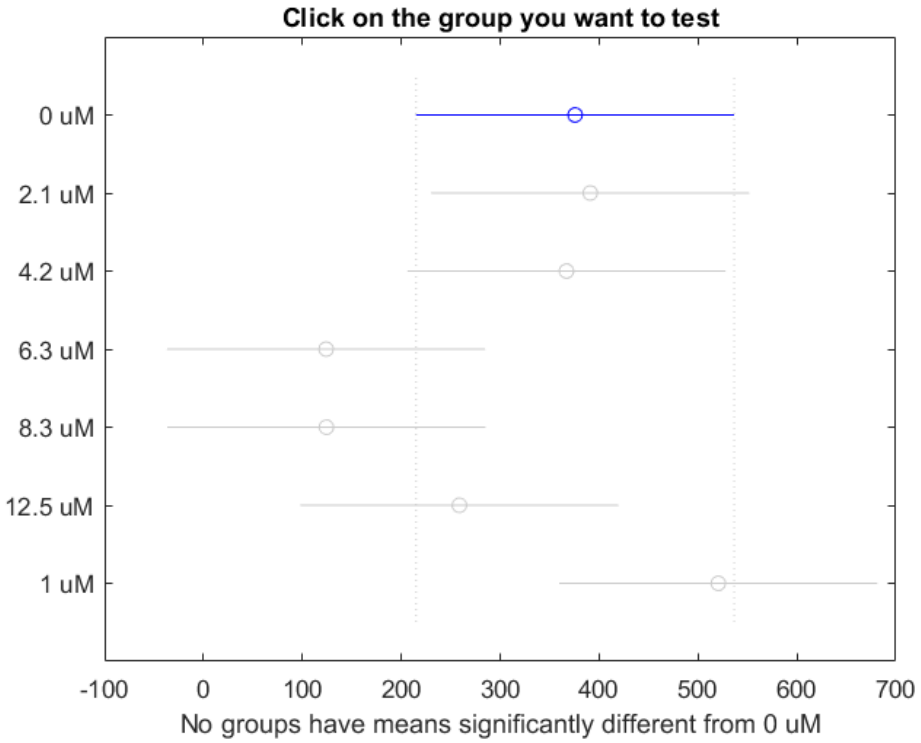


*Figure 4.3: Results of Tukey HSD post-hoc test for non-cancer cells from PGL primary tumor sample dosed with PL. Blue represents the mean that other samples were compared to (the control) and grey represents non-significant samples at the 95% confidence level.*

GIST cells were cultured in such a way as to not be a mixed cell population, so it was unnecessary to stain them for TH to differentiate them from surrounding non-cancer cells. In this case, the co-localization algorithm was not required, and only nucleus counts were performed. The results of from one of these experiments is shown in Figure 4.4. The shape of this curve is quite different from the one in Figure 4.1, and demonstrates a sharp drop-off in cell count after 4.2 µM. The trend was found to be significant at the 95% confidence level by one-way ANOVA, and the results of post-hoc testing are shown in Figure 4.5. Consistent with the sharp drop seen in the plot of cell counts, doses of 6.3 µM and higher were found to differ significantly from the control at the 95% confidence level.

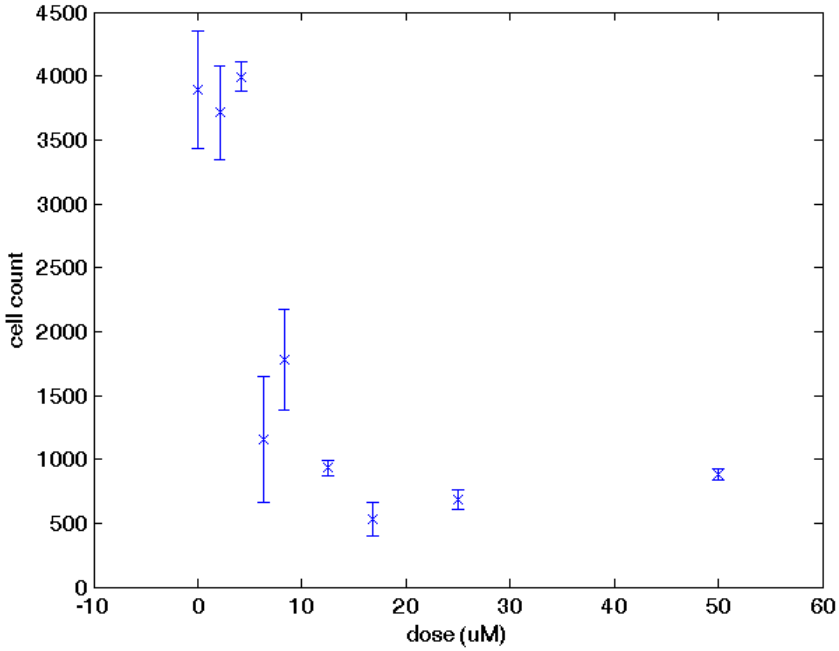


*Figure 4.4: Dose-response curve of GIST cells treated with PL. Points represent mean ± SEM.*

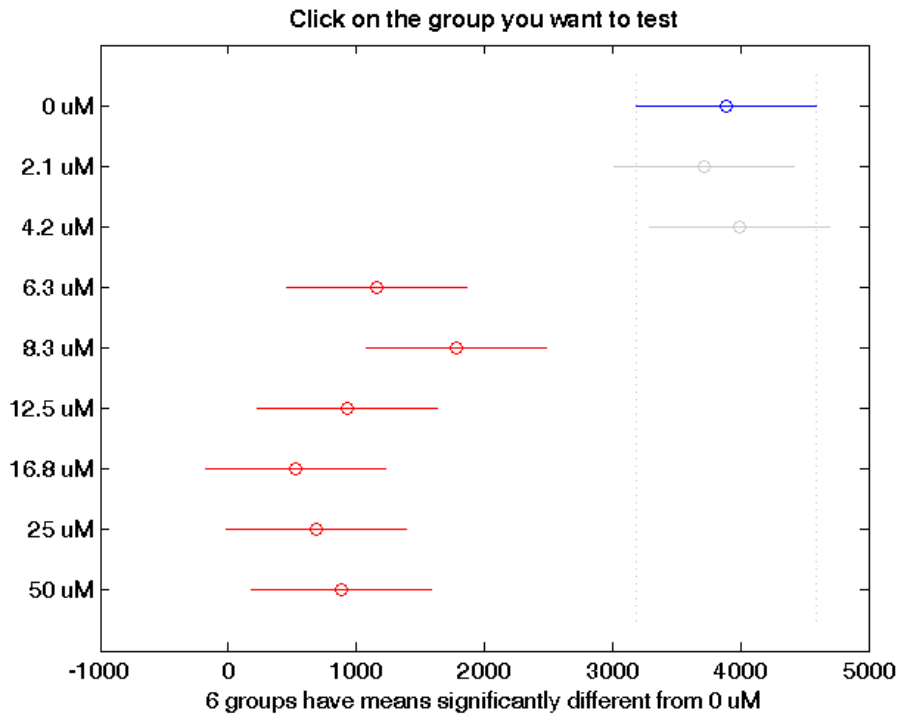


*Figure 4.5: Results of Tukey HSD post-hoc test for cancer cells from GIST samples dosed with PL. Blue represents the mean that other samples were compared to (the control), grey represents non-statistically significant samples, and red represents samples that were found to be statistically different at the 95% confidence level.*

Protein S-glutathionylation was initially thought to be quantifiable via this methodology. It had been previously found to be an interesting part of the PL mechanism. PL produced proteins whose disulfide bond to GSH could not be reduced [10]. The way this had been previously determined was by comparing the staining pattern produced by an antibody against S-glutathionylated proteins with the fluorescence produced by a kit that relied on that disulfide bond being reduced. However, early attempts to implement all the steps the chemistry of the kit required resulted in the cells washing off the plate, despite centrifuging between steps and gentle handling. Future attempts to understand these post-translational modifications will require careful optimization, and may benefit from robotic liquid handling systems.

The PGL and GIST initial data show some promise that PL may be an effective therapeutic in these tumor types. Some additional preliminary data for PCC is shown in the Appendix. More broadly, the methodology applied here provided a framework to be able to study these non-model systems with some amount of statistical rigor. By taking advantage of high-throughput systems microscopy systems and automated image processing pipelines, we are able to capture a lot more information from cells sourced from the same donor, rather than adding an additional confounding variable of patient-to-patient heterogeneity within a dose-response curve. This methodology could be extended to any cancer system where model cell lines are not currently available but patients biopsies are.

## 4.4 References


(1) DeLellis, R. A. *Tumours of Endocrine Organs*; IARC Press, 2004.

(2) Yang, C.; Matro, J. C.; Huntoon, K. M.; Ye, D. Y.; Huynh, T. T.; Fliedner, S. M. J.; Breza, J.; Zhuang, Z.; Pacak, K. Missense Mutations in the Human SDHB Gene Increase Protein Degradation without Altering Intrinsic Enzymatic Function. *FASEB J.* **2012**, *26* (11), 4506–4516.

(3) Chae, Y. C.; Angelin, A.; Lisanti, S.; Kossenkov, A. V; Speicher, K. D.; Wang, H.; Powers, J. F.; Tischler, A. S.; Pacak, K.; Fliedner, S.; et al. Landscape of the Mitochondrial Hsp90 Metabolome in Tumours. *Nat. Commun.* **2013**, *4*, 2139.

(4) van Nederveen, F. H.; Gaal, J.; Favier, J.; Korpershoek, E.; Oldenburg, R. A.; de Bruyn, E. M.; Sleddens, H. F.; Derkx, P.; Rivière, J.; Dannenberg, H.; et al. An Immunohistochemical Procedure to Detect Patients with Paraganglioma and Phaeochromocytoma with Germline SDHB, SDHC, or SDHD Gene Mutations: A Retrospective and Prospective Analysis. *Lancet Oncol.* **2009**, *10* (8), 764–771.
(5) Powers, J. F.; Cochran, B.; Baleja, J. D.; Sikes, H. D.; Zhang, X.; Lomakin, I.; Langford, T.; Stein, K. T.; Tischler, A. S. A Unique Model for SDH-Deficient GIST: An Endocrine-Related Cancer. *Endocr. Relat. Cancer* **2018**, *25* (11), 943–954.
(6) Tella, S. H.; Taïeb, D.; Pacak, K. HIF-2alpha: Achilles' Heel of Pseudohypoxic Subtype Paraganglioma and Other Related Conditions. *Eur. J. Cancer* **2017**, *86*, 1–4.
(7) Keith, B.; Johnson, R. S.; Simon, M. C. HIF1α and HIF2α: Sibling Rivalry in Hypoxic Tumour Growth and Progression. *Nat. Rev. Cancer* **2011**, *12* (1), 9–22.
(8) Favier, J.; Amar, L.; Gimenez-Roqueplo, A. P. Paraganglioma and Phaeochromocytoma: From Genetics to Personalized Medicine. *Nat. Rev. Endocrinol.* **2015**, *11* (2), 101–111.
(9) Gimenez-Roqueplo, A.-P.; Favier, J.; Rustin, P.; Rieubland, C.; Crespin, M.; Kien, P. K. Van; Corvol, P. Mutations in the SDHB Gene Are Associated with Extra-Adrenal and / or Malignant Phaeochromocytomas Mutations. *Cancer Res.* **2003**, *63*, 5615–5621.
(10) Huang, B. K.; Langford, T. F.; Sikes, H. D. Using Sensors and Generators of H2O2 to Elucidate the Toxicity Mechanism of Piperlongumine and Phenethyl Isothiocyanate. *Antioxid. Redox Signal.* **2016**, *24* (16), 924–938.
(11) Bullova, P.; Cougnoux, A.; Abunimer, L.; Kopacek, J.; Pacak, K. Hypoxia Potentiates the Cytotoxic Effect of Piperlongumine in Pheochromocytoma Models. *Oncotarget* **2016**, *7* (26).
(12) Li, J.; Lu, Y.; Akbani, R.; Ju, Z.; Roebuck, P. L.; Liu, W.; Yang, J.-Y.; Broom, B. M.; Verhaak, R. G. W.; Kane, D. W.; et al. TCPA: A Resource for Cancer Functional Proteomics Data. *Nat. Methods* **2013**, *10* (11), 1046–1047.
(13) Li, J.; Akbani, R.; Zhao, W.; Lu, Y.; Weinstein, J. N.; Mills, G. B.; Liang, H. Explore, Visualize, and Analyze Functional Cancer Proteomic Data Using the Cancer Proteome Atlas. *Cancer Res.* **2017**, *77* (21), e51–e54.

## 4.5 Appendix

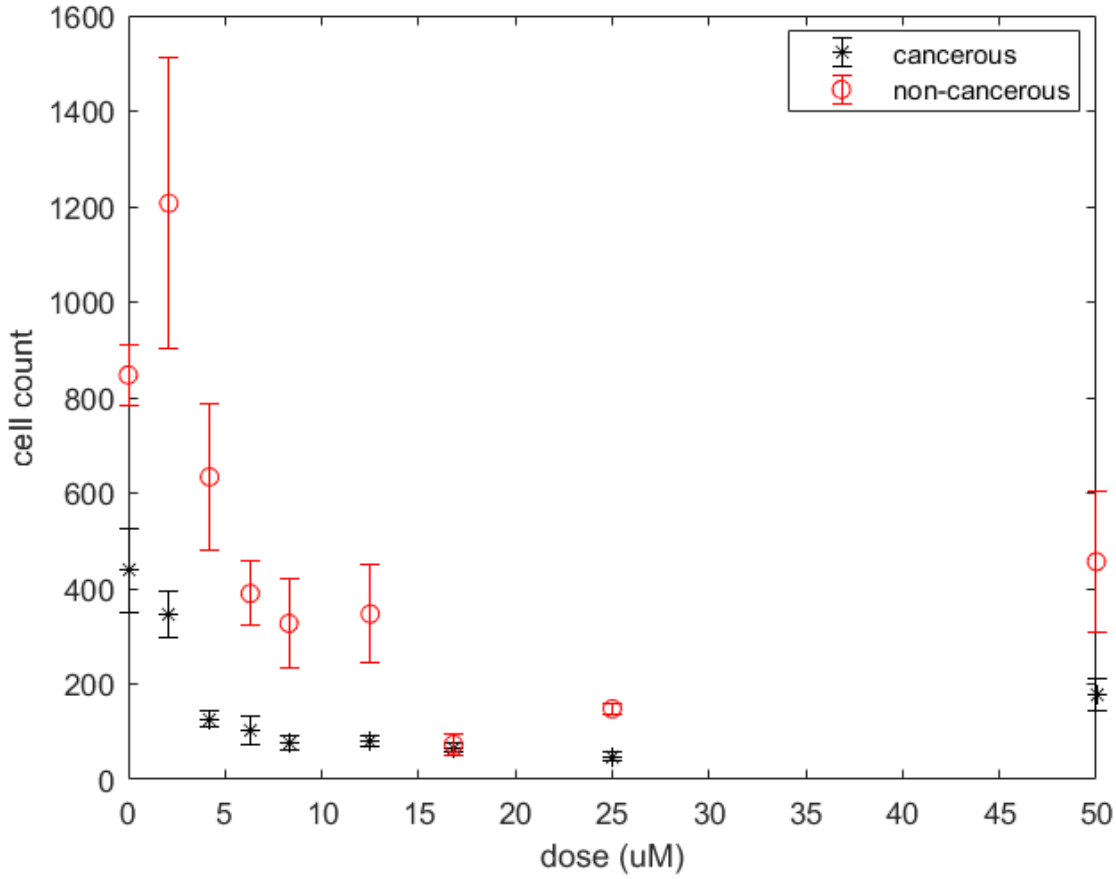


*Figure 4.6: Dose-response of primary PCC samples dosed with PL. Points represent mean ± SEM.*

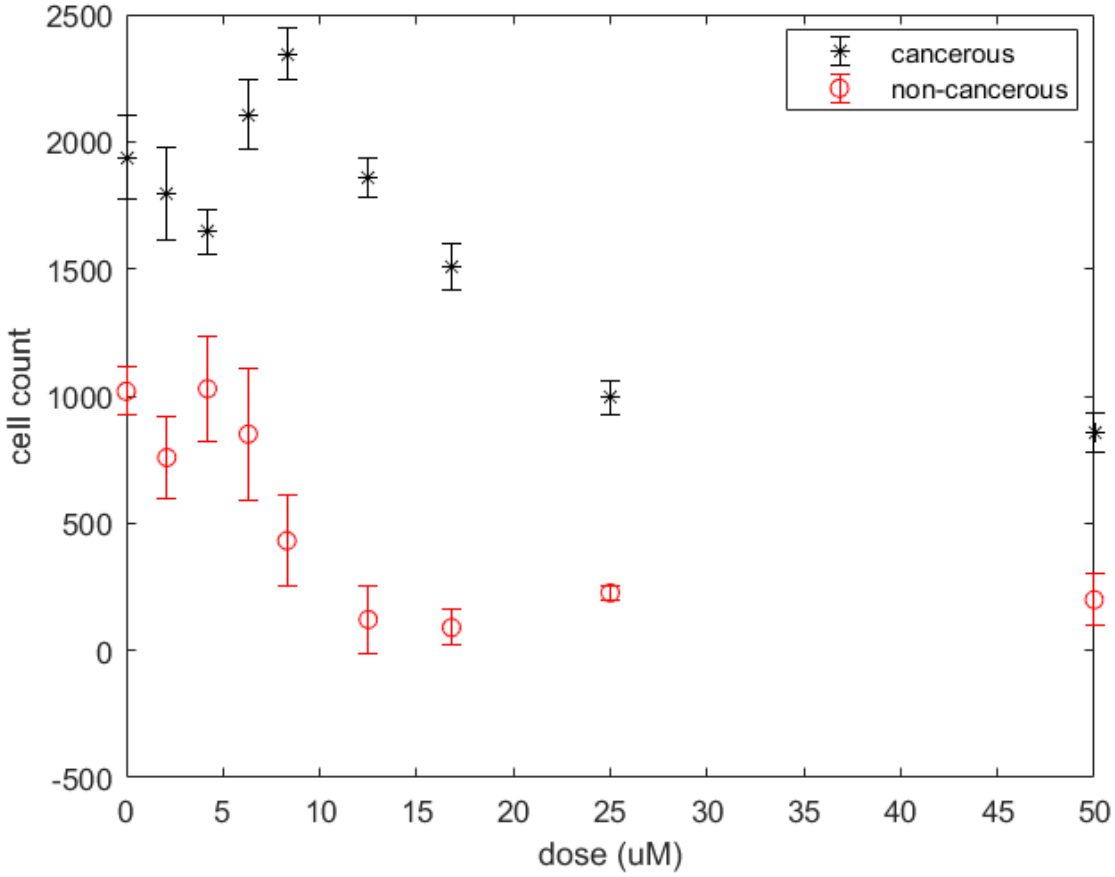


*Figure 4.7: Dose-response curve of primary PCC samples dosed with PL. Points represent mean ± SEM.*

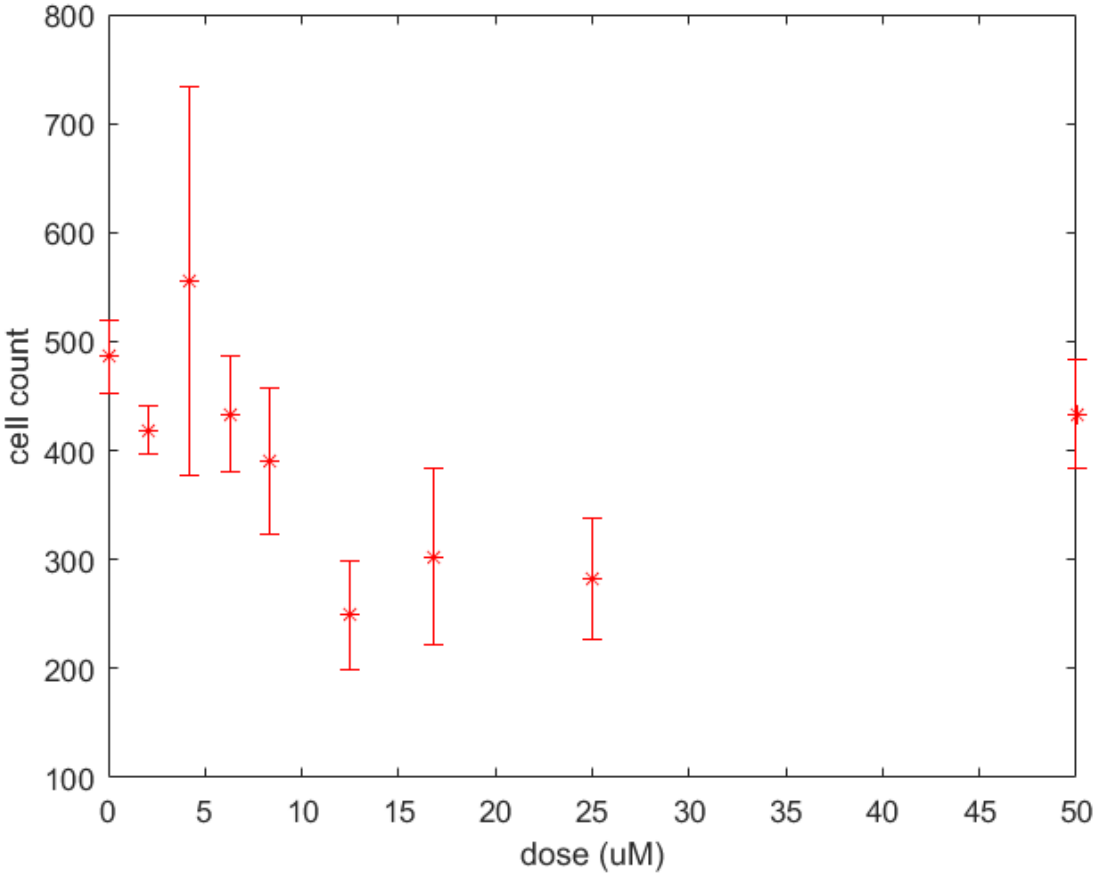


*Figure 4.8: Dose-response of GIST cells grown in normoxia rather than hypoxia. Points represent mean ± SEM.*

*Table 4.1: Dose-response (raw and normalized) of cancer and non-cancerous cells in primary PGL samples to PL*

| Dose (µM) | Cancer cell count | Non-cancer cell count | Normalized cancer cell count | Normalized non-cancer cell count |
|---|---|---|---|---|
| 0 | 187±27 | 910±117 | 1±0.14 | 1±0.13 |
| 1 | 178±37 | 1066±139 | 0.95±0.20 | 1.17±0.15 |
| 2.1 | 161±11 | 776±40 | 0.86±0.05 | 0.85±0.04 |
| 4.2 | 175±17 | 798±101 | 0.93±0.09 | 0.88±0.11 |
| 6.3 | 110±17 | 376±31 | 0.59±0.09 | 0.41±0.03 |
| 8.3 | 45±7 | 203±20 | 0.24±0.04 | 0.22±0.02 |
| 12.5 | 11±4 | 269±110 | 0.06±0.02 | 0.30±0.12 |

*Table 4.2: Dose-response (raw and normalized) of cancer and non-cancerous cells in primary PCC samples to PL*

| Dose (µM) | cancer | SEM | non-cancer | SEM | Normalized cancer | SEM | Normalized non-cancer | SEM |
|---|---|---|---|---|---|---|---|---|
| 0 | 1938.5 | 163.7999 | 1018.5 | 94.71404 | 1 | 0.084498 | 1 | 0.092994 |
| 2.1 | 1796.5 | 183.5381 | 758.5 | 164.2024 | 0.926747 | 0.09468 | 0.744723 | 0.16122 |
| 4.2 | 1645.5 | 90.18361 | 1028.5 | 205.7403 | 0.848852 | 0.046522 | 1.009818 | 0.202003 |
| 6.3 | 2106.5 | 137.7755 | 850.25 | 257.4883 | 1.086665 | 0.071073 | 0.834806 | 0.252811 |
| 8.3 | 2344.25 | 99.79761 | 431.25 | 181.0301 | 1.209311 | 0.051482 | 0.423417 | 0.177742 |
| 12.5 | 1859 | 74.11365 | 121.25 | 135.2432 | 0.958989 | 0.038232 | 0.119048 | 0.132787 |
| 16.8 | 1508.25 | 93.4241 | 89.75 | 70.14435 | 0.77805 | 0.048194 | 0.08812 | 0.06887 |
| 25 | 996 | 66.4718 | 226.25 | 27.59642 | 0.513799 | 0.03429 | 0.22214 | 0.027095 |
| 50 | 855.75 | 79.92953 | 199.25 | 101.2179 | 0.44145 | 0.041233 | 0.195631 | 0.099379 |

# Chapter 5 : Using Computational Methods to Analyze the Structure of 2-Cys Peroxiredoxins

Peroxiredoxins are remarkably conserved across all kingdoms of life and through evolutionary time. Their catalytic mechanism involves a conformational change across the length of the protein, from the peroxidatic to the resolving cysteine, in order for a disulfide bond to form. To better understand the allosteric mechanisms involved in dimer formation and protein-protein interactions, statistical coupling analysis (SCA) was performed to elucidate evolutionarily conserved clusters of residues within the peroxiredoxin-2 (Prx2) and peroxiredoxin-1 (Prx1) sub-families of proteins. Eigenvalue decomposition of the correlation matrices was used to analyze protein sectors. Prx2 was found to have four evolutionarily conserved clusters, and Prx1 was found to have three, with each protein demonstrating evidence of distinct protein sectors. These data can be used to better understand the structure-function relationships in Prx2 and Prx1.

## 5.1 Introduction

The peroxiredoxin (Prx) protein family in mammals is part of a large protein group, conserved across kingdoms, known as thiol-specific antioxidants (TSAs) or sometimes called the thioredoxin (Trx) superfamily. What is most notable about TSAs is their very high reaction rate with hydrogen peroxide ($H_2O_2$) compared to a typical protein thiol: ~$10^8$ vs. ~$10^{1}$ [1–3]. Contributing to this large kinetic difference is the microenvironment created by the protein structure around the catalytic (or peroxidatic, $C_P$) and resolving ($C_R$) cysteines [4]. In the most common type of $H_2O_2$ detoxification reaction, the TSA protein converts from a fully folded (FF) conformation to a locally unfolded (LU) conformation after $H_2O_2$ reacts with $C_P$ [5]. This enables the reaction between $C_P$ on one monomer with $C_R$ on the opposite monomer, completing the formation of a disulfide bond and a head-to-tail dimer [6].

Based on the conformational change necessary for the mechanism of action of these proteins and the presence of these proteins in all kingdoms of life, it is expected that there exists a conserved structural relationship within Prxs that goes beyond the simple conservation of $C_P$ and $C_R$. Additionally, new data are emerging that suggest the existence of protein-protein interaction sites on Prx2 and Prx1 [7,8]. These sites could help explain the mechanism and kinetics of the putative redox relay that has recently been proposed, which posits that proteins which are easily oxidized, like Prx2, "transfer" their disulfides to protein thiols whose oxidation is kinetically unfavorable [7,9]. As an experimental approach to an exhaustive structural analysis is infeasible, a computational strategy was employed to investigate the allosteric mechanisms behind Prx catalysis as well as the existence of possible protein sectors. Statistical Coupling Analysis (SCA) applies the experimental strategy of making point mutations to proteins and measuring whether the protein retains function, but in a computational format. By using the "experiments" already performed by nature through evolution, a library of protein sequences can be used to demonstrate how mutations correlate with each other.

The focus of this work is two members of the Trx superfamily: peroxiredoxin-2 (Prx2) and peroxiredoxin-1 (Prx1). Each of these forms a homodimer; dimer formation is central to its catalytic activity. Clusters of residues identified by SCA could indicate how allosteric interactions are mediated across the protein dimers or within the monomers themselves. They could also point to structural features that support protein-protein interactions.

## 5.2 Methods

*5.2.1 : Creating a library of protein sequences*

Human peroxiredoxin-2 (PRDX2, accession number P32119), human peroxiredoxin-1 (PRDX1, accession number Q06830), and a truncated peptide from an unpublished crystal

structure provided by the lab of Todd Lowther were used to seed a PSI-BLAST search to identify proteins with >65% identity. The following were excluded from the search: synthetic DNA/organisms, predicted/putative/hypothetical structures, and unknown proteins. The top hits were selected to perform a multiple sequence alignment (MSA) and subsequent analysis. Libraries were selected to have at least 500 sequences.

*5.2.2 : Multiple Sequence Alignment*

MSA was performed on the protein libraries that each PSI-BLAST search outputted using Clustal Omega. The alignment was performed on the whole sequences, ensuring that the first sequence in the alignment was the sequence used to seed the PSI-BLAST search (PRDX2, PRDX1, and the peptide sequence, respectively). After the alignment, the sequences were truncated to match the length of a single monomer of Prx, where applicable.

*5.2.3 : Statistical Coupling Analysis*

The Ranganathan laboratory has made available a MATLAB code for the execution of SCA, the clustering of residues based on the results of SCA, and the generation of corresponding figures. For more specific methodology regarding SCA, please see Suel *et al* [10]. For protein structure reference, Prx2 results were compared to the published crustal structure 1QMV [11] and Prx1 results were compared to the published crystal structure 2RII [12].

## 5.3 Results and Discussion

*5.3.1 : Validation of Statistical Coupling Analysis Approach*

For SCA to work best, the sequence library must be both conserved and flexible, because without a variety of sequences, it is difficult to determine how one residue responds to a change in another. In Figure 5.1, it is demonstrated that for both Prx2 and Prx1, the sequence libraries have sufficient diversity. As seen in the histograms in Figure 5.1a – b, most of the distribution in these libraries falls between 50 – 70% conserved sequence identity, with a tail above 70%. This indicates

that both alignments are comprised of a mostly diverse group of sequences, with a smaller group of very similar sequences. The matrix plots in Figure 5.1c – d displays these results as clusters. Both Prx2 and Prx1 show a small cluster of high pairwise sequence identity, demonstrated by the red clusters in the top left of both matrices, but this cluster appears larger for Prx1. A second, more diffuse cluster appears in both matrices as well, depicting the group of sequences that fall in the middle ranges of pairwise sequence identity.

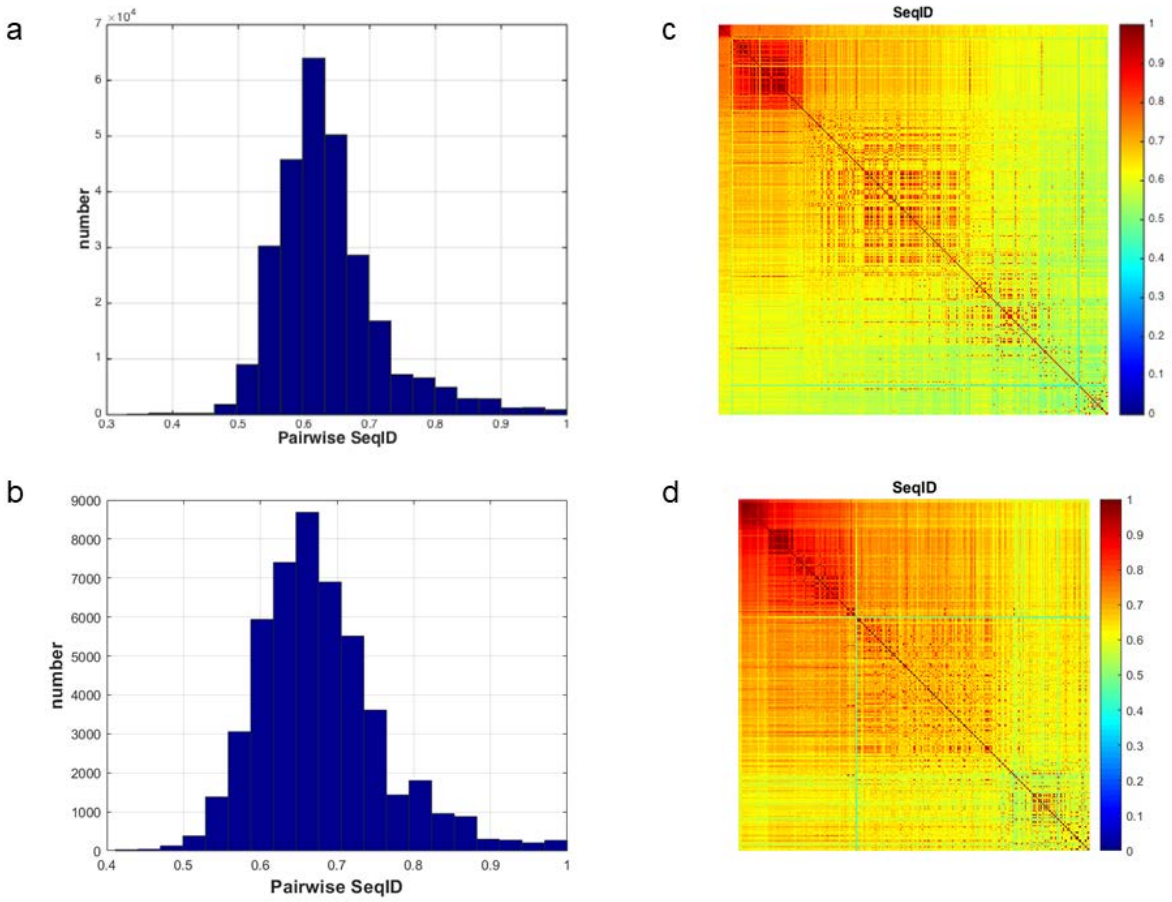


*Figure 5.1: Sequence correlation. Histogram of the mean pairwise identity distribution for a) PRX2 sequences and b) Prx1 sequences. Both histograms are relatively normally distributed, with a tail towards higher values. Sequence similarity matrix for c) PRX2 and d) Prx1, with red indicating the highest degree of similarity and blue indicating no similarity.*

The positional conservation results further support a moderate degree of conservation across sequences. Figure 5.2 indicates that the individual conservation scores for PRDX2 and Prx1 show a similar distribution, and that most of them fall between 1.5 and 3; only a small number

have a very high score (D>4). This suggests that only a few residues are very highly conserved, and are likely the ones essential for protein function. For instance, the peroxidatic and resolving cysteines ($S_P$ and $S_R$) of both Prx2 and Prx1 stand out as very highly conserved.

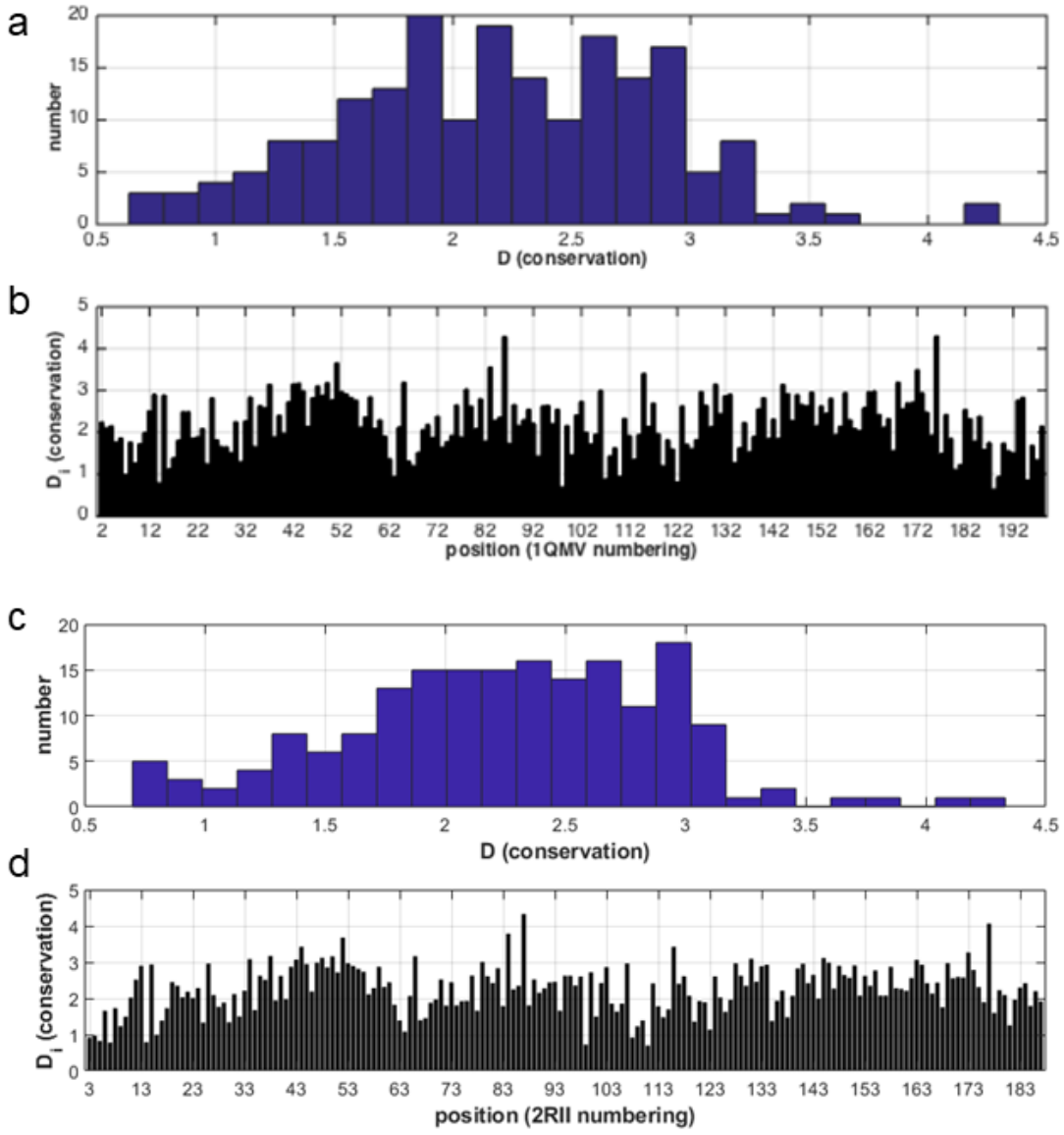


*Figure 5.2: Positional conservation. Histogram of positional conservation scores (D) calculated for each residue in a) Prx2 and c) Prx1. Bar graph of the degree of conservation at each residue in b) Prx2 and d) Prx1.*

### *5.3.2 : Probing the Mathematical Structure of SCA Results*

To search for patterns in protein structure coevolution, an eigenvalue decomposition was performed on the SCA positional correlation matrix. The eigenvectors here represent a linear

combination of sequence positions, with the eigenvalue assigning statistical importance. To verify which eigenvectors are statistically significant rather than the result of finite sampling, the eigenvectors of the positional correlation matrix were compared to the eigenvectors of the scrambled alignment. Figure 5.3a – b demonstrates that up to six eigenmodes are statistically significant for both the Prx2 and Prx1 sequence families. The top three eigenmodes are further explored here. Figure 5.3c – d depicts 3D plots of these eigenmodes for Prx2 and Prx1. Patterns, as opposed to random scatter or all points grouped at the origin, suggest different sectors in the protein. The three branches in Figure 5.3c suggests that there are different sectors of coevolution in the Prx2 family of proteins; a similar pattern can be observed for Prx1 in Figure 5.3d. Figure 5.4 depicts 2D representations of the top eigenmodes for both protein families. The scatter of residues from Prx1 in Figure 5.4d – e as opposed to the tighter branching patterned seen in the plots associated with Prx1 in Figure 5.4a – b suggests that the sectors in the Prx2 family are more separate from one another, whereas the structure in Prx1 may be more interrelated.

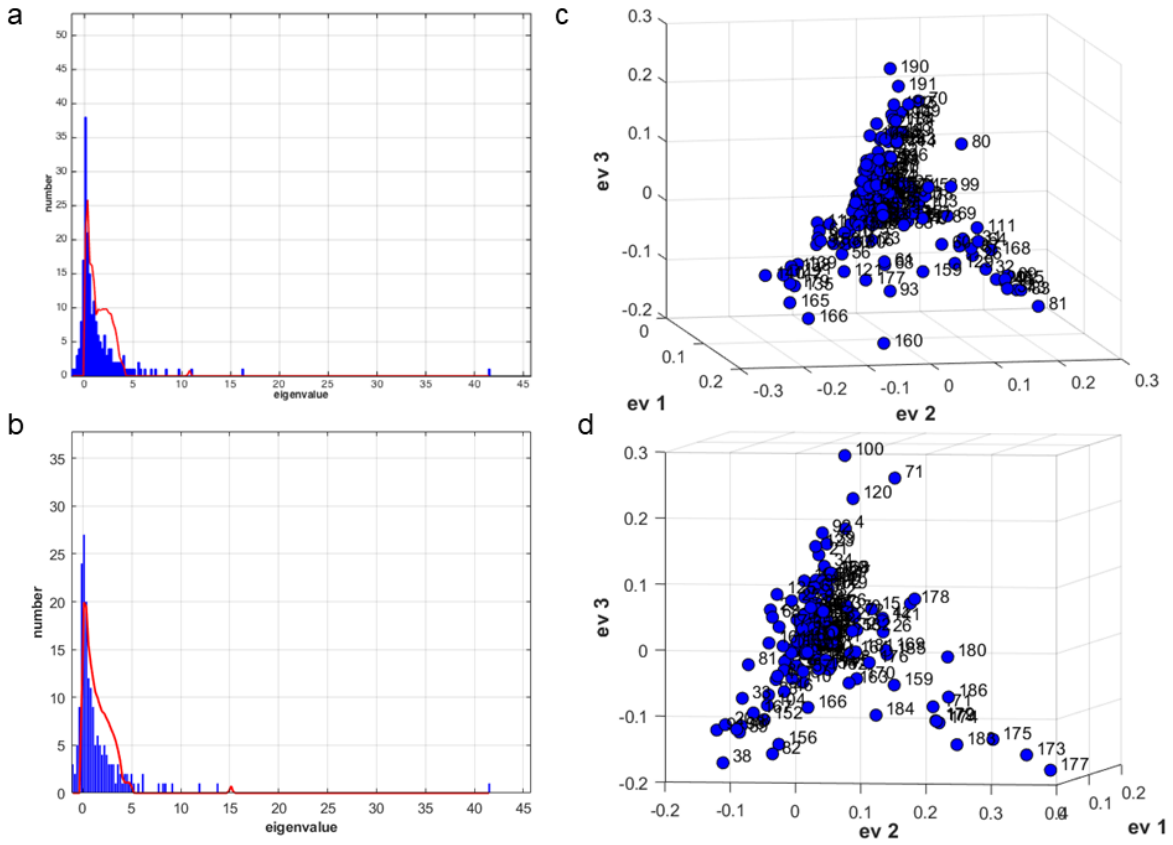


*Figure 5.3: Eigenmodes of the SCA matrix. Red line in a (Prx2) and b (Prx1) depicts the random statistical expectation value of the eigenmodes for each protein family. Blue bars are the actual eigenmodes calculated by eigenvalue decomposition. Bars to the left of the red line are considered statistically significant. In both families, more than three eigenmodes are significant, so only the top three are considered, plotted in c and d for Prx2 and Prx1, respectively. These 3D representations of the eigenmodes suggest the existence of different protein sectors, evidenced by the branches in the plots.*

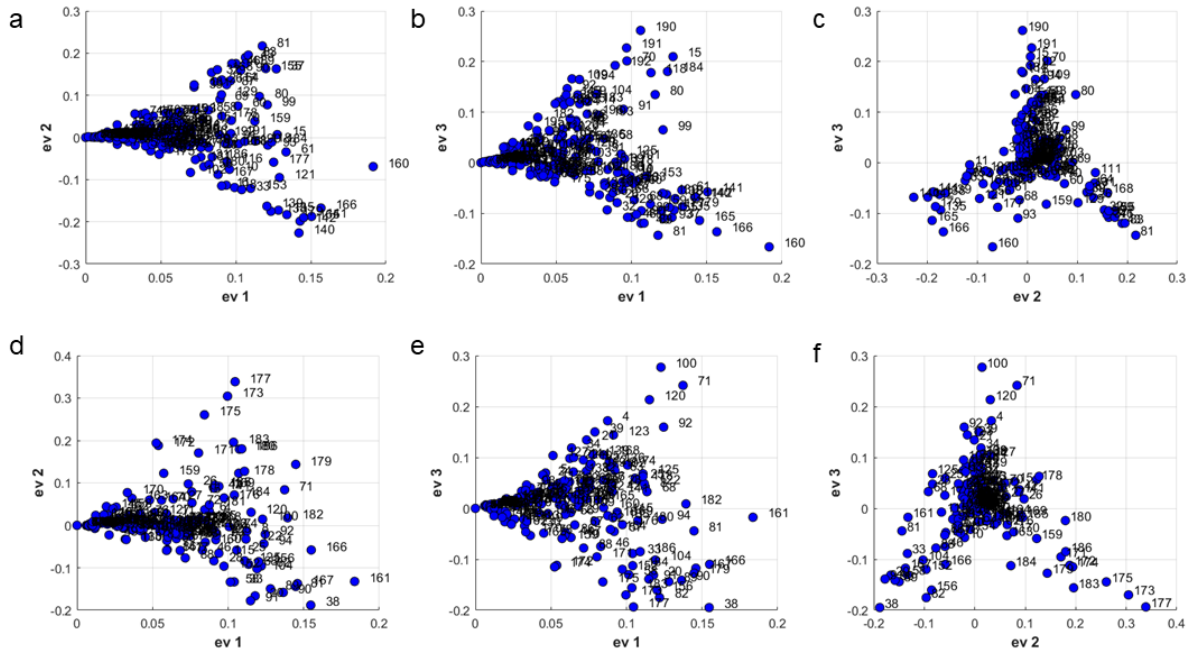


*Figure 5.4: Top Eigenmodes, 2D representation. Plots a – c depict the top three eigenmodes of the positional correlation matrix for Prx2 plotted against each other in 2D. Plots d – g depict the top three eigenmodes of the positional correlation matrix for Prx1 plotted against each other in 2D. These plots imply the existence of different protein sectors, particularly evident in panels c and g.*

Independent component analysis (ICA) further validated the results from the eigenvalue decomposition. ICA performs a singular value decomposition on the eigenvectors of the positional correlation matrix, which maps it to the sequence correlation matrix. Figure 5.5 depicts the 3D plots of the top three independent components of the positional correlation matrices for each Prx2 and Prx1, with corresponding 2D plots in Figure 5.6. In Figure 5.5a, the ICA results for Prx2 display three branches along the three independent components, indicating three groups of evolutionarily correlated sectors, as was implied from the eigenvalue decomposition. From the 2D plots, it can be observed that these sectors are mostly independent from the branching, but that some points contribute about equal weight to multiple sectors (i.e. position 61). In Figure 5.5b, the ICA results for Prx1 show two defined branches and a less defined third branch. Breaking this down into the 2D plots in Figure 5.6d – f, there appear to be two groups of evolutionarily correlated sectors, most clearly depicted by the branching in d, with some scattered residues comprising a

weak possible third sector. This pattern can be further explored by directly comparing the sequence space to the positional correlations, depicted in Figure 5.7. Different patterns emerge for Prx2 and Prx1. By comparing Figure 5.7a and c, the pattern emergence in the sequence space suggests that difference sectors may correspond to phylogenetically distinct subfamilies in the Prx2 family. The same comparison for Prx1 in Figure 5.7b and d is less clear, as the scatter in the sequence space is ambiguous and difficult to interpret.

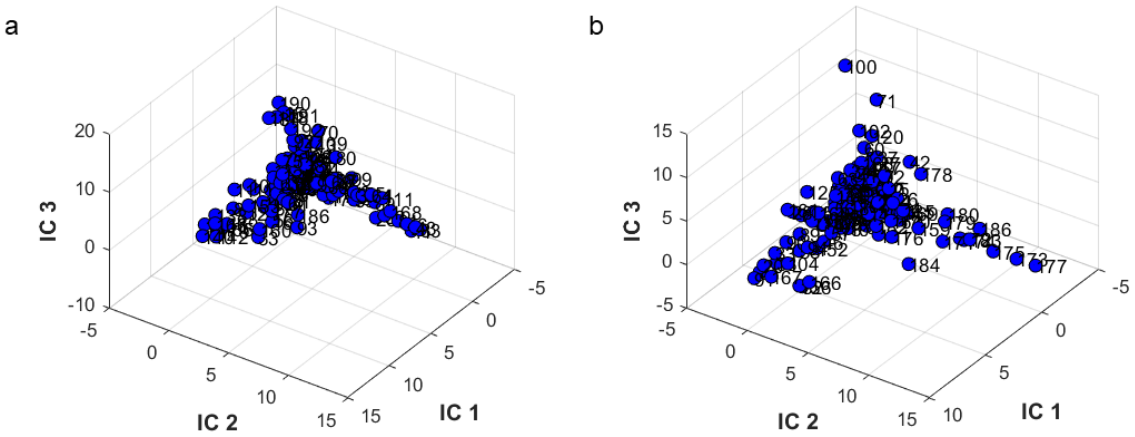


*Figure 5.5: Independent component analysis. The top three independent components of the sequence correlation matrix of a) Prx2 and b) Prx1 were plotted against each other in 3D. Similar to the eigenvalue decomposition, these plots suggest the existence of different protein sectors rather than a single group of related residues.*

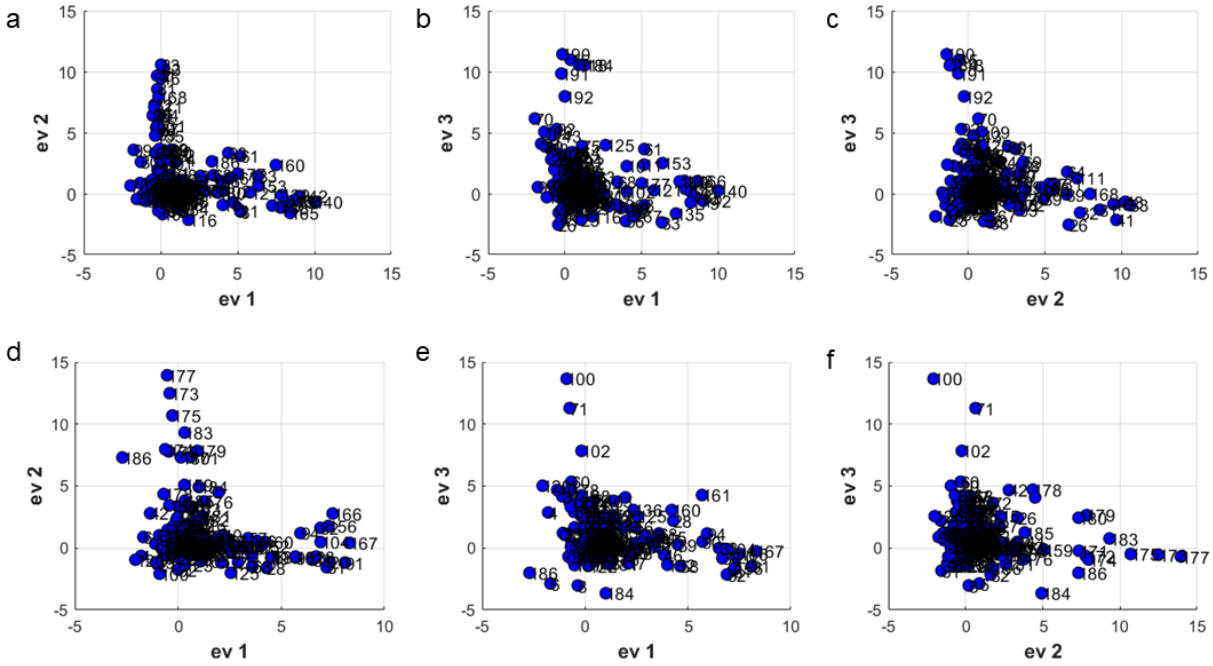


*Figure 5.6: ICA, 2D representation. Plots a – c depict the top three eigenmodes of the sequence correlation matrix for Prx2 plotted against each other in 2D. Plots d – g depict the top three eigenmodes of the sequence correlation matrix for Prx1 plotted against each other in 2D.*

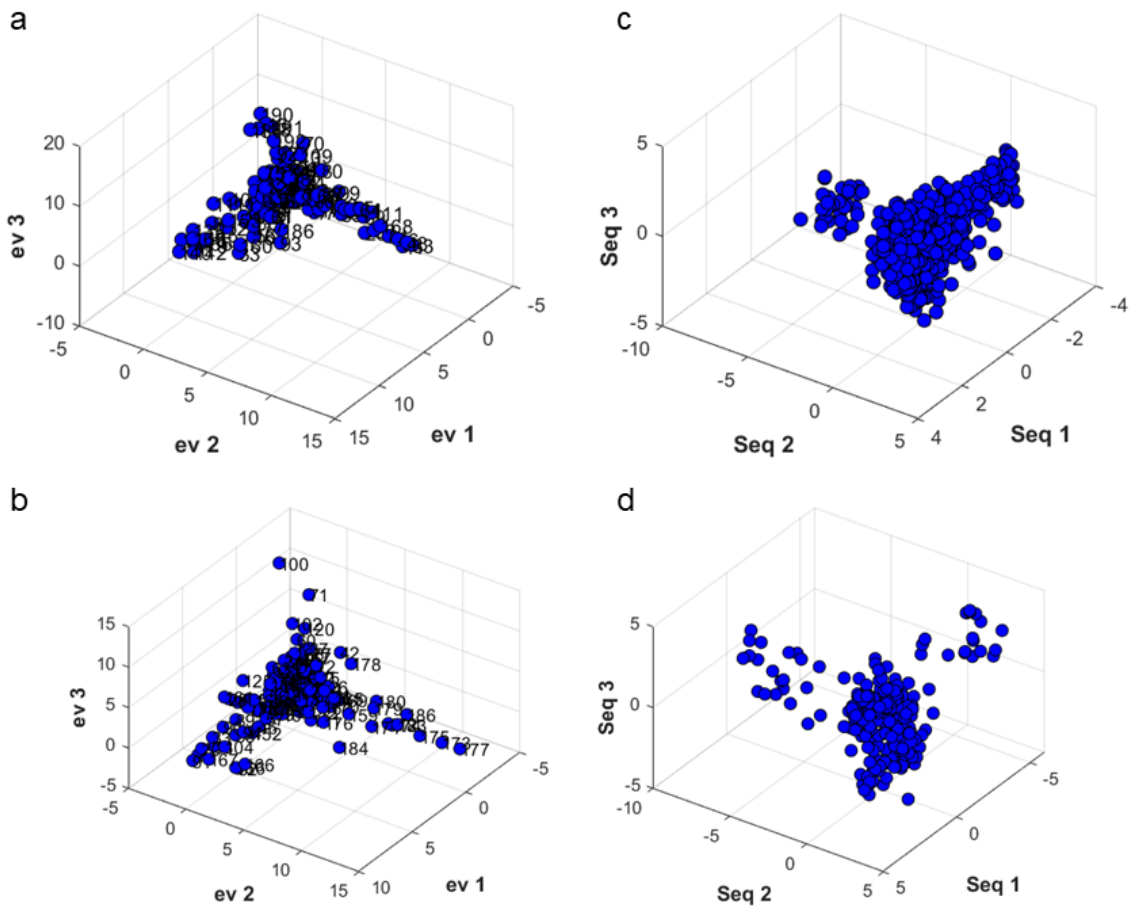


*Figure 5.7: Mapping sequence space by positional correlation. Comparing the pattern in the positional space (left, Prx2 in a and Prx1 in b) with the pattern in the sequence space (right, Prx2 in c and Prx1 in d) may provide information about the evolution of protein sub-families. For Prx2, the pattern in c implies the evolution of phylogenetically distinct sub-families. The pattern in d for Prx1 also appears to imply some evolutionary divergence, though not as clearly as for Prx2.*

### *5.3.3 : Identifying and Understanding Correlated Residue Clusters*

Following eigenvalue analysis, correlation data was used to identify structural relationships in the protein. Figure 5.8 depicts a heatmap of the clustering of residues based on their pairwise correlation. For Prx2, four clusters were identified and for Prx1, three clusters were identified. In choosing groups of interest, some clusters were chosen as a smaller subset of a larger cluster in order to reduce noise and better elucidate the functional features of the group, like Group 1 for Prx2.

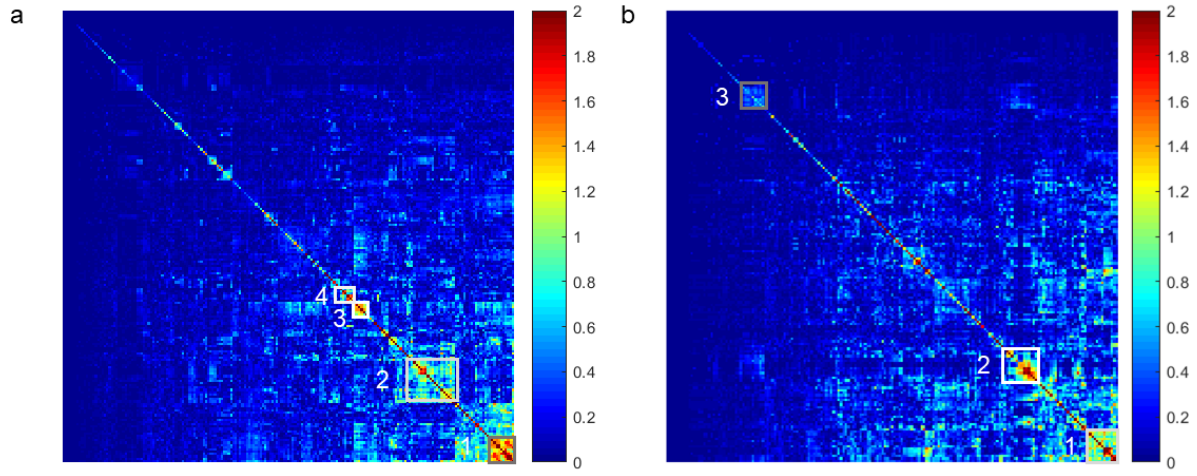


*Figure 5.8: SCA position clustergram. a) Pairwise residue correlations for Prx2, with the four identified clusters outlined and numbered. b) Pairwise residue correlations for Prx1, with the three identified clusters outlined and numbered. Normalized maximum correlation is 2.*

The Prx2 dimer with its $C_P$ and $C_R$ highlighted on each monomer is shown in Figure 5.9. This structure was used to contextualize each cluster identified in Figure 5.8a. Cluster 1 is depicted in Figure 5.10 and has the most visually apparent allosteric mechanism. Its residues span the homodimer interface and also form part of $C_R$'s binding pocket. This suggests a series of cooperative interactions that mediate the conformational changes involved in dimerization. $C_R$ cannot be accessed until the second step of the Prx2 catalytic mechanism, after $C_P$ has been oxidized and the structure has shifted from FF to LU. This suggests that this cluster may be involved in the allosteric interaction that occurs as the structure undergoes this conformational change.

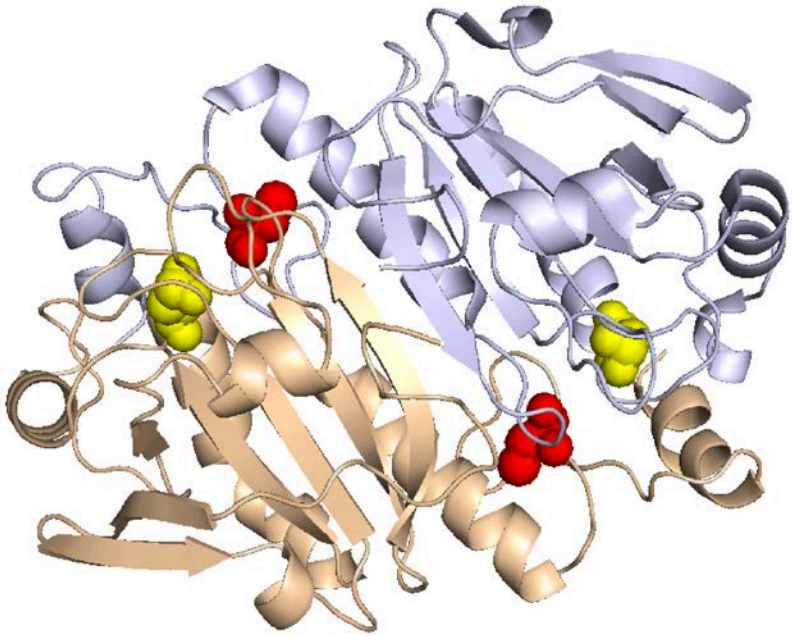

*Figure 5.9: Dimer of Prx2 with peroxidatic and resolving cysteines shown in spherical form. Chain D, which was used for the analysis, is shown in grey, and Chain C, its homodimer, is shown in gold. $C_P$ is shown in yellow and $C_R$ is shown in red on each monomer.*

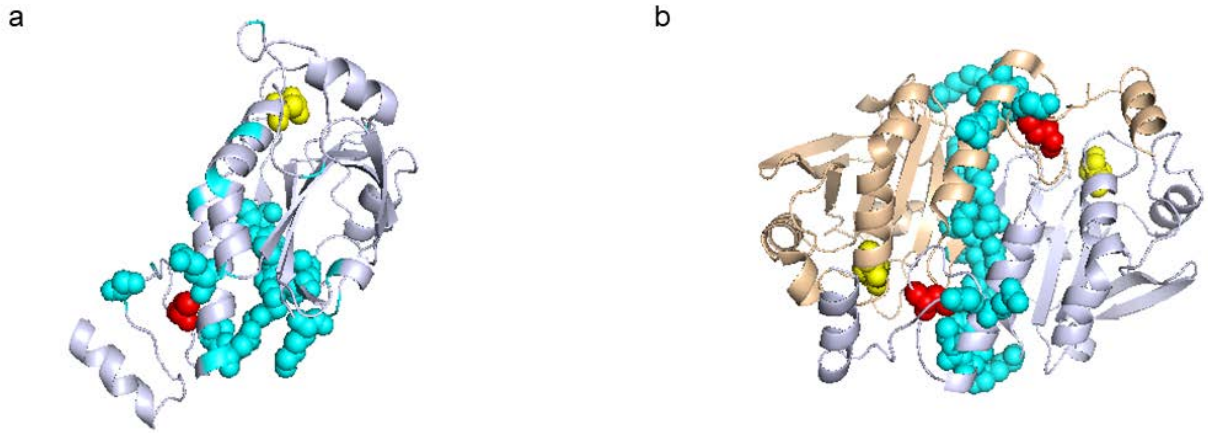


*Figure 5.10: Prx2 cluster 1. Cluster 1 from Figure 5.8a superimposed in cyan on a) Chain D of Prx2 and b) both monomers. $C_P$ shown in yellow and $C_R$ shown in red.*

The second major cluster, cluster 2, is depicted in Figure 5.11. This cluster spans the length of the protein. This cluster connects $C_P$ and $C_R$ through the core of the protein and by forming parts of the binding pockets. Similar to cluster 1, this cluster likely contributes to the conformational changes that take place during catalysis as the protein changes from FF to LU. This cluster also interfaces with the dimer-dimer interface formed when Prx2 is in a decamer. It has been

demonstrated in microbes that Tsa1, a homolog of Prx2, exists as a decamer until oxidation, at which point the dimer dissociates from the higher-order complex [13]. This mechanism has been hypothesized to be consistent in mammals. Cluster 2 is suggestive of this putative decamer-to-dimer transistion that occurs when the protein interacts with its substrate.

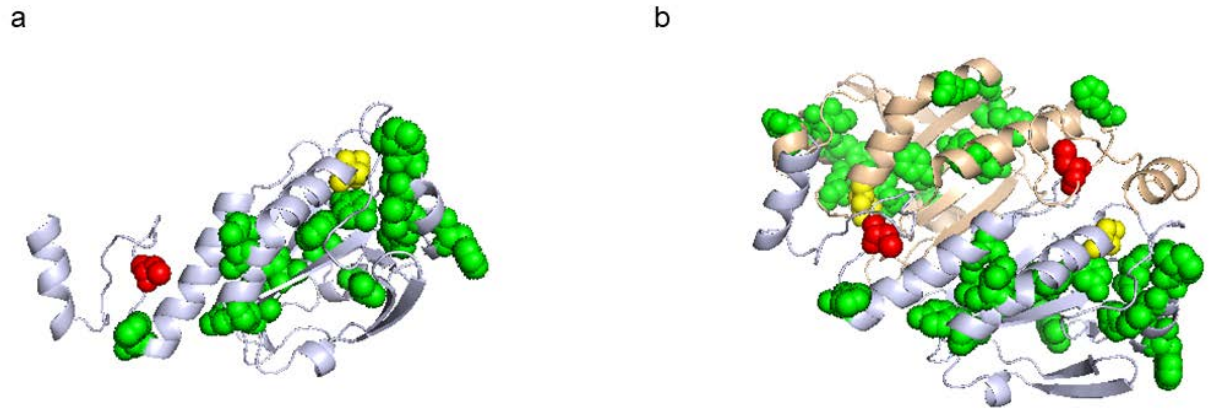


*Figure 5.11: Prx2 cluster 2. Cluster 2 from Figure 5.8a superimposed in green on a) Chain D of Prx2 and b) both monomers. $C_P$ shown in yellow and $C_R$ shown in red.*

Cluster 3 is depicted in Figure 5.12 and is a bit disjointed across the protein, with several clusters around the C-terminus of the monomer surrounding the $C_R$ binding pocket and two residues in the middle of each monomer. The isolated residues are Phe15 and Leu117. Similarly, cluster 4, shown in Figure 5.13, also surrounds the C-terminus. These clusters may be involved in the newly hypothesized protein-protein interactions between Prx2 and important signaling or structural proteins within the cell [7,8]. It has already been established that the C-terminus of Prx proteins is the site of interaction with sulfiredoxin (Srx) [14]. This YF motif must move in order for disulfide bond formation to occur, so clusters 3 and 4 are also most likely conserved because of this catalytic mechanism. Clusters 3 and 4 are shown together in Figure 5.14a, demonstrating how they complement each other at the C-terminus of each monomer. Figure 5.14b shows all the clusters together; this depiction demonstrates how conserved residues can allosterically link the two cysteine pockets across the entire protein structure, as well as provide sites of interface.

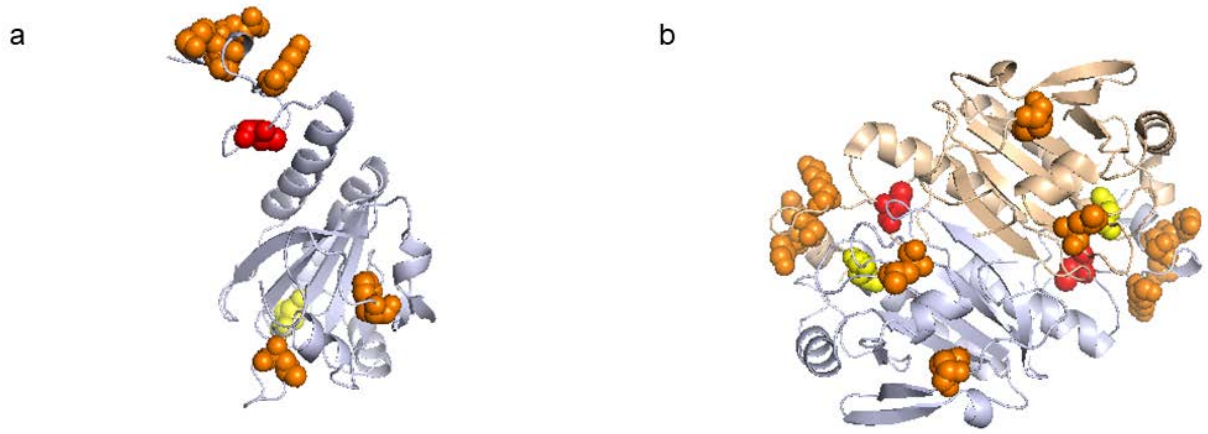


*Figure 5.12: Prx2 cluster 3. Cluster 3 from Figure 5.8a superimposed in orange on a) Chain D of Prx2 and b) both monomers. $C_P$ shown in yellow and $C_R$ shown in red.*

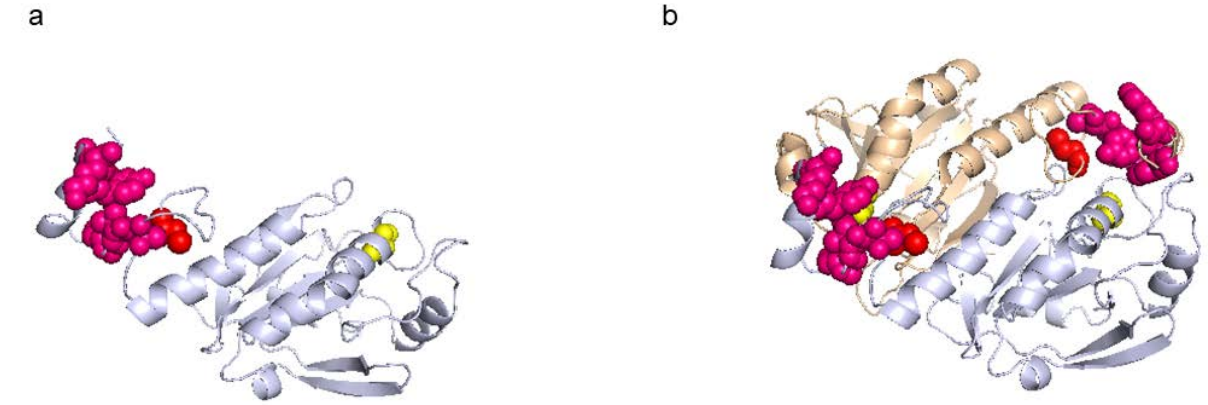


*Figure 5.13: Prx2 cluster 4. Cluster 4 from Figure 5.8a superimposed in magenta on a) Chain D of Prx2 and b) both monomers. $C_P$ shown in yellow and $C_R$ shown in red.*

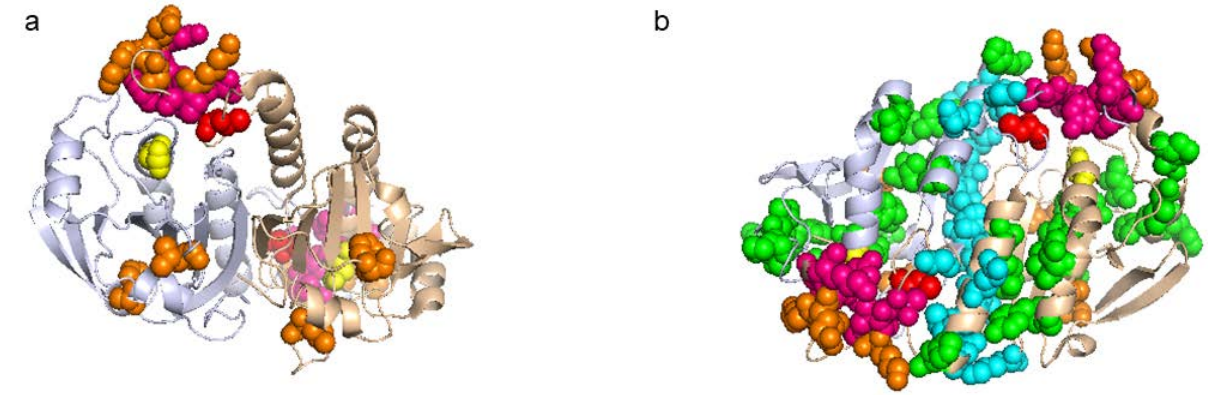


*Figure 5.14: Prx2 protein sectors. a) Clusters 3 and 4 shown together on the Prx2 dimer. b) All four clusters shown together on the Prx2 dimer. $C_P$ shown in yellow and $C_R$ shown in red.*

Figure 5.15 depicts the Prx1 with $C_P$ and $C_R$ highlighted. This structure originally came from a crystal structure in complex with two molecules of Srx, bound in the large gaps between the C-terminus of one monomer and the $C_P$ of the other. These molecules were omitted from the figures for simplicity and clarity. Cluster 1 for Prx1 is depicted in Figure 5.16, and appears to have elements spanning the core of the protein from the dimer interface to the outer face of the monomers. This cluster's role is not obvious, but could be involved in interfacing with other molecules and/or the homodimer.

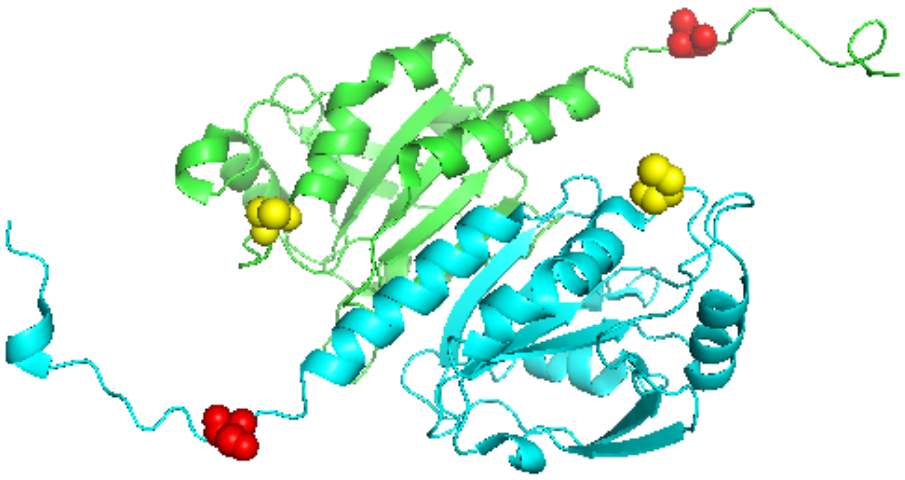

*Figure 5.15: Dimer of Prx1 with peroxidatic and resolving cysteines shown. Chain A is shown in green and Chain B, its homodimer, which was used for the analysis, is shown in cyan. $C_P$ is shown in yellow and $C_R$ is shown in red on each monomer. The Srx from this protein complex crystal structure are not shown for simplicity.*

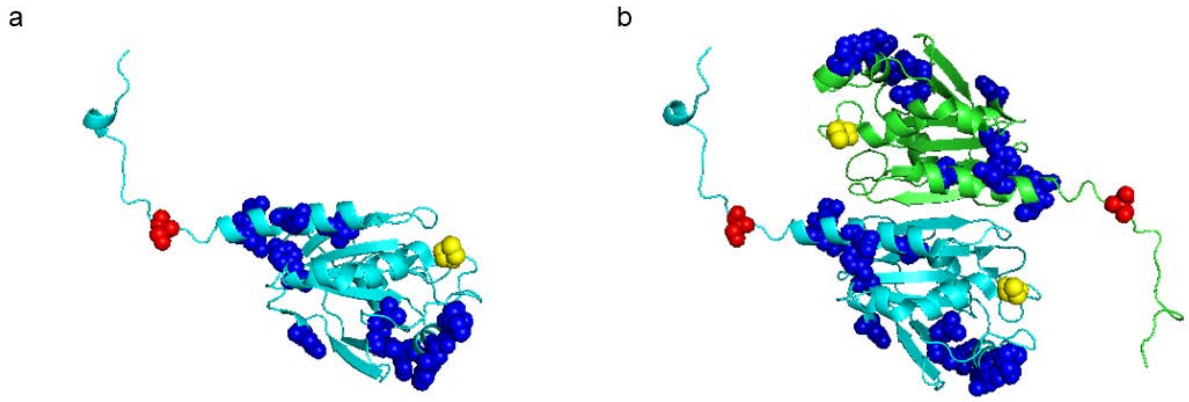


*Figure 5.16: Prx1 cluster 1. Cluster 1 from Figure 5.8b superimposed in blue on a) Chain B of Prx1 and b) both monomers. $C_P$ shown in yellow and $C_R$ shown in red.*

Cluster 2 for Prx1 is depicted in Figure 5.17. As seen for Prx2, this cluster spans the C-terminus of the monomers and also has a couple isolated residues in the center of the structure. In this structure, where the C-terminus is swung out to interact with Srx, the role of this cluster is more apparent. This is shown with Srx in context within the structure in Figure 5.19b along with all the clusters.

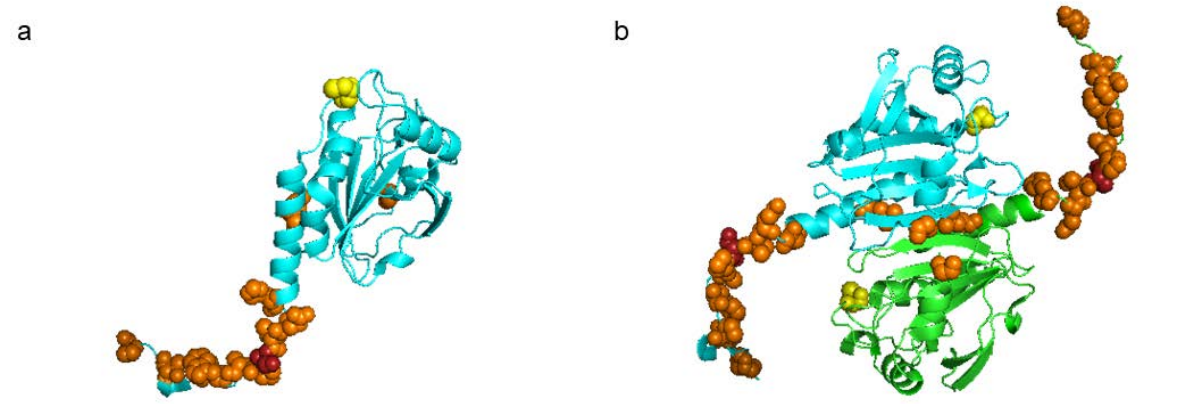


*Figure 5.17: Prx1 cluster 2. Cluster 2 from Figure 5.8b superimposed in orange on a) Chain B of Prx1 and b) both monomers. $C_P$ shown in yellow and $C_R$ shown in red.*

Cluster 3 is depicted in Figure 5.18. This cluster had the weakest SCA scores, but shares a similar form to a high-scoring cluster from Prx2, spanning the interface of the homodimer and linking $C_P$ with $C_R$. Similar to Prx2, this cluster could provide an allosteric mechanism for the conformational changes that occur during catalysis. All the clusters mapped together on the protein

structure, shown in Figure 5.19, suggest a cooperative allosteric mechanism along the C-terminus through the interface of the homodimer. This may aid Prx1 in interacting with other proteins like Srx [12].

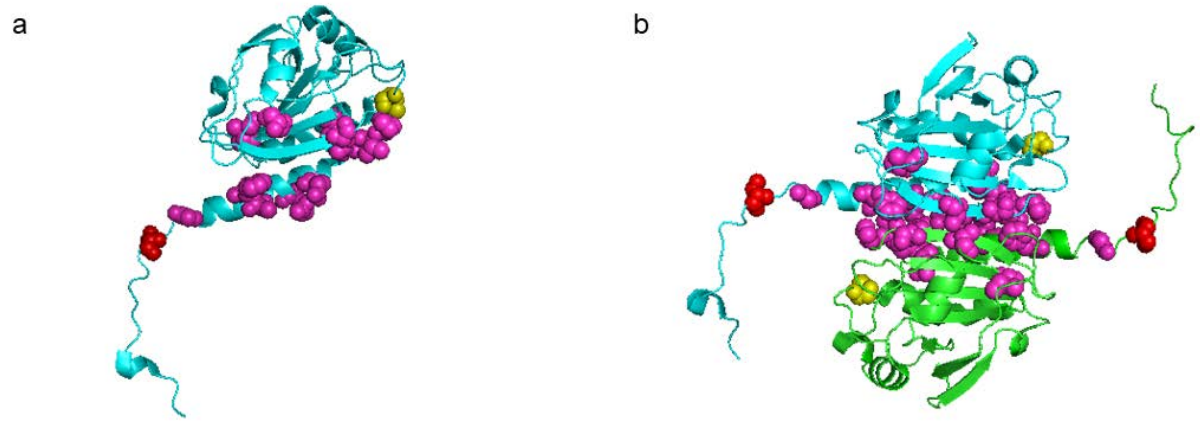


*Figure 5.18: Prx1 cluster 3. Cluster 3 from Figure 5.8b superimposed in magenta on a) Chain B of Prx1 and b) both monomers. $C_P$ shown in yellow and $C_R$ shown in red.*

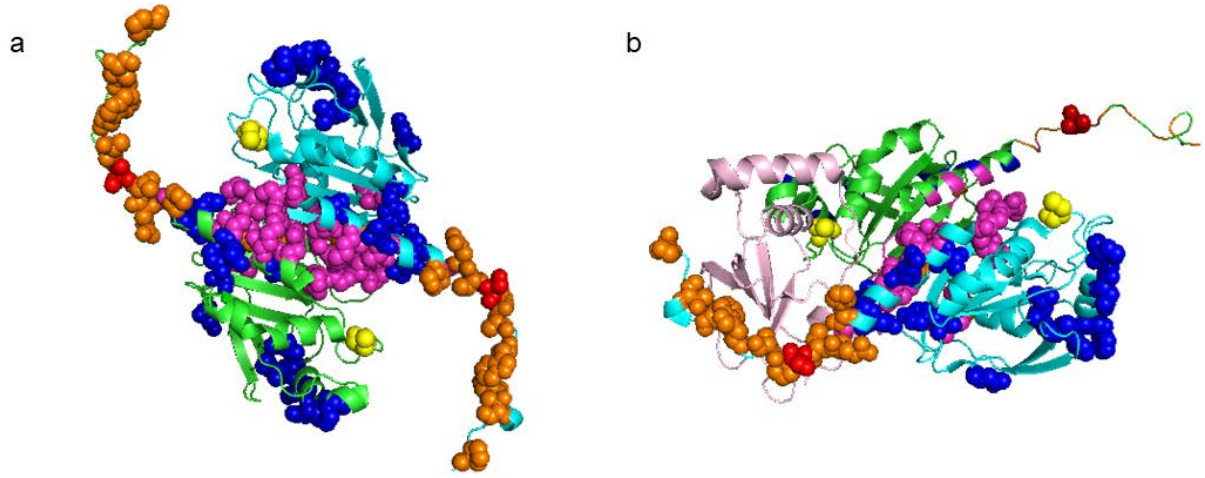


*Figure 5.19: Prx1 protein sectors. a) All three clusters shown on the Prx1 dimer. b) One Srx group shown in pink in the dimer complex, with clusters represented as spheres on Chain B of Prx1. $C_P$ shown in yellow and $C_R$ shown in red.*

This analysis demonstrated that SCA was a useful tool for discerning more information about the structure-function relationship of Prx2 and Prx1. It enabled the identification of four groups of highly correlated residues in the Prx2 family and three groups in the Prx1 family. These groups corroborate allosteric interactions in the suggested cooperative mechanism for Prx action [14]. They describe a residue network that could induce the structural changes that are hypothesized

to occur within each monomer upon oxidation. The C-terminus clusters could describe a residue network responsible for a docking site for protein-protein interactions. Finally, the unexpected identification of cluster 2 in Prx2 indicated a group of residues that could be responsible for dimer-dimer binding in the formation of the decamer ring, indicating that there may be cooperativity upon oligomerization.

Experimental validation of these residue networks would provide more confidence in the function of these clusters. This would be achieved by creating mutant proteins and doing double-mutant cycles to understand if sites are coupled as predicted. One region to pursue in these proteins will likely be the sites at the C-terminus, which seems to be a possible protein-protein interaction site; performing double-mutant cycles of the residues within these clusters and observing whether the ability of the Prxs to interact with downstream proteins like Trx and Srx is intact will be interesting. Efforts already exist to explore different motifs within the proteins using mutant and chimera strategies [15]. These SCA data provide a future direction for these structural biology efforts that will help elucidate the functional significance of the sectors within Prx2 and Prx1.

## 5.4 References


(1) Rhee, S. G.; Woo, H. A.; Kil, I. S.; Bae, S. H. Peroxiredoxin Functions as a Peroxidase and a Regulator and Sensor of Local Peroxides. *J. Biol. Chem.* **2012**, *287* (7), 4403–4410.

(2) Portillo-Ledesma, S.; Randall, L. M.; Parsonage, D.; Dalla Rizza, J.; Karplus, P. A.; Poole, L. B.; Denicola, A.; Ferrer-Sueta, G. Differential Kinetics of Two-Cysteine Peroxiredoxin Disulfide Formation Reveal a Novel Model for Peroxide Sensing. *Biochemistry* **2018**, acs.biochem.8b00188.

(3) Young, D.; Pedre, B.; Ezeriņa, D.; De Smet, B.; Lewandowska, A.; Tossounian, M.-A.; Bodra, N.; Huang, J.; Astolfi Rosado, L.; Van Breusegem, F.; et al. Protein Promiscuity in H 2 O 2 Signaling. *Antioxid. Redox Signal.* **2019**, *30* (10), 1285–1324.

(4) Winterbourn, C. C.; Peskin, A. V. Kinetic Approaches to Measuring Peroxiredoxin Reactivity. *Mol. Cells* **2016**, *39* (1), 26–30.

(5) Yewdall, N. A.; Peskin, A. V.; Hampton, M. B.; Goldstone, D. C.; Pearce, F. G.; Gerrard, J. A. Quaternary Structure Influences the Peroxidase Activity of Peroxiredoxin 3. *Biochem. Biophys. Res. Commun.* **2018**, *497* (2), 558–563.

(6) Winterbourn, C. C. Biological Production, Detection, and Fate of Hydrogen Peroxide. *Antioxid. Redox Signal.* **2017**, *29* (6), 541–551.

(7) Sobotta, M. C.; Liou, W.; Stöcker, S.; Talwar, D.; Oehler, M.; Ruppert, T.; Scharf, A. N. D.; Dick, T. P. Peroxiredoxin-2 and STAT3 Form a Redox Relay for H2O2 Signaling. *Nat. Chem. Biol.* **2014**, *11* (1), 64–70.
(8) Pace, P. E.; Peskin, A. V.; Konigstorfer, A.; Jasoni, C. J.; Winterbourn, C. C.; Hampton, M. B. Peroxiredoxin Interaction with the Cytoskeletal-Regulatory Protein CRMP2: Investigation of a Putative Redox Relay. *Free Radic. Biol. Med.* **2018**, *129* (October), 383–393.
(9) Travasso, R. D. M.; Sampaio dos Aidos, F.; Bayani, A.; Abranches, P.; Salvador, A. Localized Redox Relays as a Privileged Mode of Cytoplasmic Hydrogen Peroxide Signaling. *Redox Biol.* **2017**, *12* (November 2016), 233–245.
(10) Süel, G. M.; Lockless, S. W.; Wall, M. A.; Ranganathan, R. Evolutionarily Conserved Networks of Residues Mediate Allosteric Communication in Proteins. *Nat. Struct. Biol.* **2003**, *10* (1), 59–69.
(11) Schröder, E.; Littlechild, J. A.; Lebedev, A. A.; Errington, N.; Vagin, A. A.; Isupov, M. N. Crystal Structure of Decameric 2-Cys Peroxiredoxin from Human Erythrocytes at 1.7 A Resolution. *Structure* **2000**, *8* (6), 605–615.
(12) Jönsson, T. J.; Johnson, L. C.; Lowther, W. T. Structure of the Sulphiredoxin–peroxiredoxin Complex Reveals an Essential Repair Embrace. *Nature* **2008**, *451*, 98.
(13) Low, F. M.; Hampton, M. B.; Winterbourn, C. C. Peroxiredoxin 2 and Peroxide Metabolism in the Erythrocyte. *Antioxid. Redox Signal.* **2008**, *10* (9), 1621–1630.
(14) Lowther, W. T.; Haynes, A. C. Reduction of Cysteine Sulfinic Acid in Eukaryotic, Typical 2-Cys Peroxiredoxins by Sulfiredoxin. *Antioxid. Redox Signal.* **2010**, *15* (1), 99–109.
(15) Bolduc, J. A.; Nelson, K. J.; Haynes, A. C.; Lee, J.; Reisz, J. A.; Graff, A. H.; Clodfelter, J. E.; Parsonage, D.; Poole, L. B.; Furdui, C. M.; et al. Novel Hyperoxidation Resistance Motifs in 2-Cys Peroxiredoxins. *J. Biol. Chem.* **2018**, *293* (30), 11901–11912.

## 5.5 Appendix

Sequence of Prx2:

SGNARIGK PAPDFKATAV VDGAFKEVKL SDYKGKYVVL FFYPLDFTFV CPTEIIAFSN RAEDFRKLGC EVLGVSVDSQ FTHLAWINTP RKEGGLGPLN IPLLADVTRR LSEDYGVLKT DEGIAYRGLF IIDGKGVLRQ ITVNDLPVGR SVDEALRLVQ AFQYTDEHGE VCPAGWKPGS DTIKPNVDDS KEYFSKHN

Sequence of Prx1:

SGNAKIGH PAPNFKATAV MPDGQFKDIS LSDYKGKYVV FFFYPLDFTF VCPTEIIAFS DRAEEFKKLN CQVIGASVDS HFCHLAWVNT PKKQGGLGPM NIPLVSDPKR TIAQDYGVLK ADEGISFRGL FIIDDKGILR QITVNDLPVG RSVDETLRLV QAFQFTDKHG EVCPAGWKPG SDTIKPDVQK SKEYFSKQK

*Table 5.1: List of residues associated with each cluster in Prx2.*

| Cluster | Residues |
|---|---|
| 1 | 135 + 141 + 165 + 166 + 138 + 139 + 140 +142+179+160 |
| 2 | 26+32+ 41 + 43 + 46 + 83 +64+111+168+39+131+69+37+87+ 89 +90+ 81 +155 |
| 3 | 15 + 118 + 184 + 190 + 191 +192 |
| 4 | 185 + 196 + 183 +193+194+182 |

*Table 5.2: List of residues associated with each cluster in Prx1*

| Cluster | Residues |
|---|---|
| 1 | 20+91+33+82+156+104+81+38+89+90+161+166+167 |
| 2 | 169+159+171+172+174+173+175+177+183+179+186+4 |
| 3 | 133+145+148+150+151+155+149+158+162+170+163+3 |

# Chapter 6 : Conclusions and Outlook

This thesis has developed tools and methodology for understanding hydrogen peroxide ($H_2O_2$) perturbations in the mitochondria. It expanded upon previous work focused on cytoplasmic perturbations. Using a genetically encoded generator of $H_2O_2$ targeted to the mitochondrial matrix, a tunable platform for making mechanistic perturbations was demonstrated. These perturbations were observed to be dramatically more toxic than comparable one directed to the cytoplasm. Consistent with previous findings, $H_2O_2$ toxicity in the mitochondria was dose- and time-dependent, highlighting the importance of considering the dynamics of $H_2O_2$ signaling. Finally, interesting evidence of $H_2O_2$ protein modifications was found outside of the mitochondria at high perturbations, implying that that are competing kinetic and transport processes at play.

To enhance the mechanistic understanding developed experimentally, a computational model of the mitochondrial $H_2O_2$ reaction network was constructed. This modeled the kinetics of the major antioxidant pathways, aka redox couples, and tracked the concentration of not only $H_2O_2$ but the oxidized and reduced forms of all the relevant protein species. Using the model, basal steady-state mitochondrial $H_2O_2$ was predicted to vary with the overall available pool of peroxiredoxin-3 (Prx3) and to be in the low nM range (~3 nM). This is in good agreement with our group's predictions of ~80 pM cytosolic $H_2O_2$; a higher steady state mitochondrial $H_2O_2$ concentration is expected for transport to be possible from the mitochondria to the cytoplasm. This prediction is also about one order of magnitude lower than existing literature predictions, though these simulations were made in faster-respiring cells than HeLa cells, which could account for the discrepancy. It was also predicted that the mitochondrial reaction network could control $H_2O_2$ perturbations well, up to a threshold (~50 µM/s or 0.25 nmol/mg-protein/s generation). At high rates of perturbation, the Prx3 network collapsed, and the $H_2O_2$ concentration in the mitochondria was no longer well controlled. Only at these extreme perturbations did the other antioxidants

become oxidized, implying that Prx3 controls mitochondrial $H_2O_2$ dynamics. This points to the Prx system as a potential target for future proteomic studies interested in cancer and chemotherapeutic susceptibility. Finally, it was observed that at short times, there was good experimental agreement with the model, but at long times, transport becomes more important, causing the model to over-estimate hyperoxidation.

A method for testing redox-based drugs in primary patient samples was developed based on high-throughput techniques. Patient tumor samples were split as homogeneously as possible into 96-well plates to provide at least three replicates per dose to create a dose-response curve with good statistical power. These plates were fixed and stained post-treatment, and imaged using a high-throughput microscopy system. An automatic image analysis pipeline developed in the software CellProfiler allowed a more rapid data processing of the volume of images that came out of the experiments in order to generate dose-response curves. This methodology was applied to pheochromocytoma, paraganglioma, and gastrointestinal stromal tumor (GIST) cells treated with the investigational chemotherapeutic piperlongumine and preliminary results demonstrated some toxicity of this drug in these tumor types.

The peroxiredoxin (Prx) family of proteins is remarkably conserved across all kingdoms of life. The Prxs were analyzed using a computational technique known as statistical coupling analysis (SCA) to look for evolutionarily conserved residues and predict protect sectors or residues that may be promising for mutational studies. This algorithm was applied to a sequence family related to Prx2 and Prx1. The analysis found four conserved clusters in the Prx2 family and three conserved clusters in the Prx1 family. Both proteins showed a conserved cluster at the C-terminus of the protein, near the resolving cysteine, that may be involving in Prx ability to complex with other proteins.

This thesis has elucidated several interesting points about $H_2O_2$ and related proteins, and leaves more questions that can be answered to further evolve our understanding. The dramatic cell death observed with mitochondrial $H_2O_2$ perturbations was only the beginning of the field's understanding of these cell death mechanisms. Thanks to the model, we now have a good idea of the approximate magnitude of some of these perturbations, but now determine the downstream protein targets and the signaling cascades with which $H_2O_2$ participates is a new challenge. A systems biology approach to this question may be a promising solution, wherein a multidimensional dataset is captured and regressed to understand how much each component is contributing to the observed phenotype. High-throughput methods like Luminex exist to interrogate the phosphoproteome, which can be paired with the low-throughput methods like Western blot that are necessary to interrogate the redox proteins. A systems-level understanding of $H_2O_2$ signaling will help in our quest to find good drug targets in the future.

More complete models is another new area where this field is headed. Great strides have been made in computational modeling in redox biology already. Future models could take several forms. Reaction-diffusions models could investigate how $H_2O_2$ (and probably other protein species) traffic from the mitochondria to the cytoplasm. For this, more experiments will be necessary to estimate mass transfer parameters. Another strategy would be to implement rule-based modeling, which is simply a different representation of biochemical systems—still based on kinetics—that tends to scale better as more species and reactions are added.

The SCA analysis bore out interesting findings. The conserved clusters of residues at the C-terminus in both Prx2 and Prx1 was of particular interest. Structural biology studies are underway with collaborators at several institutions to try to understand how these protein sectors

contribute to the Prxs' ability to complex with proteins. In particular, this could shed light on the so-called redox relay hypothesis that has been emerging.

Moving some of these tools and methodologies out of proof-of-concept systems and into more clinically interesting systems is another future direction. Based on public databases, it looks like some pancreatic cancers, glioblastomas, and hepatic cancers may be interesting systems to study to quantify differences in $H_2O_2$ signaling and metabolism. Still another as-of-yet unexplored avenue is moving these tools into non-cancerous cell lines and quantifying the differences between cancer and non-cancer cells. This is a concept that the selective cancer killing hypothesis relies upon, but that has not been rigorously validated. Taking these tools and beginning to make measurements in interesting systems will not only shed light on existing hypotheses in the field, but generate new ideas for the mechanisms underlying the pathologies we are studying.

# APPENDIX A: Measurement of peroxiredoxin-2 and peroxiredoxin-3 oxidation in patient-derived tumors

Previous work in the area of redox-directed cancer therapeutics has suggested that small molecule compounds in this class have the potential to selectively kill certain cancer cells through intracellular elevation of oxidants. Tumors that carry genetic modifications thought to elevate intracellular fluxes of oxidants may be particularly susceptible to this approach. However, evaluating the functional significance of various mutations and identification of specific tumor types that might benefit the most from these treatments remains a challenge. The oxidation states and abundances of peroxiredoxin isoforms provide information about basal hydrogen peroxide fluxes. However, most existing studies have been performed *in vitro*, using methods developed with immortalized cell lines. We have extended these methods to examine $H_2O_2$ fluxes in the cytosol and mitochondria of patient-derived tumor samples. Using a patient-derived xenograft (PDX) model, we compared the effectiveness of the alkylating agents N-ethyl maleimide (NEM) and methyl methanethiosulfonate (MMTS) in minimizing lysis-induced oxidation of protein-thiols in tumor homogenates. Our results show that both NEM and MMTS can reduce artificial peroxiredoxin oxidation to a similar extent in these samples, and that the addition of these agents to tumor samples prior to cryopreservation is required in order to avoid a prohibitive amount of artificial protein-thiol oxidation. Finally, the expression levels of the cytosolic and mitochondrial peroxiredoxin isoforms in the tumors we analyzed appeared to be similar to expression levels commonly observed in immortalized cell lines, which allows these proteins to retain their high reaction rate with $H_2O_2$.

## A.1 Introduction

The advent of personalized medicine has spurred the production of numerous therapies that target specific molecular signatures of disease, and these targeted therapies have had success in the treatment of several types of disorders [1–3]. In cancer treatment, use of these therapies revolves around identification of biomarkers that are expressed by tumor cells and point to specific molecules or pathways with altered activity that can be targeted in order induce selective cancer cell death [1]. Redox cancer therapeutics target cancer cells' enhanced susceptibility to oxidant-induced stress and elevate intracellular levels of key oxidants past the toxicity threshold for these species in order to induce cell death [4–7]. Previously, Blackman et al. and Miyajima et al. suggested that the small-molecule compounds cisplatin and elesclomol, respectively, act in part through elevated oxidative species in the mitochondria of human cancer cells [8,9], and Huang et al. demonstrated that the small molecule compound piperlongumine induces toxicity through $H_2O_2$ elevation in the cytosol of human cancer cells [10]. However, clinicians currently do not have a reliable biomarker for use as a metric to determine which tumors would benefit the most from these treatments. Several researchers have hypothesized that tumor types with elevated fluxes of intracellular $H_2O_2$ or decreased capacity to reduce $H_2O_2$ could exist much closer to the toxicity threshold for this species, thus exhibiting a higher sensitivity to $H_2O_2$-based therapeutics [4–7]. However, in order to maximize the efficacy of these treatments and reduce the amount of off-target toxicity, researchers and clinicians require better methods to measure molecular indicators of $H_2O_2$ stress in patient tumor tissue.

Gastrointestinal stromal tumors (GISTs) are mesenchymal tumors found in the gastrointestinal tract of humans, and can occur in men and women of all ages. Succinate dehydrogenase (SDH) deficient GISTs are a rare type of tumor in this group, characterized by lack of active SDH in the tumor cells' mitochondrial membrane, resulting in impairment of electron

transport chain (ETC) function and normal aerobic respiration. As a result of impaired mitochondrial function in cells, researchers have hypothesized that these tumors may have higher rates of production of $H_2O_2$, endowing them with a higher sensitivity towards $H_2O_2$-mediated cancer therapeutics [11]. However, methods for assessing the functional significance of particular mutations in SDH and other components of the ETC are currently lacking.

In order to withstand oxidative insults, cells utilize a network of antioxidant proteins that includes peroxiredoxins (Prxs), glutathione peroxidases, and catalase that consume $H_2O_2$ [12,13]. Due to the relatively high reactivity of Prxs with $H_2O_2$ in comparison with that of other reaction partners [14,15], these proteins act as natural intracellular sensors of this oxidant [16,17]. In order to maintain large pools of reduced Prx that can respond to slight fluctuations in intracellular $H_2O_2$ levels, cells rely upon thioredoxin (Trx) and thioredoxin reductase (TrxR) to constantly reduce oxidized Prxs. As a result, changes in Prx oxidation can indicate changes in both intracellular $H_2O_2$ as well as Trx and TrxR activity, and reflects the capacity of the cell to respond to further elevation of $H_2O_2$. In to order assess oxidation of Prxs in cells, researchers have utilized an electrophoretic method that relies upon lysis of cell samples, followed by non-reducing SDS-PAGE, and finally, western blotting for the Prx isoform of interest [17,18]. This analysis reveals the oxidation state of Prx; under these conditions, reduced forms of the protein appear as monomers and oxidation results in disulfide-linked dimers. However, due to the extremely high sensitivity of Prxs towards $H_2O_2$, freeze-thaw processes and other procedures that disrupt the membrane of the cell can expose Prxs to $H_2O_2$ in the extracellular media or buffer, which can result in artificial oxidation of Prxs [17]. In order to reduce this lysis-induced oxidation, previous studies have used alkylating agents such as methyl methanethiosulfonate (MMTS) and N-ethylmaleimide (NEM) in order to alkylate free thiol groups on proteins in established cell lines and effectively trap the oxidation state of these proteins

[17,18]. However, to our knowledge no studies to date have explored the variable space around use of these alkylating agents for preparation of Prx protein from patient-derived tumor samples.

It was recently noted that knowledge of Prx protein status in tumors is lacking [19]. Establishing a clear methodology for measuring Prx oxidation status in tumor tissue is the first step in obtaining these valuable data. In the present study, we employed our recently-characterized patient-derived xenograft (PDX) model of SDH-deficient human GIST to optimize conditions for assessing Prx oxidation status as a biomarker for oxidant induced stress in human tumor samples [20]. Building upon previous work done with heart tissue from mice [21], we tested several protocols for protein extraction from tumor tissue, and used non-reducing SDS-PAGE followed by western blots as a means to measure the fraction of oxidized Prx2 and Prx3 in the cytosol and mitochondria, respectively. Our results suggest that both NEM and MMTS can reduce artificial oxidation of Prx2 and Prx3 to a similar extent. Furthermore, addition of the NEM immediately before preservation of the tumor tissue on dry ice decreases the amount of observed artificial oxidation in both Prx2 and Prx3 to a similar degree as immediate lysis of fresh tumor tissue after surgical excision, which resulted in the greatest reduction in artificial oxidation.

## A.2 Materials and Methods

*A.2.1 : Origin and description of tumor model*

As previously reported, the PDX model, which we have called “the Ian GIST model”, was derived from a gastric GIST in a 17 year-old male patient with a hereditary *SDHB* mutation (423+1G>A) and family history of paragangliomas [20]. In addition to the germline *SDHB* mutation, the tumor harbored a somatic *KRAS* G12D mutation. Work with this model was approved by the Institutional Review Board at Tufts Medical Center.

*A.2.2 : Extraction of intracellular protein from patient-derived xenograft model tumor*

Excised tumor tissue samples were first placed into 1.5 mL tubes with 1 mL of PBS with either MMTS (Sigma Aldrich) or NEM (Sigma Aldrich) at various concentrations in order to block free thiol groups [17,18,21], and incubated on ice for approximately 50 minutes. After incubation with either MMTS or NEM, a portion of the tissue samples were snap-frozen on dry ice and stored in liquid nitrogen. The remainder of the tissue samples were added to separate 1.5 mL tubes with 100 μL of RIPA lysis buffer with either MMTS or NEM at various concentrations plus 1x HALT protease inhibitor, similar to previous work [21]. Samples were then ground with a manual tissue homogenizer and centrifuged at approximately 18,000xg for 10 minutes at 4 °C. After centrifugation, the supernatant of the samples was collected and stored at -20 °C.

Previously snap-frozen samples were thawed on ice and immediately placed in 1.5 mL tubes with 1 mL of PBS with either MMTS or NEM, and incubated on ice for approximately 50 minutes. The samples were then treated as the other samples and the lysate supernatant was stored at -20 ° C.

*A.2.3 : Gel electrophoresis and Prx oxidation western blots*

After extraction of protein from the tumor samples, the lysates were first passed through a sepharose spin column (GE) in order to remove any excess alkylating agent from the lysate solution. For Prx2 and Prx3 non-reducing western blots, 25 μg of protein was then loaded into a tris-tricine acrylamide gel and subjected to SDS-PAGE under non-reducing conditions (i.e. with no β-mercaptoethanol in sample buffer). The separated proteins were transferred to a polyvinylidene difluoride (PVDF) membrane (Bio-Rad) (1 hour at 100V), then the membrane was subsequently blocked with Odyssey blocking buffer (Licor). Primary antibody staining was performed at 4 °C overnight with either goat anti-Prx2 (R&D Systems, Catalog # AF3489) (at a dilution of 1:800) or rabbit anti-Prx3 (Abcam, Catalog #ab129206) (at a dilution of 1:10000), as

well as rabbit anti-β-tubulin (Cell Signaling Technology, #2146) (at a dilution of 1:1000) as a loading control, and then secondary antibody staining was performed for 1 hour at room temperature with donkey anti-goat IR 688 (Licor) (at a dilution of 1:10000) or donkey anti-rabbit IR 800 (Licor) (at a dilution of 1:10000). The tagged proteins were then visualized on the Odyssey CLx Infrared Imaging System. Densitometry quantifications were done using Image Studio Lite software and ImageJ.

*A.2.4 : Statistical Analysis*

In order to isolate the effects of the treatment being investigated, tumor fragments from the same parent tumor were used. Microsoft Excel's built-in statistical analysis toolbox was used to perform two-tailed Student's t-test where appropriate.

## A.3 Results

*A.3.1 : Effect of lysis-induced oxidation on Prx oxidation status in human tumor samples*

Due to the existence of trace amounts of $H_2O_2$ in aqueous buffers, disruptive techniques such as rapid freeze/thaw of tumor tissue samples or cell membrane permeabilization with detergents can result in introduction of additional $H_2O_2$ to the internal environment of the cell. Since Prxs react so readily with $H_2O_2$, they react with virtually all of this species that enters the cell, which results in the formation of oxidized Prx dimer species (Figure A.1a). In order to determine the extent of this artificial oxidation in a PDX model of human GIST, we first thawed a section of tissue, homogenized it with detergent, and retained the soluble protein in the lysate. We subsequently separated the protein via non-reducing SDS-PAGE, transferred the protein to a PVDF membrane, and probed the membrane for oxidized and reduced Prx2 (which exists in the cytosol) and Prx3 (which exists in the mitochondria) (Figure A.1b-c). As shown in Figure A.1,

virtually all of the Prx protein was found in the oxidized dimer state, which suggests that artificial oxidation has occurred.

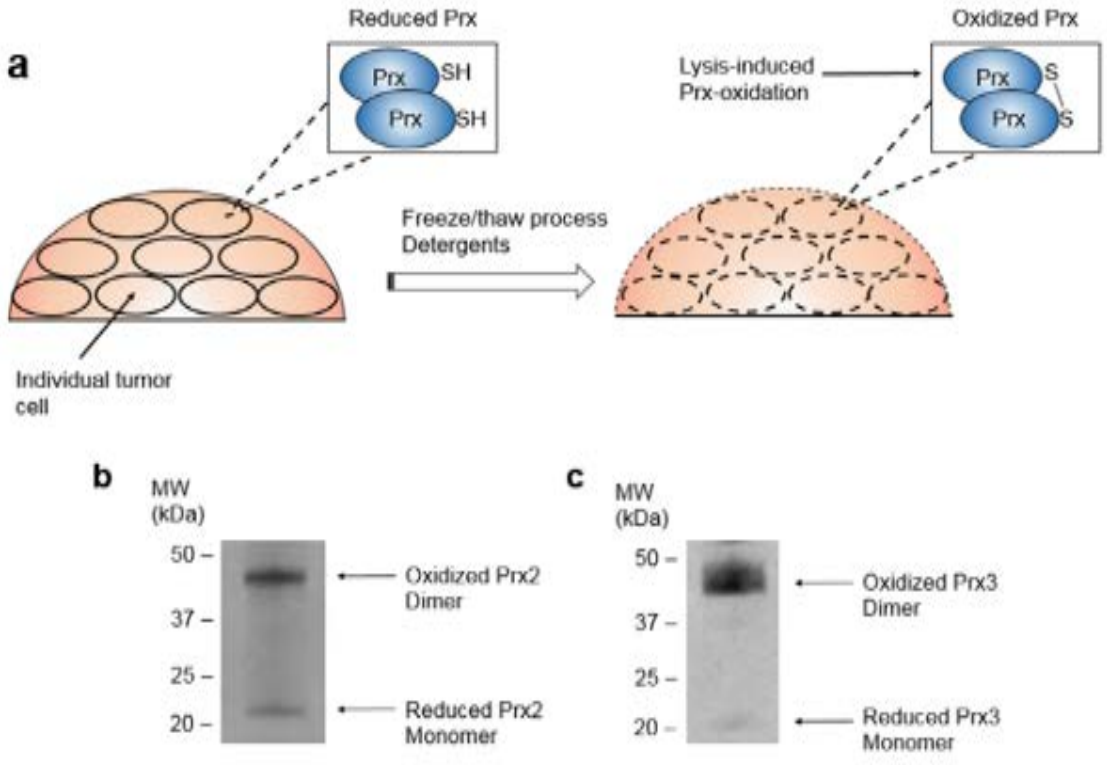


*Figure A.1: Effect of lysis-induced oxidation on Prx status in human tumor samples. (a) Schematic representation of effect of freeze/thaw process and detergents on oxidation state of Prx in human tumor samples. (b) Prx2 dimerization in untreated human GIST xenograft samples. (c) Prx3 dimerization in untreated human GIST xenograft samples. Representative of two blots.*

### *A.3.2 : Effect of alkylating agent and lysis conditions on measurement of Prx2 and Prx3 oxidation in xenograft model GIST*

Given the large amounts of oxidized Prx protein in all of the lanes of the blots in Figure A.1, we next sought to optimize the protein extraction protocol for this tissue sample type in order to minimize any artificial oxidation that resulted from the tumor extraction and homogenization process. In order to determine the optimal parameters for this process, we used three different

concentrations of two different alkylating agents to block free thiols on Prx protein in GIST tumor fragments, homogenized the tumor fragments, and immunoblotted the lysates for both Prx2 and Prx3 (Figure A.2b-e). Tumor fragments were obtained from the same parent tumor to isolate the variability associated with the alkylation methods. As shown in Figure A.2, addition of the alkylating agents significantly reduced the fraction of oxidized Prx protein in each lane compared to the control with no alkylating agent. In addition, higher amounts of alkylating agents reduced the fraction of oxidized protein in each lane even further in several instances. In contrast with prior reports of other sample types [17,18], in this new sample type, the two alkylating agents appeared to reduce the fraction of oxidized protein with equal efficacy.

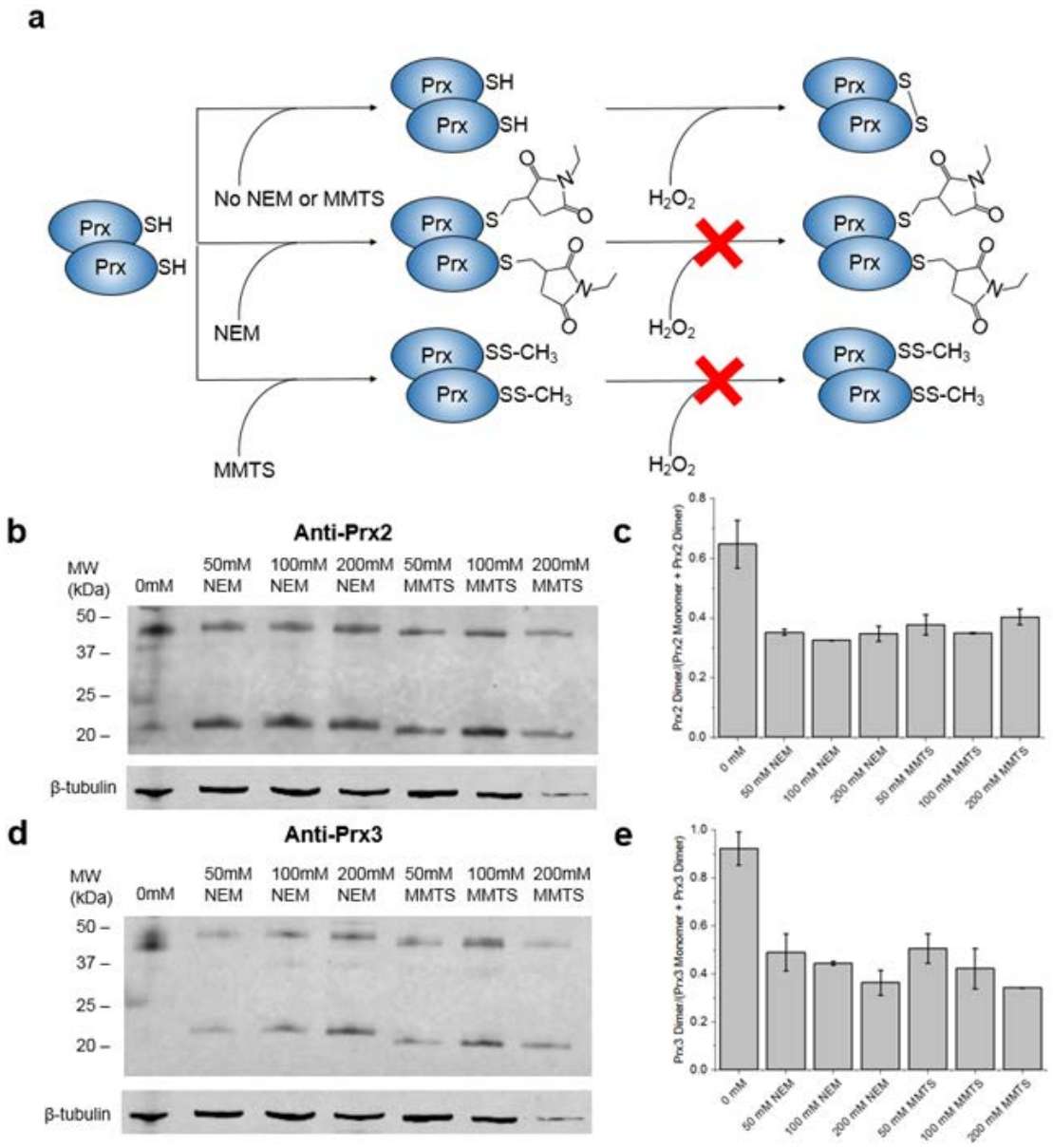


*Figure A.2: Effect of alkylating agent identity and alkylating agent concentration on Prx dimerization status in homogenized GIST biopsies. (a) Schematic representation of effect of NEM and MMTS on Prx oxidation status.* (b-c) Effect of 0-200 mM NEM and MMTS on Prx2 dimerization in GIST biopsies (b) and quantification of the fraction of total Prx2 that is oxidized, where total Prx2 is calculated from the sum of the oxidized (dimer) and reduced (monomer) bands for each condition shown in western blot (c). (d-e) Effect of 0-200 mM NEM and MMTS on Prx3 dimerization in GIST biopsies (d) and quantification of fraction of oxidized Prx3 at each condition shown in western blot (e). Error bars reflect mean ± S.E.M. for two replicates per condition. Tumor fragments for all conditions were obtained from the same parent tumor in order to confine variability to the type and concentration of alkylating agent used.

In addition to alkylating agent concentration and identity, we also sought to determine the extent of artificial oxidation in homogenized GIST biopsies thawed from frozen tumor segments,

and if it differed from GIST biopsies freshly excised from the host mouse. In order to determine the effect of the freeze-thaw process on the amount of artificial oxidation, we homogenized both thawed and fresh GIST biopsies under different conditions, prepared western blots from the soluble protein, and probed the blots for Prx2 and Prx3 (Figure A.3a-d). A comparison of the second and fourth lanes of the blot shows that thawed tumor tissue sections display significantly more oxidized Prx2 and Prx3 than fresh tumor tissue segments homogenized under the same conditions. Further, comparison of the second and third lanes in the blot in Figure A.3 demonstrates that addition of alkylating agent immediately before preservation of the tumor segments on dry ice prevents additional oxidation once thawed.

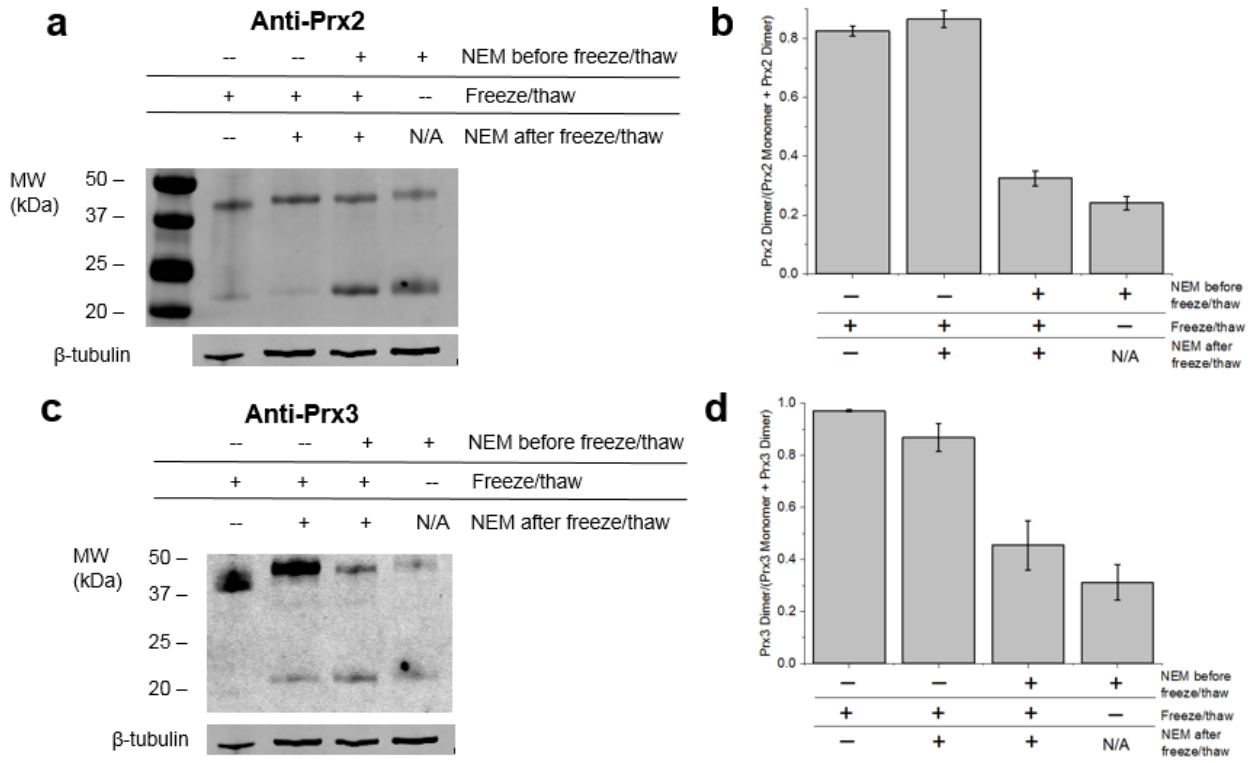


*Figure A.3: Effect of freeze-thaw process on Prx dimerization status in homogenized GIST biopsies. Lane 1: frozen GIST biopsies treated with 0 mM NEM after removal from liquid nitrogen storage; Lane 2: frozen GIST biopsies treated with 50 mM NEM after removal from liquid nitrogen storage; Lane 3: frozen GIST biopsies treated with 50 mM NEM immediately before placement in liquid nitrogen and immediately after removal from liquid nitrogen storage; Lane 4: fresh GIST biopsies treated with 50 mM NEM. (**a**-**b**) Effect of tissue disruption conditions on Prx2 dimerization in GIST biopsies (**a**) and quantification of fraction of oxidized Prx2 (**b**). (**c**-**d**) Effect of tissue disruption conditions on Prx3 dimerization in GIST biopsies (**c**) and quantification of fraction of oxidized Prx3 (**d**). Error bars reflect mean ± S.E.M. for two replicates. Tumor fragments for all conditions were obtained from the same parent tumor in order to isolate the effects of the freeze-thaw process conditions.*

In our last experiment, we sought to compare the fraction of oxidized Prx protein in the human PDX GIST model with the fraction of oxidized Prx protein from a reference human cancer cell line. In the absence of the availability of a cell line that would allow a comparison in the same genetic background, we chose a cell line that allows connection to the existing literature where redox western blots have been used. When immortalized cell lines are cultured in growth medium at atmospheric oxygen concentrations, it is well established that peroxiredoxins are highly abundant and primarily found in the reduced state [10,12,13,17,18]. Comparison data for tumor tissues has not yet been reported. It is possible that the relative scarcity of nutrients and oxygen within the tumor could lead to dramatically altered expression levels and or/extent of oxidation of Prx.

Human GIST samples freshly excised from a mouse were pre-treated with 200 mM of NEM before homogenization. For comparison, a culture of HeLa cells were immersed in 200 mM NEM for an equivalent period of time and lysed. Both samples were then subjected to non-reducing SDS-PAGE followed by western blot (Figure A.4a-e). As shown in the figure, the GIST samples contained a similar fraction of oxidized Prx2 in the cytosol as the HeLa cells, as well as similar amounts of total Prx2 protein. These data also suggest sub-significant differences in the amount of oxidized Prx3 and total Prx3 protein between the GIST and HeLa samples.

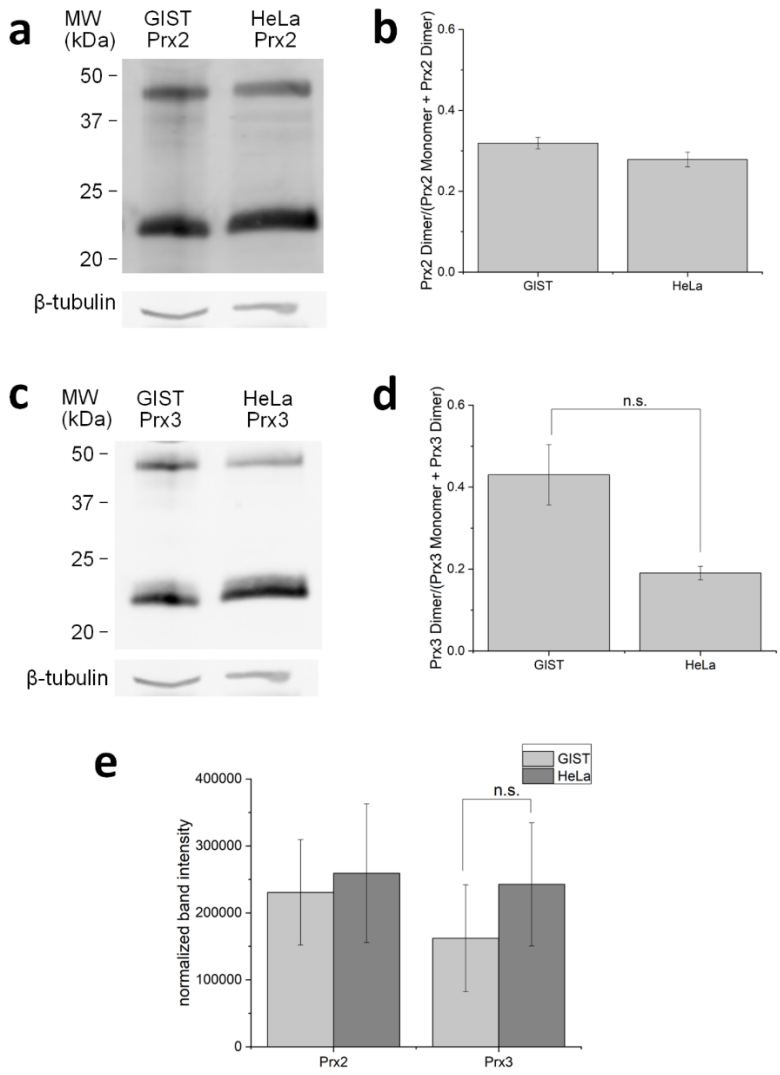


*Figure A.4: Comparison of oxidized and reduced Prx2 and Prx3 levels in patient derived xenograft GIST samples and HeLa cell samples. (**a**) Western blot demonstrating the relative amounts of oxidized and reduced Prx2 in freshly homogenized human GIST biopsies and HeLa cells treated with 200 mM NEM, with the corresponding densitometry comparing the fraction of oxidized Prx2 given in (**b**). Western blot and corresponding densitometry for Prx3 are given in (**c**) and (**d**). (**e**) Comparison of total Prx2 and Prx3 content of GIST biopsies and HeLa cells. Protein band intensities were normalized to the β-tubulin loading control. Error bars reflect mean ± SEM for three biological replicates. Statistical significance reflects a two-tailed t-test at the 95% confidence level.*

## A.4 Discussion

In order to prevent lysis-induced oxidation of protein-thiols in samples from established human cell lines, prior studies have utilized alkylating agents such as MMTS and NEM. These compounds react with the free thiols of cellular proteins to form adducts that prevent additional oxidation of the protein samples upon cell lysis. Previously, Sobotta et al. found that addition of

either MMTS or NEM to HEK293 cells grown in 2D cell culture resulted in a decrease in the amount of artificial Prx2 oxidation, and that MMTS was more effective at reducing artificial oxidation than NEM [17]. However, Cox et al. demonstrated that NEM can also serve as a very effective agent in Jurkat cells at high enough concentrations [18]. Kumar et al. showed that treatment of mouse hearts undergoing ischemia and reperfusion with NEM could preserve information about peroxiredoxin oxidation status [21]. That said, no studies to date have examined the use of these reagents in patient-derived tumor samples. In this study, we utilized both MMTS and NEM to treat human PDX model GIST samples, and systematically examined the effects of several reaction and process conditions.

In order to prevent degradation of fresh tumor samples, researchers often use dry-ice or an equivalent substance to rapidly freeze tumor tissue samples and store them for a later date. However, this process can alter the tissue and lead to a rupture of cellular membranes, which can cause oxidation of very sensitive proteins such as Prxs. In agreement with this claim, and similar to observations in mouse hearts [21], we observed very high levels of oxidized Prx protein in tissue samples frozen in dry ice without prior incubation with MMTS or NEM, but addition of NEM immediately before placement in dry ice substantially reduced the amount of Prx oxidation. These findings suggest that analysis of tissue samples from biorepositories are not likely to provide valuable information regarding the oxidation status of Prx. Future studies of Prx oxidation as a biomarker as suggested in [16] will need to include sample collection and alkylating treatment using methodology we present here in the study design.

Previous studies with kinetic models have suggested that the majority of cytosolic Prx exists in reduced form in human cells [13,22], and numerous experimental studies have demonstrated that many cell types have very low levels of oxidized Prx proteins in the basal state [15,17,18].

Interestingly, the GIST tissue samples used in this study exhibited only slightly higher levels of oxidized Prx in the cytosol, but much higher levels of oxidized Prx in the mitochondria compared to the reference cancer cell line; meanwhile, the total Prx protein in each organelle was actually comparatively lower for the GIST tissue. To that point, the GIST tumor tissue contains a loss-of-function mutation of succinate dehydrogenase B (SDHB), a key mitochondrial protein that could affect intracellular $H_2O_2$ levels. SDHB is one of four separately encoded protein subunits of SDH: subunit A catalyzes the oxidation of succinate to fumarate in the TCA cycle, while subunits B, C, and D support the transport of the free electron to the next member of the electron transport chain. The *SDHB* mutation causes destabilization of the enzyme complex and loss of SDH activity, which can in turn result in impaired transport of electrons that result from the oxidation reaction [23,24]. These electrons can "leak" from the electron transport chain and combine with molecular oxygen in the mitochondria to form $O_2^-$, and eventually $H_2O_2$ [24]. Consequently, the human GIST samples may have higher levels of $H_2O_2$ in the mitochondria as a result of the *SDHB* mutation, which could also potentially explain the higher fraction of oxidized Prx3 in this tissue compared to our reference cancer cell line. An alternative interpretation of these differences could be that, because established cell lines are grown in rich medium and high-oxygen environments, they express the Prxs at higher levels to compensate. This observation about underlying differences in Prx3 protein merits further study through a more comprehensive analysis of many tumors, and could be an interesting avenue of future work.

The aim of this study was to explore the parameters that affect the efficacy of NEM and MMTS as a means to block free thiol groups in human GIST samples obtained from a PDX model. Our results suggest that both MMTS and NEM reduce the amount of artificial Prx2 and Prx3 oxidation in these samples to a similar extent, and concentrations of MMTS and NEM above 50

mM correspond to the most effective blocking of artificial oxidation. Our results also suggest that addition of the alkylating agent immediately after isolation from the host organism is most effective at minimizing artificial oxidation during subsequent processing steps, including freeze/thaw. Finally, our experiment in which we compared Prx oxidation in GIST tissue and HeLa cells suggests that human GIST isolated from the xenograft model have a higher fraction of oxidized Prx3 in the mitochondria, which could reflect disruption of the mitochondrial electron transport chain which could result in additional electron leakage into the mitochondrial matrix and formation of additional $O_2^-$ followed by $H_2O_2$. These results shed light on the effects of NEM and MMTS on the oxidation status of Prxs in patient-derived GIST samples, and provide a basis for the use of these agents block free thiol groups and measure relative Prx oxidation in patient-derived human tissue samples.

## A.5 References


(1) Dugger, S. A.; Platt, A.; Goldstein, D. B. Drug Development in the Era of Precision Medicine. *Nat. Rev. Drug Discov.* **2018**, *17* (3), 183–196.

(2) Aronson, S. J.; Rehm, H. L. Building the Foundation for Genomics in Precision Medicine. *Nature* **2015**, *526* (7573), 336–342.

(3) Favier, J.; Amar, L.; Gimenez-Roqueplo, A. P. Paraganglioma and Phaeochromocytoma: From Genetics to Personalized Medicine. *Nat. Rev. Endocrinol.* **2015**, *11* (2), 101–111.

(4) Dobbelstein, M.; Moll, U. Targeting Tumour-Supportive Cellular Machineries in Anticancer Drug Development. *Nat. Rev. Drug Discov.* **2014**, *13* (3), 179–196.

(5) Gorrini, C.; Harris, I. S.; Mak, T. W. Modulation of Oxidative Stress as an Anticancer Strategy. *Nat. Rev. Drug Discov.* **2013**, *12* (12), 931–947.

(6) Trachootham, D.; Alexandre, J.; Huang, P. Targeting Cancer Cells by ROS-Mediated Mechanisms: A Radical Therapeutic Approach? *Nat. Rev. Drug Discov.* **2009**, *8* (7), 579–591.

(7) Wondrak, G. T. Redox-Directed Cancer Therapeutics: Molecular Mechanisms and Opportunities. *Antioxid. Redox Signal.* **2009**, *11* (12), 3013–3069.

(8) Blackman, R. K.; Cheung-Ong, K.; Gebbia, M.; Proia, D. A.; He, S.; Kepros, J.; Jonneaux, A.; Marchetti, P.; Kluza, J.; Rao, P. E.; et al. Mitochondrial Electron Transport

Is the Cellular Target of the Oncology Drug Elesclomol. *PLoS One* **2012**, *7* (1).

(9) Miyajima, A.; Nakashima, J.; Yoshioka, K.; Tachibana, M.; Tazaki, H.; Murai, M. Role of Reactive Oxygen Species in Cis-Dichlorodiammineplatinum-Induced Cytotoxicity on Bladder Cancer Cells. *Br. J. Cancer* **1997**, *76*, 206–210.

(10) Huang, B. K.; Langford, T. F.; Sikes, H. D. Using Sensors and Generators of H2O2 to Elucidate the Toxicity Mechanism of Piperlongumine and Phenethyl Isothiocyanate. *Antioxid. Redox Signal.* **2016**, *24* (16), 924–938.

(11) Sabharwal, S. S.; Schumacker, P. T. Mitochondrial ROS in Cancer: Initiators, Amplifiers or an Achilles' Heel? *Nat. Rev. Cancer* **2014**, *14* (11), 709–721.

(12) Winterbourn, C. C. Reconciling the Chemistry and Biology of Reactive Oxygen Species. *Nat. Chem. Biol.* **2008**, *4* (5), 278–286.

(13) Lim, J. B.; Huang, B. K.; Deen, W. M.; Sikes, H. D. Analysis of the Lifetime and Spatial Localization of Hydrogen Peroxide Generated in the Cytosol Using a Reduced Kinetic Model. *Free Radic. Biol. Med.* **2015**, *89*, 47–53.

(14) Peskin, A. V.; Low, F. M.; Paton, L. N.; Maghzal, G. J.; Hampton, M. B.; Winterbourn, C. C. The High Reactivity of Peroxiredoxin 2 with H2O2 Is Not Reflected in Its Reaction with Other Oxidants and Thiol Reagents. *J. Biol. Chem.* **2007**, *282* (16), 11885–11892.

(15) Low, F. M.; Hampton, M. B.; Peskin, A. V.; Winterbourn, C. C. Peroxiredoxin 2 Functions as a Noncatalytic Scavenger of Low-Level Hydrogen Peroxide in the Erythrocyte. *Blood* **2007**, *109* (6), 2611–2617.

(16) Poynton, R. a; Hampton, M. B. Peroxiredoxins as Biomarkers of Oxidative Stress. *Biochim. Biophys. Acta* **2014**, *1840* (2), 906–912.

(17) Sobotta, M. C.; Barata, A. G.; Schmidt, U.; Mueller, S.; Millonig, G.; Dick, T. P. Exposing Cells to H2O2: A Quantitative Comparison between Continuous Low-Dose and One-Time High-Dose Treatments. *Free Radic. Biol. Med.* **2013**, *60*, 325–335.

(18) Cox, A. G.; Winterbourn, C. C.; Hampton, M. B. Measuring the Redox State of Cellular Peroxiredoxins by Immunoblotting. In *Methods in enzymology*; Elsevier Inc., 2010; Vol. 474, pp 51–66.

(19) Fischer, J.; Eglinton, T.; Frizelle, F.; Hampton, M. Peroxiredoxins in Colorectal Cancer: Predictive Biomarkers of Radiation Response and Therapeutic Targets to Increase Radiation Sensitivity? *Antioxidants* **2018**, *7* (10), 136.

(20) Powers, J. F.; Cochran, B.; Baleja, J. D.; Sikes, H. D.; Zhang, X.; Lomakin, I.; Langford, T.; Stein, K. T.; Tischler, A. S. A Unique Model for SDH-Deficient GIST: An Endocrine-Related Cancer. *Endocr. Relat. Cancer* **2018**, *25* (11), 943–954.

(21) Kumar, V.; Kitaeff, N.; Hampton, M. B.; Cannell, M. B.; Winterbourn, C. C. Reversible Oxidation of Mitochondrial Peroxiredoxin 3 in Mouse Heart Subjected to Ischemia and Reperfusion. *FEBS Lett.* **2009**, *583* (6), 997–1000.

(22) Adimora, N. J.; Jones, D. P.; Kemp, M. L. A Model of Redox Kinetics Implicates the

Thiol Proteome in Cellular Hydrogen Peroxide Responses. *Antioxid. Redox Signal.* **2010**, *13* (6), 731–743.

(23) Bezawork-Geleta, A.; Wen, H.; Dong, L.; Yan, B.; Vider, J.; Boukalova, S.; Krobova, L.; Vanova, K.; Zobalova, R.; Sobol, M.; et al. Alternative Assembly of Respiratory Complex II Connects Energy Stress to Metabolic Checkpoints. *Nat. Commun.* **2018**, *9* (1).

(24) Kluckova, K.; Tennant, D. A. Metabolic Implications of Hypoxia and Pseudohypoxia in Pheochromocytoma and Paraganglioma. *Cell Tissue Res.* **2018**, *372* (2), 367–378.

(25) Selvaggio, G.; Coelho, P. M. B. M.; Salvador, A. Mapping the Phenotypic Repertoire of the Cytoplasmic 2-Cys Peroxiredoxin – Thioredoxin System. 1. Understanding Commonalities and Differences among Cell Types. *Redox Biol.* **2018**, *15* (November 2017), 297–315.